FLUID-STRUCTURE INTERACTIONS OF AN OSCILLATING CYLINDER IN CROSS FLOW IN THE PRESENCE OF A NEIGHBOURING CYLINDER

Xu Shengjin

A thesis submitted for the Degree of
Doctor of Philosophy in Mechanical Engineering at
The Hong Kong Polytechnic University

Hong Kong, 2003

I hereby certify that the work embodied in this thesis is the result of original research and has not been submitted for a higher degree to any other University or Institution.

(Signed).....

Acknowledgements

I would like to express my deepest gratitude to my supervisor, Associate Professor Y. Zhou, for excellent guidance and sincere encouragement throughout my study and preparation of this thesis. His considerable and strict work attitude benefits me in my research, no matter in the past three years or in the future. I would like to express my deep gratitude to my co-supervisor Professor R. M. C. SO, the head of ME department, for many helpful discussions and suggestions during this project. I would also give my special thanks to co-supervisor Dr. W, Jin for his assistance.

Grateful acknowledgements are also extended to Dr. G. Q. Xu for helpful suggestions to the thesis writing, Dr. Z. J. Wang, Dr. H. J. Zhang, Dr, Y. Y. Li, Messieurs W. C. Lai, M. M. Zhang, K. K. Lo, K. M. Cheung, K. K. Shun and K. Y. Ng for their assistance to the experimental setups.

I wish to acknowledge support given by the Central Research Grant of The Hong Kong Polytechnic University through the Research Grants Council of the Government of the HKSAR through Grants PolyU5125/98E and PolyU 5128/98E.

I also wish to thank Prof. B. L. Wang, Prof. X. R. Ma and Prof. Z. Q. Deng who were my previous supervisors when I studied in Harbin Institute of Technology. They made much convenience for me to study in The Hong Kong Polytechnic University.

Finally, I wish to express my sincerest gratitude to my wife, Xiaochao Zhang, my son, Bei Bei and my parents, for their love, tolerance and support throughout this work.

CONTENTS

Abstract

The fluid-structure interactions of a single streamwise oscillating circular cylinder and two tandem (including a streamwise oscillating circular cylinder) and side-by-side circular cylinders have been experimentally investigated using methods of LIF (Laser-induced fluorescence) visualization, PIV, laser vibrometer and hot wires.

In the case of a single streamwise oscillating cylinder, the wake mode has been studied at relatively large oscillation amplitudes A/d = 0.5 and 0.67 over a range of frequencies $f_e/f_s = 0 \sim 3.1$. Five typical flow structures, referred to as S-I, S-II, A-I, A-III and A-IV modes, respectively, are identified. Their occurrence is dependent on a combination of A/d and f_e/f_s. The occurrence of the S-II mode has been predicted. The threshold frequency ratio $(f_e/f_s)_c$ for the occurrence of the S-II mode is inversely proportional to A/d and dependent on the Reynolds number Re. The Re effect is negligible for $Re > 250$. The results are in good agreement with available experimental data.

Interference between a streamwise oscillating cylinder (A/d = 0.5 and 0.67, $f_e/f_s = 0 \sim 2$) wake and that of a downstream stationary cylinder with an identical diameter has been experimentally studied. The center-to-center spacing L/d of two cylinders varies from 2.5 to 4.5. Three distinct flow regimes have been identified. For $0.45 \sim 0.5 < f_e/f_s < 0.8 \sim 1.0$ (depends on A/d), a single antisymmetrical vortex street (A-mode) emerges behind the downstream cylinder. For $0.8 \sim 1.0 < f_e/f_s < (f_e/f_s)_c$ which depends on A/d and

Re, the flow behind the downstream cylinder is characterized by an antisymmetric-antisymmetric complex street (AA-mode) that consists of two outer rows of binary vortices originating from the upstream cylinder, and two inner rows of single vortices shed by the downstream cylinder. For $f_e/f_s > (f_e/f_s)_c$, the symmetric-antisymmetric complex street (SA-mode) occurs behind the downstream cylinders, respectively. Effects of initial conditions such as L/d, Re, f_e/f_s and A/d on the flow regimes have been discussed. Analysis has been developed to predict the occurrence of the SA-mode flow structure; the analysis is in excellent agreement with the experimental data.

Interference between a stationary cylinder wake and that of a downstream streamwise oscillating cylinder ($L/d = 2.5 \sim 4.5$; $A/d = 0.5$ and 0.67; $f_e/f_s = 0 \sim 2$) has also been studied. Two flow regimes have been identified, i.e., the 'single-cylinder shedding regime' at $L/d \leq 3.5$ and the 'two-cylinder shedding regime' at $L/d > 3.5$. For the 'single-cylinder shedding regime', the upstream cylinder does not appear to shed vortices; vortices are symmetrically formed behind the downstream cylinder as a result of interactions between the shear layers separated from the upstream cylinder and the oscillation of the downstream cylinder. For the 'two-cylinder shedding regime', the vortices are shed alternately from the upstream cylinder; a staggered spatial arrangement of vortices occurs behind the downstream cylinder.

Experimental study of the wake structure of two side-by-side cylinders has been conducted at Re = 150 - 14300. The focus is on the effect of Re on the dominant frequency of the wake in the asymmetrical flow regime, i.e., T/d = 1.2 - 1.6 (T is the center-to-center cylinder gap). As Re increases, the flow structure behind the cylinders

may change from one single vortex street to two vortex streets with one narrow and one wide for the same *T/d*. The one-street flow structure is dominated by one frequency $f_0^* = f_0 d / U_\infty \approx 0.09$, where f_0 is the dominant frequency and U_∞ is the free-stream velocity. Two dominant frequencies of $f_0^* \approx 0.3$ and 0.09 characterize the two-street flow structure. The critical *Re*, at which the transition from single to two streets occurs, increases as *T/d* decreases. The present results help clarify previous scattered reports for $1.2 < T/d < 1.5$: detection of one dominant frequency by some but two by others.

Finally, vortex induced vibration of a single cylinder in a cross flow was analyzed theoretically by considering the cylinder as an elastic beam. Two-Dimensional coupled and nonlinear dynamics equations were established using Hamilton's principle. The fluid forces were simplified and calculated using related parameters such as the Strouhal number, root-mean-square lift and drag coefficients, and fluid damping ratio, which could be directly determined from previous experimental results. Displacement and strain responses, and the natural frequency of the cylinder have been found analytically using Mathematica© software. The results are in agreement with the available experimental data.

Nomenclature

A	Oscillation amplitude.
A_c	Cross section area of a cylinder.
c_m	Added mass coefficient.
c_s	Viscous damping coefficient.
c_x, c_y	Viscous damping coefficients in the drag and lift direction, respectively ($N \cdot s / m^2$).
C_D	Drag coefficient $\equiv 2F_D/(\rho U_\infty^2 A_c)$.
C_L	Lift coefficient $\equiv 2F_L/(\rho U_\infty^2 A_c)$.
C_D'	Fluctuating drag coefficient.
C_L'	Fluctuating lift coefficient.
C_p	Pressure coefficient $\equiv 2\Delta p/(\rho U_\infty^2)$.
C_{pb}	Base pressure coefficient.
d	Diameter of a circular cylinder (m).
E	Young's modulus of the cylinders.
EI	Structural stiffness.
f	Frequency in spectrum analysis (Hz).
F_D	The resultant force on the cylinder in the drag direction.
F_L	The resultant force on the cylinder in the lift direction.
f_e	Oscillation frequency of cylinders.

$f^{(1)}_y$	First-mode natural frequency of a circular cylinder in the lift direction (Hz).
$f^{(3)}_y$	Third-mode natural frequency of a circular cylinder in the lift direction (Hz).
$f_0^{(n)}$	The nth mode structural natural frequency (Hz), n = 1, 2, 3, ...
$f_x^{(n)}$, $f_y^{(n)}$	The nth mode inline and cross-flow natural frequencies, respectively, of the fluid-cylinder system (Hz), n = 1, 2, 3,...
f_s	The natural vortex shedding frequency of a stationary cylinder (Hz).
I	Moment of inertia (m^4).
I_{xx}, I_{yy}	Moment of inertia about the x and y axes, respectively (m^4).
I_{xy}	Product of inertia with respect to the x and y axes (m^4).
l	Cylinder length (m).
L	Centre-to-centre spacing of two cylinders in a tandem arrangement.
m	Structural mass per unit length = $\rho_s A$.
M	Sum of added mass and the cylinder unit length mass = $(c_m + 1)\rho_s A$.
M^*	Mass ratio = $M/\rho d^2$.
Re	Reynolds number ≡ $U_\infty d / \nu$.
q_x, q_y	Fluid excitation force in the drag and lift directions, respectively.
$\overline{q}_x$, $\overline{q}_y$	The mean fluid excitation force in the drag and lift directions, respectively.

$\tilde{q}_x, \tilde{q}_y$	Fluctuating fluid excitation force in the lift and drag directions, respectively.
St	Strouhal number = $f_s d / U_\infty$.
t	Time (sec).
t^*	Dimensionless time $= t / 2\pi f_0$.
T	Centre-to-centre Spacing two cylinders in side-by-side arrangement.
U_∞	Free stream velocty (m/sec).
U_r	Reduced velocity $\equiv U_\infty / f_0 d$.
U_{rel}	Relative velocity between stream and cylinder (m/s).
U, T, W	Strain energy, kinetic energy and work done by external forces and axial force, respectively (J).
x, y, z	Coordinates in the stream-wise, lateral and span-wise directions, respectively.
X, Y, Z	Cylinder displacements in the x, y, and z direction, respectively (m).
Y^*	$= \frac{Y_{rms}\big\vert_{N\neq 0}}{Y_{rms}\big\vert_{N=0}}$, where $Y_{rms}\big\vert_{N\neq 0}$ and $Y_{rms}\big\vert_{N=0}$ denote Y_{rms} calculated with and without the effect of axial force N present, respectively.
X_{rms}, Y_{rms}	Root mean square values of X and Y, respectively (μm).
z^*	Dimensionless length = z/d.

Greek Symbols

ρ	Mass density of fluid (kg/m^3).
ρ_s	Mass density of structures (kg/m^3).
ε	Strains.
$\varepsilon_x, \varepsilon_y$	Dynamic strains due to drag and lift, respectively.
ω_z	Vorticity.
Ω_D, Ω_L	The circular frequency of vortex exciting forces in the drag and lift directions, respectively. $\Omega_D / 2 \approx \Omega_L = 2\pi SU_\infty / d$ (rad/s).
$\zeta_0^{(1)}$	The first-mode structural damping ratio.
ζ_e	Modal damping ratio of a fluid-cylinder system.
$\zeta_s^{(n)}$	The nth mode structural damping ratio, n = 1, 2, 3,...
ζ_f	Fluid damping ratio.
$\zeta_{x,f}^{(n)}$, $\zeta_{y,f}^{(n)}$	The nth mode inline and cross-flow fluid damping ratios, respectively, n = 1, 2, 3,...
$\zeta_{x,e}^{(n)}$, $\zeta_{y,e}^{(n)}$	The nth mode inline and cross-flow effective (or system) damping ratios, respectively, n = 1, 2, 3, ...
θ	The azimuthal angle around a cylinder with the origin at the forward stagnation point.
θ_R	The angle of resultant force.
Δp	The mean pressure difference between the wall pressure and a reference pressure.

ν	The fluid kinematic viscosity.
ϕ	Phase.

Superscript

*	Denotes a dimensionless parameter normalized by f_s or d, or U_∞ unless otherwise stated.

Subscript

rms	Root mean square.

CHAPTER 1

INTRODUCTION

1.1 Background

When a flow blows over a bluff body, the vortex formation is strongly controlled by the dynamics in the low-base-pressure region and feedback from the fluctuating wake (Naudascher 1987). For a stationary cylinder, this control leads to anti-symmetric vortex shedding and formation of a Karman vortex street. If the cylinder is flexible or flexibly mounted, interactions can arise between vortex shedding and the cylinder movement (King, 1977). The fluid-structure interactions are of common occurrence in engineering. For example, pipeline-suspension bridges, power lines, large towers, chimneys and skyscrapers in airflow; marine piles, marine cables, submarine periscope and brace members of offshore structures in water. They can be excited to oscillate in both cross-flow direction and streamwise direction (King *et al.* 1973). Under certain conditions, structures oscillate at a frequency close to or consistent with their natural frequencies, e.g., resonance and synchronization (Zdravkovich, 1997; pp.588). The occurrence of resonance or synchronization is often accompanied by a relatively large vibration

amplitude, large deformation and large stress that may be over allowable regarding the safe values of design. It often results in structural damage or failure. Examples include the collapse of the Tacoma Narrows Bridge (Figure 1.1) during a violent windstorm, and the damage of piling during the construction of an oil terminal on the Humber estuary of England in 1960s (Griffin & Ramberg 1976). Suppressing or controlling the occurrence of resonance and synchronization of fluid-structure systems is often required in engineering. Therefore, it is of fundamental importance and of engineering significance to investigate fluid-structure interactions.

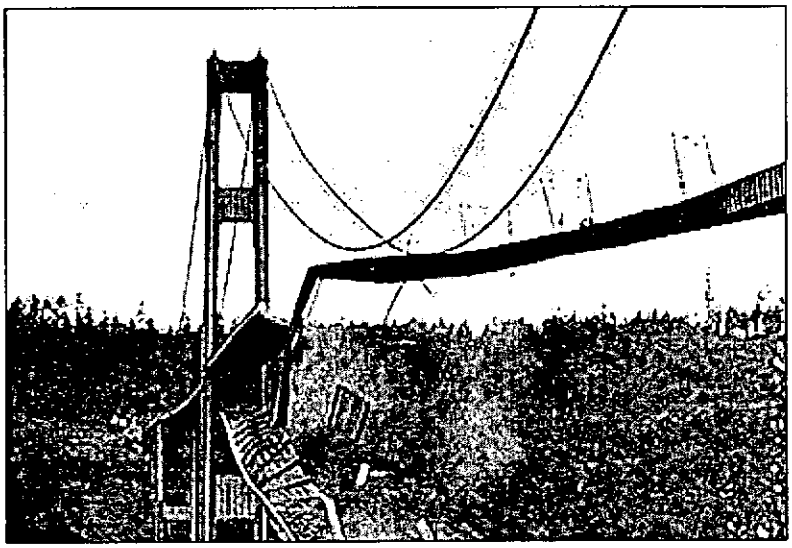

Figure 1-1 Bridge midsection crashing into the waters of the Tacoma Narrows.

(http://www.lib.washington.edu/specialcoll/tnb/page4.html)

Fluid-structure interactions are of significant complexity since the dynamic mechanisms of flow and structures are coupled and nonlinear (Chen 1987). There are

three important kinds of research approaches on this issue. First, structures are assumed to vibrate freely in a cross flow, e.g., Feng (1968), King (1977) & Sarpkaya (1979), Bearman (1984), Chen (1987), Blevins (1994), Kahalak & Williamson (1996, 1997 and 1999), Govardhan & Williamson (2000) and Zhou *et al.* (2001 & 2002). These studies have made considerable advances in determining the wake structure and relating it to the vibration of structures. Second, interactions between structures and an oscillatory flow are concerned. There are fundamental differences between the structures in the oscillatory flow and those in a steady flow. However, the vortex formation and the alternate vortex shedding for both cases follow a similar pattern (Zdravkovich & Namork, 1977). Studying this issue is also the first step to understand the complex wave-structure interaction. (Lighthill, 1979; Sarpkaya, 1980; Williamson, 1985). Third, structures are forced to oscillate in a cross flow (e.g. Bishop & Hassan, 1963; Tanida *et al.* 1973; Griffin & Ramberg, 1976; Ongoren & Rockwell, 1988a & b; Williamson & Roshko, 1988; Staubli & Rockwell, 1989; Griffin & Hall, 1991; Hover *et al.* 1998; Carberry & Sheridan, 2001; and Cetiner & Rockwell, 2001). In this case, the motion of structures undergoing flow-induced vibrations is simulated by means of giving structures a simple and known motion such as harmonic oscillation. This approach decouples the response of structures from that of flow. Fluid-structure interactions are hence simplified by controlling the motion of structures.

Evidently, investigation of an oscillating cylinder subjected to a cross flow in the presence of a neighbouring cylinder is a traditional approach to investigate fluid-structure interactions. Furthermore, multiple oscillating structures in a cross flow is frequently seen

in engineering or control applications. The interactions between fluid and oscillating structures not only vary the fluid forces on structures but also re-organize the fluid flow. The re-organized flow can affect flow forces on neighbouring structures or their wake. The oscillating structure can be utilized for appropriate control devices in vibration-suppression and transport enhancement applications (Karniadakis and Triantafyllou, 1989). Therefore, it is of both fundamental and practical significance to investigate fluid-structures interactions of an oscillating structure in the presence of neighbouring structures.

The present study is largely focused on fluid-structure interactions of a streamwise oscillating circular cylinder in a cross flow in the presence of a neighbouring cylinder. It covers five aspects based on the relative location between the oscillating cylinder and the neighbouring cylinder: i) A streamwise oscillating cylinder in a cross flow (the neighbouring cylinder is at infinity); ii) A stationary cylinder in the wake of a streamwise oscillating cylinder; iii) A streamwise oscillating cylinder in the wake of a stationary cylinder; iv) The Reynolds number effect on the flow structure behind two side-by-side cylinders; v) Theoretical analysis for vortex-induced vibration of an elastic cylinder in a cross flow.

1.2 Brief Review of Literature

Previous investigations related to the present work are surveyed; they cover investigation of a streamwise oscillating cylinder in a cross flow, experiments of streamwise oscillations of two tandem cylinders, studies of two side-by-side cylinders in

a cross flow and analysis of flow-induced vibration of a single elastic cylinder in a cross flow.

1.2.1 A streamwise oscillating circular cylinder in a cross flow

There have been a number of investigations involving a streamwise oscillating cylinder in a cross-flow. Tanida *et al.* (1973) measured the lift and drag forces on a streamwise oscillating circular cylinder to study the stability of the oscillation of cylinder at $A/d = 0.14$ and $f_e/f_s = 0.5 \sim 2.2$. Herein, d is the cylinder diameter, f_s is the natural vortex shedding frequency of a stationary cylinder, and A and f_e are the structural oscillation amplitude and frequency, respectively. Griffin and Ramberg (1976) visualized the vortex formation from a cylinder oscillating in line with flow at the onset of 'lock-on'. The ranges of f_e/f_s and A/d investigated ranged from 1.74 to 2.2 and 0.06 to 0.12 ($Re = 190$), respectively. Lock-on refers to the situation where the vortex shedding frequency coincides with that of the structural oscillation frequency. An anti-symmetric vortex street occurred at $A/d = 0.06 \sim 0.1$ and $f_e/f_s = 1.74 \sim 2.2$. But as A/d was increased to 0.12, they observed a vortex street consisting of one row of single vortices and one row of counter-rotating vortex pairs. These two different flow structures in effect correspond to A-I and A-III modes, respectively, as categorized by Ongoren and Rockwell (1988b). Ongoren and Rockwell (1988b) investigated the flow patterns behind a cylinder oscillating at an angle with respect to the streamwise direction. The investigated A/d was fixed at 0.13 and 0.3, and f_e/f_s varied from 0.5 to 4.0. Two basic modes, i.e., the symmetrical and anti-symmetrical vortex formation, were identified. They further

classified the two basic modes into five submodes: S mode for the symmetric vortex formation and A-I, II, III, IV modes for the anti-symmetric vortex formation. The A-II mode did not occur in the case of streamwise oscillation. Recently, Cetiner & Rockwell (2001) studied the lock-on state of a streamwise oscillating cylinder in a cross flow (f_e/f_s = 0.5 ~ 3.0) and found that the time-dependent transverse force was phase-locked to the cylinder motion and the vortex system occurred both upstream and downstream of the cylinder. These studies have uncovered many important aspects of physics associated with a streamwise oscillating cylinder wake, but the cylinder oscillation amplitude investigated has been relatively small ($A/d \leq 0.3$).

1.2.2 Streamwise oscillations of two tandem cylinders in a cross flow

For two stationary cylinders in tandem (or in-line) arrangement, there have been many studies on vortex formation, vortex interference, fluid forces, dynamic strains, vibration modes, damping and natural frequencies, and amplification and suppression of flow-induced vibrations (e.g., Zdravkovich, 1977, 1980, 1984, 1985 and 1986; Zdravkovich & Namork, 1980; Igarashi 1981 and 1984; Arie *et al.* 1983; Williamson, 1985; Zhou *et al.* 2001 and 2002).

If one or both cylinders are flexible, vortex shedding may result in large amplitude vibration. King (1976) investigated experimentally wake interactions between two tandem flexible cylinders in a water flow at a range of L/d = 0.25 to 6.0 and Re = 1000 to 20000. The longitudinal distance between the axes of two cylinders in tandem arrangement is denotated L. When the upstream cylinder is allowed to oscillate by vortex

shedding in the first instability region (reduced velocity < 5), symmetric vortices shed from both the upstream and downstream cylinders at $L/d = 1$. For $L/d = 3$, however, the symmetric vortices shed from the upstream cylinder become misaligned when they arrive at the downstream cylinder. Finally, these vortices form an alternate street. Brika and Laneville (1999) studied experimentally the dynamic response of a long flexible circular cylinder in the wake of a stationary cylinder at $Re = 5000$ to 27000. They found that the synchronization onset is at a higher reduced velocity. Laneville & Brika (1999) had also examined the effect of the fluid and mechanical couplings between two flexible circular cylinders on their vortex-induced vibrations. They found the upstream cylinder behaves as an isolated cylinder when only fluid coupling is present.

When one of two tandem cylinders is forced to oscillate streamwise (longitudinal, in-line or horizontal direction as used in some papers), fluid-structure interactions between fluid and cylinders will differ from those of two stationary cylinders. There have been a limited number of investigations on a streamwise oscillating cylinder in two tandem cylinders in a cross flow. Tanida *et al.* (1973) measured the lift and drag forces on two tandem circular cylinders when the downstream cylinder oscillated streamwise at $A/d = 0.14$ and $f_e/f_s = 0.5 \sim 2.2$. They found that no synchronization is induced by oscillation for any L/d at $Re = 80$. For $L/d < 5$ and $Re = 80$, no vortex shedding can be observed irrespective of the oscillation of the downstream cylinder. For $L/d > 5$ and $Re = 80$, vortices shed from the oscillating downstream cylinder are almost independent of the oscillation of the downstream cylinder. The fluctuating drag force of the downstream cylinder is nearly proportional to the oscillating frequency and plays a role of the positive

damping. When Re = 4000 and L/d > 3, synchronization always can be observed whilst the shedding frequency of vortices from the downstream cylinder was half the oscillating frequency. The effect of synchronization on the vortex shedding from the upstream cylinder is quite limited. Li *et al.* (1992) conducted a direct numerical simulation (DNS) of an oscillating cylinder (A/d = 0.14) in the wake of an upstream cylinder. They identified two flow regimes. In the 'vortex formation regime' at large L/d (> 3.7), vortex streets developed behind both cylinders. The street generated by the upstream cylinder was important compared to the forced oscillation and dominated the flow, resulting in a very small zone of synchronization. In the 'vortex suppression regime' at small L/d, this street became weak and had little effect on the downstream cylinder wake. The upstream cylinder or the downstream cylinder oscillating streamwise at a relative large oscillation amplitude has not been previously reported.

1.2.3 The Reynolds number effects on the flow structure behind two side-by-side cylinders

The wake behind two side-by-side circular cylinders has attracted considerable interest in the past because of its practical significance in many branches of engineering. As a result, our understanding of this flow has been greatly improved. It is now well established that, when the ratio of the transverse center-to-center spacing T of the cylinder to the diameter d, T/d, is beyond 2, two distinct vortex streets have been observed (Landweber 1942). For 1.5 < T/d < 2.0, the base pressure on each cylinder is

different. The gap flow between the cylinders is deflected toward the cylinder with the lower base pressure, resulting in one narrow wake. Meanwhile, one wide wake develops behind the neighboring cylinder. The deflected gap flow is bi-stable and randomly changes over from one side to the other (Ishigai *et al.* 1972; Bearman & Wadcock 1973). The timescale for the changeover is several orders of magnitude longer than that of vortex shedding and of the instability of the separated shear flows (Kim & Durbin 1988). At $T/d < 1.2$, the two cylinders behave like one structure, generating a single vortex street (Sumner *et al.* 1999). Peschard and Le Gal (1996) further found that the Reynolds number may affect the way the two streets were coupled; the two streets could be in-phase locking, asymmetric locking, quasi-periodic and phase-opposition locking.

However, many aspects remain to be clarified, in particular, in the asymmetrical flow regime, i.e., $T/d < 2.0$. For example, previous results indicate a lack of consistency in the vortex shedding frequencies for $1.2 < T/d < 1.5$. Ishigai *et al.* (1972) measured two dominant frequencies in the range $T/d = 1.25 \sim 1.5$, namely $f_0^* = f_0 d / U_\infty \approx 0.1$ and 0.3, respectively, where f_0 is the dominant frequency and U_∞ is the free-stream velocity. The two frequencies were also detected by Spivac (1946) in the range, $T/d = 1.5 \sim 2.0$. He further detected a frequency f_0^* of 0.2, which could be interpreted as the second harmonic of 0.1. However, he failed to detect $f_0^* = 0.3$ at $T/d \approx 1.25$. Kim & Durbin (1988) measured two frequencies of near 0.1 and 0.3, respectively, for $T/d = 1.5 \sim 2.0$, but detected only $f_0^* = 0.1$ for $T/d < 1.5$.

1.2.4 Structural dynamics of an elastic beam in a cross flow

This simple free vibration problem of an elastic beam in a cross flow is very complicated. It involves transition to turbulence in the wake and three-dimensional (3-D) wake behavior even when the aspect ratio of the structure is large and the flow is 2-D. A complete solution of the problem involves solving for the flow field, the structural dynamics and the interaction between the flow and the structural motions. Various computational and theoretical approaches have been proposed to solve this simple flow-induced vibration problem. These approaches include direct numerical simulation (Newman & Karniadakis, 1996; Evangelinos & Karniadakis, 1999; Evangelinos *et al.* 2000), finite-element method (Mendes & Branco, 1999; Mittal & Kumar, 1999; So *et al.* 2000a; Wang *et al.* 2000), boundary-element methods (Jadic *et al.* 1998; So *et al.* 1999), and approximate method (Sarpkaya, 1995; Skop & Griffin, 1973; Iwan & Blevins, 1974; Landl, 1975; Berger, 1988).

With the exception of the empirical approach, either the Navier-Stokes or the Euler equations are solved for the flow field, a one- or two-degree-of-freedom equation of motion is assumed for the structural dynamics, and an iterative time-marching technique is employed to account for fluid-structure interaction. The one-degree-of-freedom (1dof) approach only solves for the motion along the lift direction and assumes the fluctuating motion along the drag direction to be relatively unimportant. In these approaches, focus was on the flow behavior so that the transition to turbulence in the wake and the 3-D effects of the wake flow could be investigated in detail (Evangelinos *et al.* 2000). As a result, even if a 3-D solution is available for the flow field, a 2-D

approach is still assumed for the structural dynamics (Evangelinos & Karniadakis, 1999). Only recently, attempts were made to include 3-D consideration of the structural motions (Evangelinos *et al.* 2000; Wang *et al.* 2000). Through the use of a beam theory, the different modes of vibration could be resolved. In these recent attempts, the symmetry assumption was invoked; thus the even modes of vibration cannot be calculated. However, the actual flow, especially when turbulent, is unlikely to be symmetrical about the mid span of a beam at any particular instant. As a result, resonance, albeit weak, could occur with the second-mode natural frequency of the fluid-structure system. This has been confirmed by recent experimental investigations (Zhang *et al.* 2000; Zhou *et al.* 2000). Up till now, no known computational or theoretical attempts have been able to predict the occurrence of this type of resonance.

The approximate approach, on the other hand, only solves the structural dynamic equations; it assumes a model for the vortex-excited force. The effects of fluid damping and fluid-structure interaction are built into the force model. Two different types of models are commonly used; they are the force decomposition model (Sarpkaya, 1995) and the nonlinear wake oscillator model (Skop & Griffin, 1973; Iwan & Blevins, 1974; Landl, 1975; Berger, 1988). Typically, the force decomposition model is formulated to account for both the inertia (in-phase component) and the drag (out-of-phase component) force effects. Along the lift direction, these two components are usually called the lift drag component and the lift inertia component. Fluid damping could be factored from the lift drag component. In the models assumed for the vortex-excited force, a number of empirical parameters are introduced. They are usually determined from experimental

measurements or from potential flow theory. Attempts have also been made to incorporate motion-dependent fluid forces into the assumed vortex-excited force model (Chen, 1978).

Usually, the approximate approach attempts to solve either the 1dof or the 2dof equations of motion and has not yet been applied to the solution of the beam equation. The difficulty could be traced to the assumed force model, which has not been formulated to have an axial dependence. A 2dof correction formula has been proposed by Wang *et al.* (2000), whereby the mid-span displacement prediction could be transformed into a spanwise distribution. However, inherent in this correction is the assumption that the vortex-excited force along the span is uniform, because the mean flow is assumed to be 2-D in their derivation of the correction formula. Nevertheless, the formula yields a fair prediction of the displacement distribution along the span for two cases, one where the structure is in resonance with the first-mode vibration and one where the structure vibrates at off resonance. Again, the assumption of symmetry is invoked and no even-mode vibrations are observed.

1.3 Gaps and Objectives

Studies mentioned in Section 1.2 have uncovered many important aspects of the physics associated with interactions between a streamwise oscillating cylinder and fluid, a neighbouring cylinder in a cross flow. In engineering, the structural oscillation amplitude could be of the order of one cylinder diameter or even significantly larger. If A/d is relatively large, vortex formation from a streamwise oscillating cylinder could be

different from that of relatively small *A/d*. The effects of a streamwise oscillating cylinder with a large *A/d* on the neighbouring cylinder are still unknown. In summary, the following issues/questions have yet to be addressed.

i) For a single streamwise oscillating cylinder in a cross flow, are there any new flow structures other than those summarised by Ongoren and Rockwell (1988b)?

ii) For a stationary cylinder in the wake of a streamwise oscillating cylinder, how do the wakes of the two cylinders interact? What is the dominant flow structure when the upstream oscillating cylinder is locked on with the vortex shedding?

iii) How would the flow be affected if a streamwise oscillating cylinder is immersed in a stationary-cylinder wake? What is the dominant flow structure when the cylinder oscillation is locked on with the vortex shedding?

iv) For two side-by-side cylinder wake in a cross flow, why are the observations scattered in terms of dominant frequencies? Is it related to the effect of initial conditions, especially *Re*? Does the effect depend on *T/d*? How is the flow structure affected?

v) For an elastic beam subjected to an axial force in a cross flow, what would the dynamic response of vortex-induced vibration be in the lift, drag and spanwise directions? Could these issues be solved using a relative simple method?

These issues motivate the present investigation. The work mainly aims to understand fluid-structure interactions between a streamwise oscillating cylinder and a neighbouring cylinder in a cross flow based on experiments (LIF visualization, PIV, Laser vibrometer and hot-wires) and analysis. The main objectives are summarized below.

i) To investigate possible new flow structures behind a circular cylinder streamwise oscillating at relatively large amplitude.

ii) To investigate wake interference between a streamwise oscillating circular cylinder and a stationary downstream cylinder, and to understand the effects of the oscillating cylinder on the downstream cylinder wake.

iii) To study wake interference between a streamwise oscillating circular cylinder and an upstream cylinder.

iv) To examined the effect of *Re* on the flow structure behind two side-by-side cylinders and the possible relationship between the flow structure and the scattered observation of the dominant frequencies.

v) To establish dynamic equations of an elastic beam subjected to axial forces in a cross flow. Attempt to solve these differential equations analytically.

1.4 Experimental Instruments and Facilities

In the present work, experiments were mainly carried out in both water tunnel and wind tunnel in Mechanical Engineering Department of The Hong Kong Polytechnic University. The detailed information of the water and wind tunnels can be found in Zhou *et al.* (2001, 2002). LIF (laser-induced fluorescence) flow visualization, PIV (particle image velocimetry), laser vibrometer and hot wire techniques were employed.

In LIF flow visualization, a Spectra-Physics Stabilite 2017 Argon Ion laser with a maximum power output of 4 watts was used to generate the laser beam and a professional

digital video camcorder (JVC GY-DV500E) was used to record the dye-marked vortex streets at a framing rate of 25 frames per second.

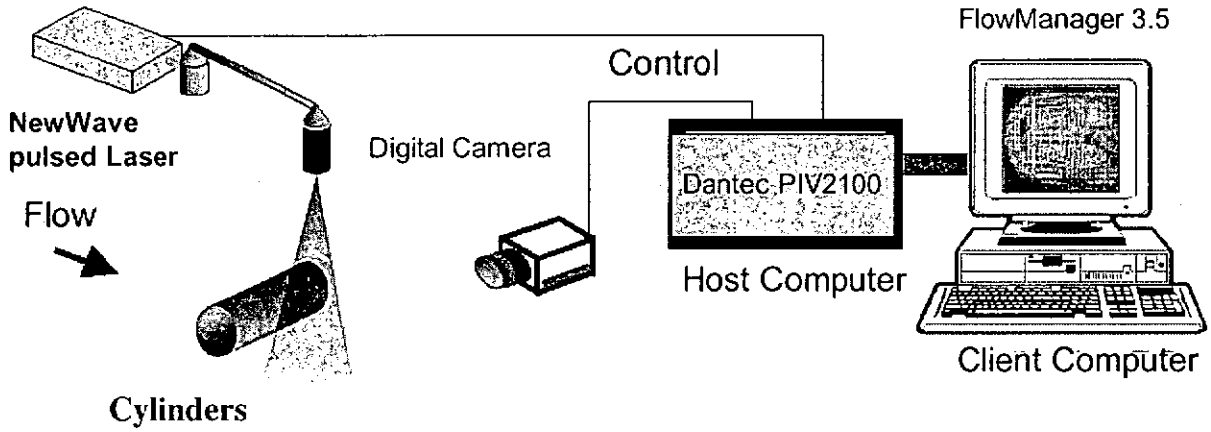

Figure 1-2 Typical PIV measurement using Dantec standard PIV2100 system

The velocity field was measured using a Dantec standard PIV2100 system. The flow was typically seeded by smoke, which was generated from Paraffin-oil, of a particle size around 1 μm in diameter. Flow was illuminated by two NewWave standard pulsed laser sources of a wavelength of 532nm, each having a maximum energy output of 120mJ. Two CCD cameras (HiSense type 13, gain × 4, double frames, 1280×1024 pixels) can be used to take digital particle images. A Dantec FlowMap Processor (PIV2100 type) was used to synchronize image-taking and illumination. Figure 1.2 presents a PIV setup. Flow visualization measurements were also carried out in the wind tunnel using the visualization function of Dantec PIV 2100 system.

1.5 Outline

The present work is to investigate fluid-structure interactions between flow, an oscillating cylinder, and a neighbouring cylinder. Measurements and analysis have been conducted. Chapter 1 has introduced the background of the present work and has surveyed the previous investigations relate to the present work. Experimental techniques employed in this work are briefed.

In Chapter 2, vortex street modes behind an isolated streamwise oscillating circular cylinder were investigated experimentally. Five typical vortex modes, S-I, S-II, A-I, A-III, A-IV are identified using LIF flow visualization. The dominant frequencies of the wake are measured using hot wire technique. Quantitative vorticity data are obtained using PIV. Mechanisms of vortex modes are discussed and prediction of S-II mode is conducted.

Interactions between a streamwise oscillating cylinder and a downstream cylinder are studied in Chapter 3. Experiments are carried out in both water tunnel and wind tunnel. Three typical flow regimes are identified using LIF flow visualization. They are examined quantitatively by means of PIV. Dominant frequencies of the wakes of two cylinders are examined using hot wires. Effects of Re, L/d, A/d, f_e/f_s on flow regimes are discussed.

In Chapter 4, interference between a stationary cylinder wake and that of a downstream streamwise oscillating cylinder is analyzed. Two typical flow regimes are addressed.

The effect of *Re* on the dominant frequencies of the two side-by-side cylinder wake in the asymmetrical flow regime is studied experimentally and discussed in Chapter 5. The relationship is examined between *T/d* and the critical *Re*, at which the transition from single to two streets occurs, shedding light upon the previous scattered reports on the detection of dominant frequencies.

In Chapter 6, two-dimensional coupled and nonlinear dynamic equations were established using Hamilton's principle. For the first time, an axial force effect on vortex induced vibrations is considered. Displacement, strain responses, and natural frequency of the fluid-cylinder system have been derived analytically using Mathematica© software.

Conclusions are summarized in Chapter 7.

CHAPTER 2

VORTEX STREET BEHIND A STREAMWISE OSCILLATING CYLINDER

2.1 Introduction

As stated in Section 1.2.1, previous studies have uncovered many important aspects of the physics associated with a streamwise oscillating cylinder wake, but the cylinder oscillation amplitude investigated has been relatively small ($A/d \leq 0.3$). Therefore, the present work aims to study the wake of a streamwise oscillating cylinder, focusing on the case of a relatively large A/d. A new flow structure S-II is observed experimentally for the first time. The effects of both f_e/f_s and A/d on the vortex street are investigated.

The experiment employs a laser-induced fluorescence (LIF) technique to visualise the flow structure behind the streamwise oscillating cylinder. The qualitative flow images are examined along with the quantitative flow field obtained using the particle image velocimetry (PIV). The dominant frequencies in the near wake are further examined based on hot-wire data. The fluid forces on the cylinder have been analyzed. The occurrence of the S-II mode flow structure has been predicted.

2. 2 Experimental Details

2. 2.1 LIF visualization in a water tunnel

The LIF measurements were carried out in a water tunnel, which has a square working section (0.15 m × 0.15 m) of 0.5 m long. The working section is made up of four 0.02 m thick perspex panels. A regulator valve controls the flow speed and the maximum velocity attained in the working section is about 0.32 m/s. Further details of the water tunnel can be found in Zhou *et al.* (2001).

An acrylic circular tube with a diameter of d = 0.01 m was horizontally mounted at the mid-plane of the working section. It was cantilever-supported; the gap between the cylinder tip and the working section wall was about 0.005 m. The cylinder, driven by a D.C. motor through a linkage system, oscillated harmonically in time in the streamwise direction. The motor was controlled by a microcomputer so that the oscillating frequency of the cylinder could be precisely obtained. The structural oscillation amplitude was fixed at A/d = 0.5, while f_e was varied up to a maximum of 2.8 Hz. This frequency was substantially smaller than the first-mode natural frequency, about 32 Hz, of the fluid-cylinder system. The frequency ratio obtained was $f_e/f_s = 0 \sim 3.1$.

Note that the cylinder has an aspect ratio of 15. For a stationary cylinder, an aspect ratio of 27 or larger is needed to avoid end effects (King 1977). However, an oscillating cylinder may re-organise the vortex shedding process to enhance significantly its two dimensionality. Griffin (1980) observed that, when the oscillation amplitude was greater than 0.01 - 0.02d, the correlation coefficient, ρ_p, between spanwise fluctuating pressures

increased greatly, compared with a stationary cylinder. For example, given a threshold of $\rho_p = 0.5$, the spanwise correlation length was about $1d$ at $A/d = 0.025$, $6d$ at $A/d = 0.075$ and $10d$ at $A/d = 0.125$. For $A/d = 0.5$, the correlation length was estimated to be over $40d$ based on an extrapolation of his data, indicating a negligible end effects in the present experiments.

Dye (Rhodamine 6G 99%), which has a faint red colour and will become metallic green when excited by a laser, was introduced at the mid-span of the cylinder through two injection pinholes located at 90°, clockwise and anti-clockwise, respectively, from the leading stagnation point. A thin laser sheet, which was generated by laser beam sweeping, provided illumination over $0 \leq x/d \leq 10$ in the vertical plane through the mid-span of the cylinder. A Spectra-Physics Stabilite 2017 Argon Ion laser with a maximum power output of 4 watts was used to generate the laser beam and a professional digital video camcorder (JVC GY-DV500E) was used to record the dye-marked vortex streets at a framing rate of 25 frames per second. A reference position was marked by a silver-coloured line on the water tunnel wall. Thus, the oscillation phase of cylinder can be estimated based on the relative position between cylinder and the reference line.

Measurements were carried out for Re ($\equiv U_\infty d/\nu$) = 100 to 600, where U_∞ is the free-stream velocity and ν is the kinematic viscosity.

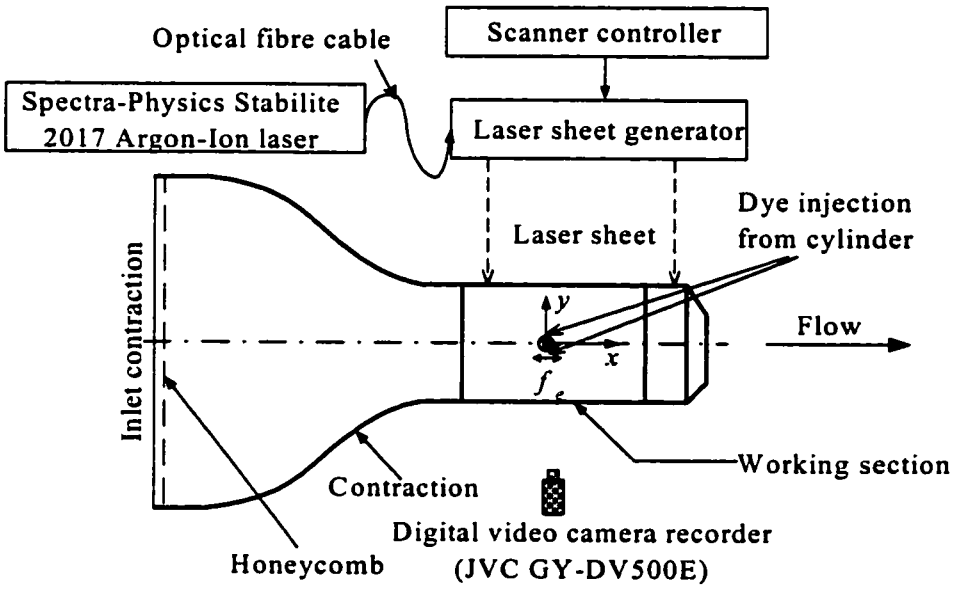

(a)

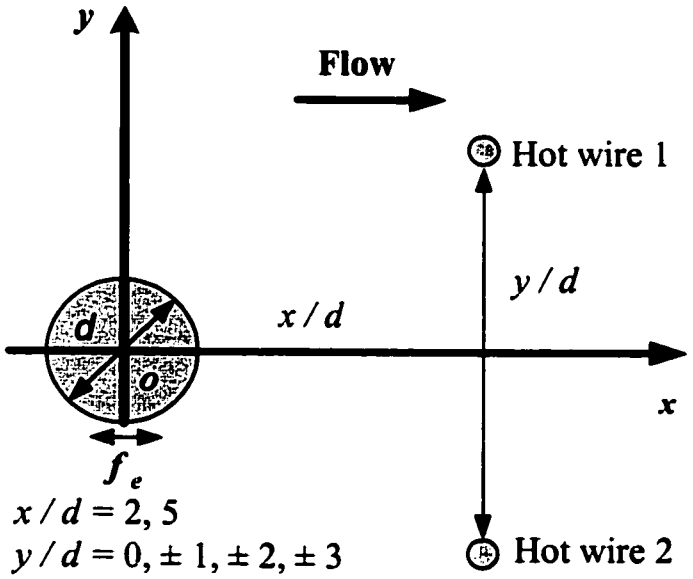

(b)

Figure 2-1 (a) Experimental set-up for flow visualization in a water tunnel. (b) Hot-wire arrangement in a wind tunnel.

2. 2. 2 PIV measurement in a wind tunnel

The PIV measurement was carried out in a closed-loop wind tunnel to obtain both qualitative and quantitative data. The wind tunnel has a square working section (0.6 m × 0.6 m) of 2.4 m in length. The view window of the working section was made of optic glass in order to maximize the signal-to-noise ratio in PIV measurements. The wind speed in the working section can be adjusted from about 0.3 m/s to 50 m/s.

The cylinder assembly was designed similarly to that used for the LIF measurements in the water tunnel. An aluminium alloy tube with a diameter of 0.015 m was cantilever-supported in the horizontal mid-plane of the working section. The length of the cylinder inside the wind tunnel was 0.35 m, thus resulting in a blockage of 1.25% and an aspect ratio of about 23. A 0.15 m long section from the free end of the cylinder was replaced using a transparent acrylic tube in order to allow the laser sheet to shine through, thus minimizing the shadow effects in the PIV measurement. One microcomputer-controlled DC motor system was used to drive the cylinder to oscillate. The oscillation amplitude varied from A/d = 0.5 to 0.67, and f_e/f_s ranged from 0 to a maximum of 1.5. The first-mode natural frequency of each cylinder was about 272 Hz, which is a factor of 12 times the maximum f_e (= 22Hz). To minimize the reflection noise generated by the laser sheet shining on the cylinder, the cylinder surface was painted black except a 0.02 m long section at 0.12 m from the free end on the acrylic section. In the free-stream, the streamwise turbulence intensity was measured to be approximately 0.4%. The velocity field was measured using a Dantec standard PIV2100 system. Flow was seeded by smoke, which was generated from Paraffin-oil, of a particle size around 1

μm in diameter. Flow was illuminated in the plane, 0.13 m from the free end of the cylinder, of mean shear by two NewWave standard pulsed laser sources of a wavelength of 532 nm, each having a maximum energy output of 120 mJ. It has been confirmed based on the streamwise mean and root mean square velocities (not shown) that the flow was two-dimensional around the plane. Digital particle images were taken using one CCD camera (HiSense type 13, gain × 4, double frames, 1280×1024 pixels). A Dantec FlowMap Processor (PIV2100 type) was used to synchronize image-taking and illumination. Each image covered an area of 0.115 m × 0.92 m of the flow field, i.e., $x/d = 0 \sim 7.7d$ and $y/d = -3.1d \sim +3.1d$; the x and y coordinates and their origin are defined in Figure 2-1b. The longitudinal and lateral image magnifications were identical, i.e. 0.09mm/pixel. Each laser pulse lasted for 0.01 μs. The interval between two successive pulses was typically 50 μs. Thus, a particle would only travel 0.05 mm (0.56 pixels or $0.003d$) at $U_\infty = 1.0$ m/s, at which the PIV measurement was conducted. An optical filter was used to allow only the green wavelength (532 nm) of the laser source to pass.

Since the cylinder was included in the PIV images, which could cause errors in deriving velocities around the cylinders, it was masked using a built-in masking function in the Dantec PIV2001 system before calculation of particle velocities. In the image processing, 32 × 32 rectangular interrogation areas were used. Each interrogation area included 32 pixels ($\approx 0.2d$) with 50% overlap with other areas in both the longitudinal and lateral directions. The ensuing in-plane velocity vector field consisted of 79 × 63 vectors. The same number of spanwise vorticity component, ω_z, may be approximately

obtained based on particle velocities. The spatial resolution for vorticity estimate was about 1.43 mm or 0.095d. The measurement was conducted at Re = 1150.

2. 2. 3 Hot wire measurement

The vortex shedding frequencies in the cylinder wake were measured using two hotwires in the wind tunnel. In order to determine the phase relationship between vortices shed from the different sides of the cylinder, two single hot-wires were placed symmetrically at x/d = 2, 5 and y/d = 0, ± 1, ± 2, ± 3, ± 4, respectively (Figure 2-1b). Constant-temperature circuits were used for the operation of the hot wires. Experiments were carried out for Re = 1150. Signals from the circuits were offset, amplified and then digitized using a 16 channel (12bit) Analog/Digital board and a personal computer at a sampling frequency $f_{sampling}$ = 1.5 kHz per channel. The typical duration of each record was about 30 s.

2. 3 Typical Flow Structures

When a structure oscillates, the structural oscillation and vortex shedding may be in the lock-on state or may not. The present investigation focused on the lock-on state. The wake of an isolated oscillating cylinder is dependent on a combination of A/d and f_e/f_s (Karniadakis & Triantafyllou 1989). For A/d = 0.5 ~ 0.7 and f_e/f_s = 0 ~ 3.1, five basic flow structures, S-I, S-II, A-I, A-III and A-IV, have been identified. Among these, S-II has not been reported before. The flow structures are classified based on Ongoren and Rockwell (1988b) and are discussed below.

2.3.1 S-I mode

For a relatively small f_e/f_s, one symmetric vortex street is formed behind the cylinder. Figure 2-2 presents sequential photographs of the street (A/d = 0.5, f_e/f_s = 0.59).The phase of cylinder oscillation is given in Figure 2-2f, where t and X represent time and the streamwise displacement from the reference position ($X = 0$) of the cylinder, respectively. During each cycle of structural oscillation, one pair of counter-rotating vortices forms symmetrically and separates from the cylinder, one from each side. The symmetric vortex formation was also observed by Ongoren and Rockwell (1988b) at A/d = 0.13 and $f_e/f_s \approx 1.0$, who referred to this vortex structure as S mode. It is well known that vortices are shed alternately from a stationary cylinder under the feedback effect of the wake. The present symmetrical vortex formation is apparently linked to the streamwise oscillation of the cylinder, which is predominant and the feedback effect from the wake is too weak to influence the symmetrical separation of free shear-layers from the cylinder.

The symmetric vortex street in Figure 2-2 appears unstable, breaking up quickly. Zhou et al. (2002) compared the wake of two side-by-side cylinders with that behind an isolated cylinder. At large centre-to-centre cylinder spacing, vortices were shed symmetrically from the two cylinders, forming two in anti-phase vortex streets. The vortices in the two streets decayed significantly faster than those in an anti-symmetrically arranged vortex street behind the isolated cylinder. Given the same lateral spacing between vortices, the symmetrically arranged vortices are expected to interact more vigorously than those anti-symmetrically arranged; vorticity cancellation between

oppositely signed vortices is more effective. As a result, the vortex street could be short-lived.

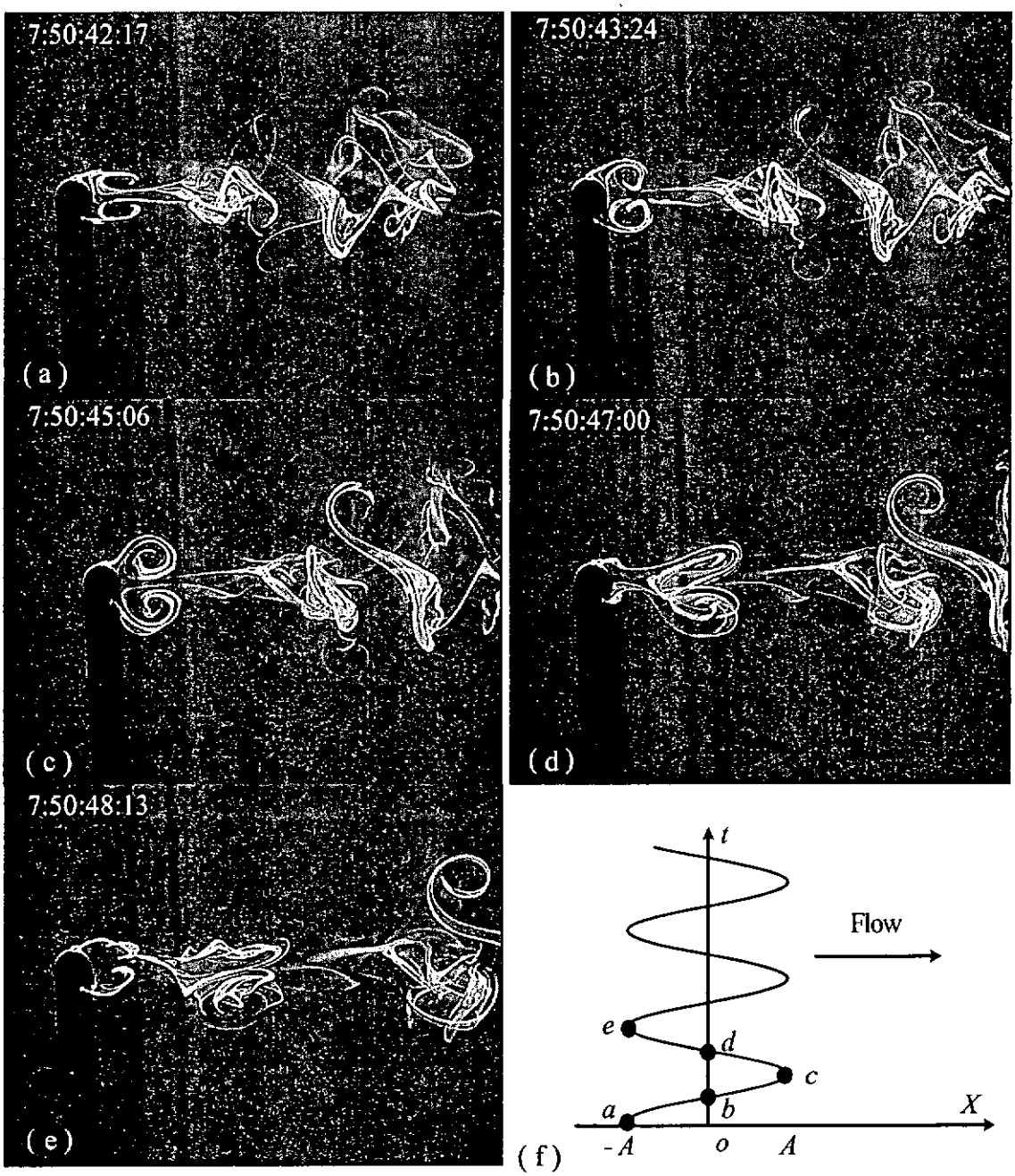

Figure 2-2 Sequential photographs of a symmetric street at $f_e/f_s = 0.6$, $Re = 164$ and $A/d = 0.5$.

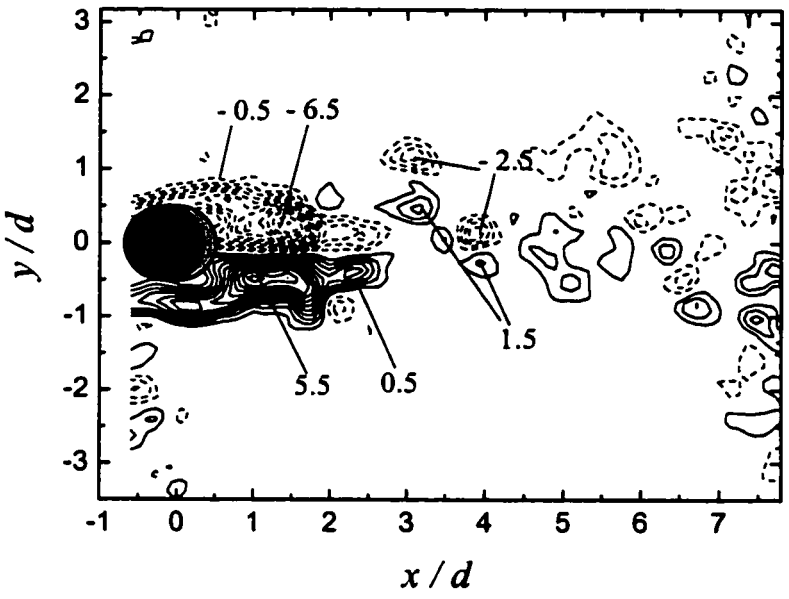

Figure 2-3 Instantaneous vorticity contours $\omega^* = \omega d/U_\infty$ obtained from the PIV measurement (the contour increment = 0.5, A/d = 0.67, Re = 1150 and $f_e/f_s = 0.5$).

This is supported by instantaneous vorticity contours $\omega^* = \omega d/U_\infty$ (Figure 2-3, A/d = 0.67 and f_e/f_s = 0.49). The dark and light grey circles indicate the existing and the next position of the cylinder, respectively, that is, the cylinder is moving along the flow direction. A pair of vortices occurs symmetrically behind the cylinder. Their strength is nearly the same. But the two vortices appear to be breaking up into pieces quickly.

2. 3. 2 A-I mode

As f_e/f_s is increased to 0.63 ~ 1.0, the flow structure changes; vortices are now shed anti-symmetrically from the cylinder, forming a staggered vortex street. The flow structure is illustrated in Figure 2-4 ($f_e/f_s = 0.63$. $A/d = 0.5$).

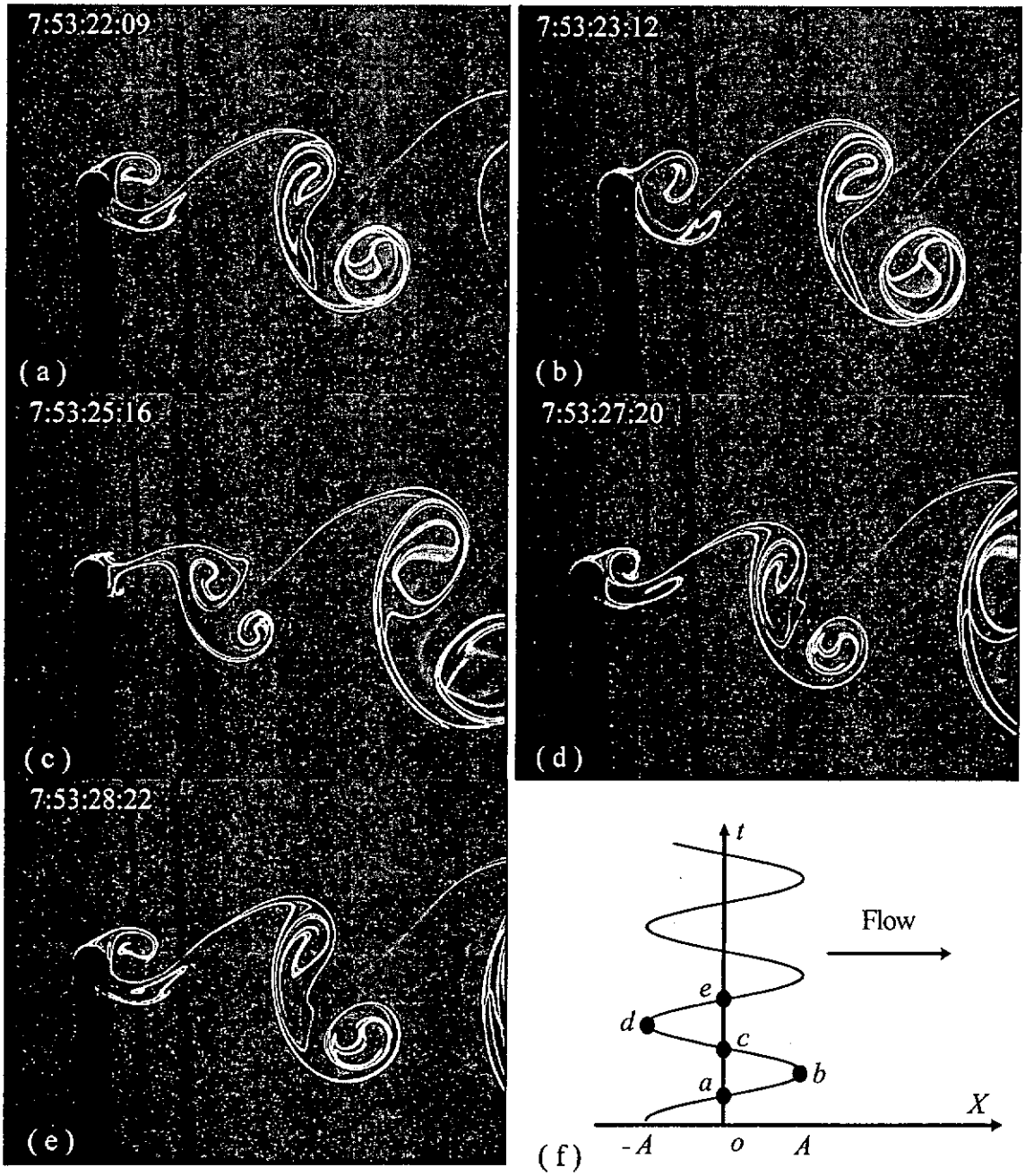

Figure 2-4 Sequential photographs of a staggered street at $f_e/f_s = 0.63$, $Re = 138$ and A/d = 0.5.

The LIF measurement indicates that the S-I mode and the A-I mode can coexist in the same experimental condition in terms of f_e/f_s and A/d. Note that the frequency ratio at which S-I and A-I modes occur is different from that ($f_e/f_s = 1.0 \sim 1.5$) observed by

Ongoren and Rockwell because of a difference in A/d, which should also influence the flow structure.

2. 3. 3 A-III mode

This mode of the flow structure occurs at a higher f_e/f_s and is characterised by one row of binary vortices and one row of single vortices. Each binary vortex consists of one pair of vortices.

Figure 2-5 presents a sequence of photographs for the A-III mode at $f_e/f_s = 1.33$ and $A/d = 0.5$. Due to interactions with the oscillation of the cylinder, the upper shear layer around the cylinder separates to form vortex A. This vortex crosses the wake centreline and merges with vortex B shed earlier from the lower side of the cylinder (Figures 2-5a ~ 5b), forming a binary vortex. Since A and B are formed from the shear layers of opposite vorticity, they are oppositely signed, which has been verified by examining the movement of flow markers (dye) on video. The interpretation is consistent with that of Ongoren and Rockwell (1988b).

Following the separation of vortex A, the upper shear layer of the cylinder separates again, before the lower shear layer, to form anther vortex C (Figures 2-5c ~ 5e). This vortex will not cross the centreline, forming the upper row of single vortices. Note that the asymmetrical nature of this flow structure implies a non-zero mean lift force on the cylinder.

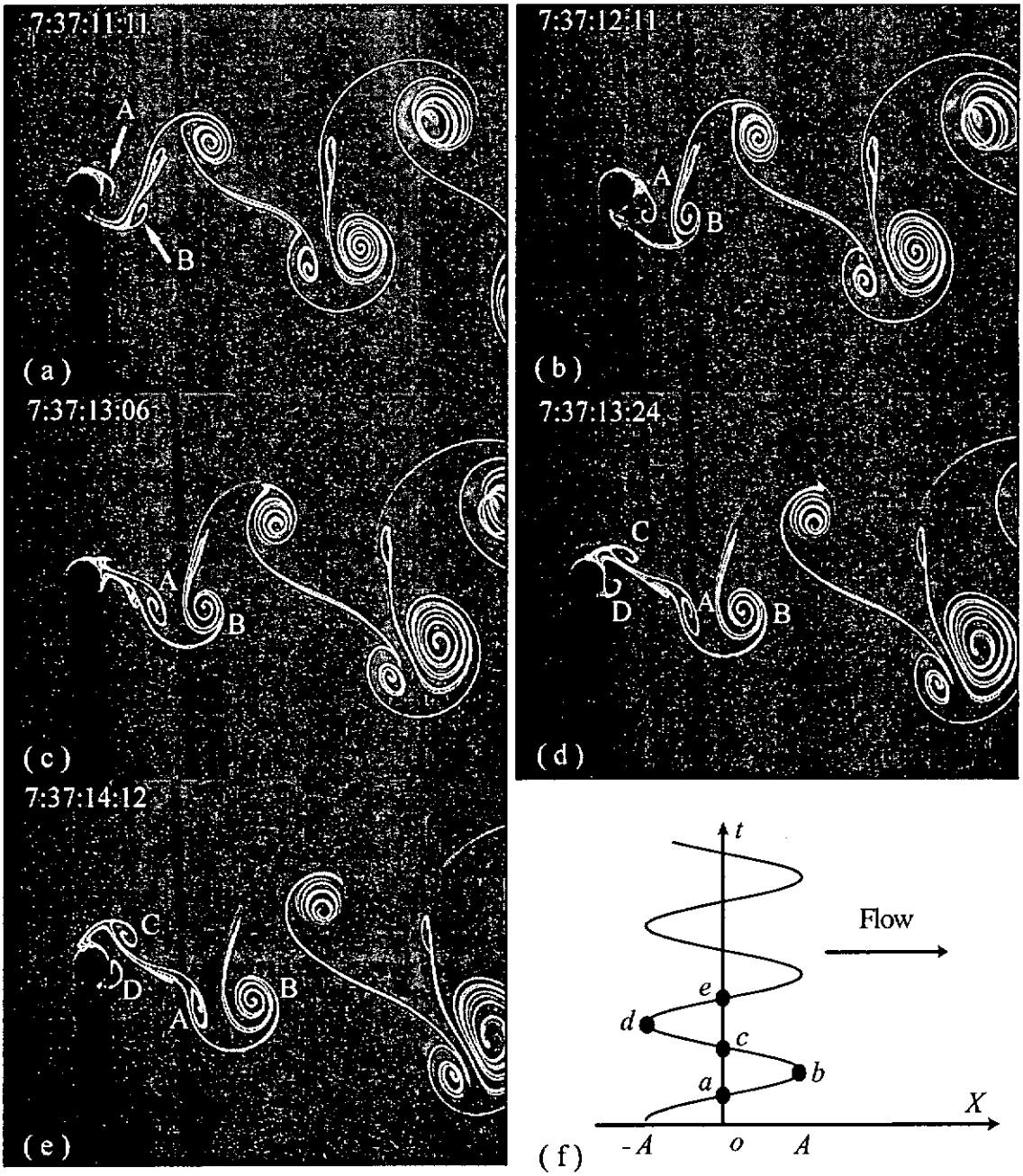

Figure 2-5 Sequential photographs of a staggered single-binary street at f_e/f_s = 1.3, Re = 138 and A/d = 0.5.

2. 3. 4 A-IV mode

As f_e/f_s increases to 1.39, one staggered binary vortex street is formed. The difference between the A-III and the A-IV mode is that vortices in both rows are binary

ones, each consisting of a pair of vortices. The formation process of the binary vortex is similar to the A-III mode. The upper shear layer around the cylinder separates to form vortex *A*, which crosses the centreline to join vortex *B* shed earlier from the lower side of the cylinder, forming one binary vortex in the lower row (Figures 2-6a ~ 6e).

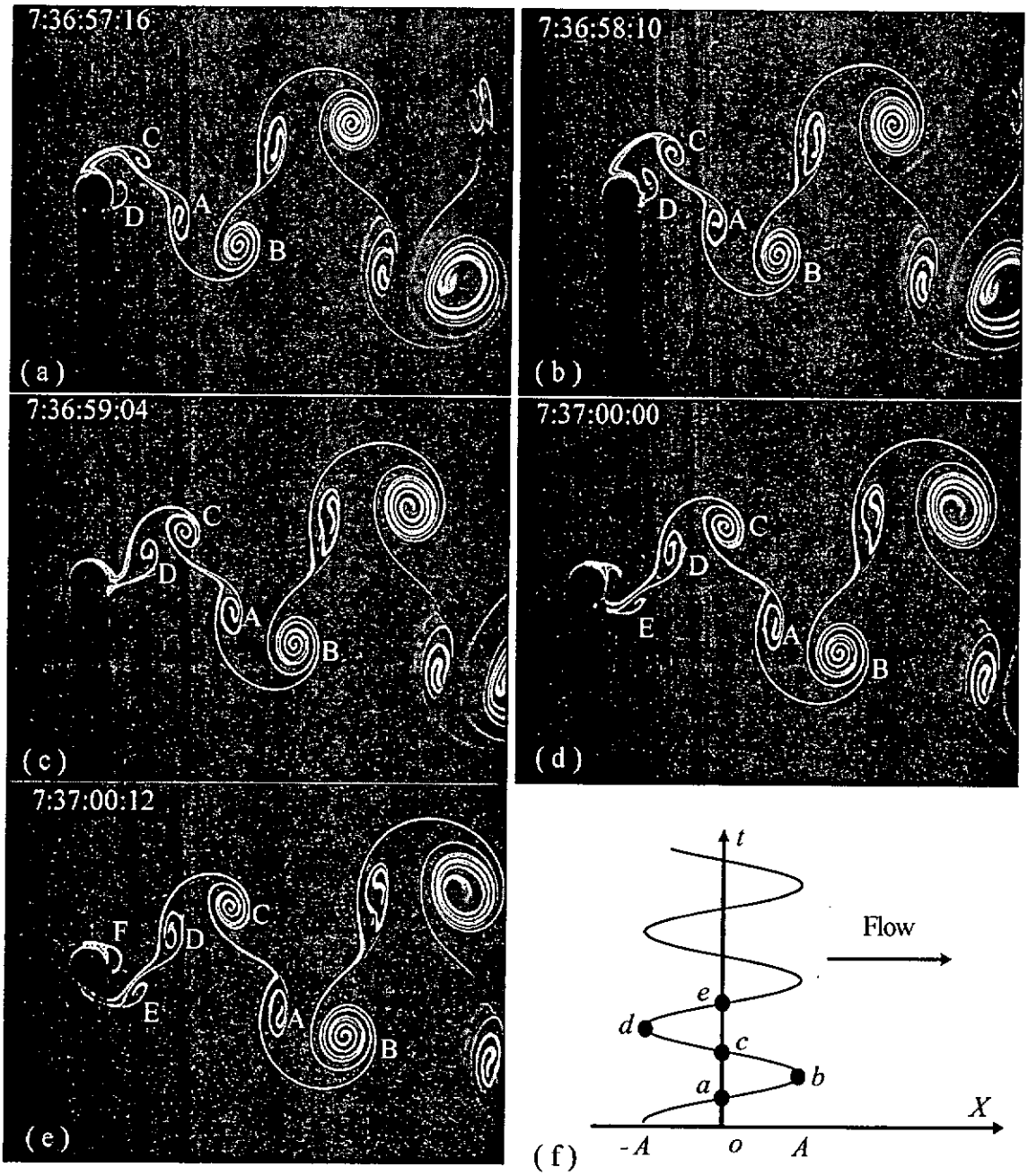

Figure 2-6 Sequential photographs of a stagger binary street at f_e/f_s = 1.4, *Re* = 138 and A/d = 0.5.

Following the separation of A, the upper shear layer generates another vortex C before the lower shear layer around the cylinder does. Unlike A, C stays above the wake centreline when advected downstream. Then, the lower shear layer separates to form a vortex D. This vortex crosses the centreline and joins C to form a binary vortex in the upper row (Figures 2-6a ~ 6e). Immediately after the formation of D, the lower shear layer around the cylinder generates another vortex E, which remains below the centreline as it evolves downstream. Similar to the binary vortex in the A-III mode, the two vortices in each binary vortex are counter-rotating.

2. 3. 5 S-II mode

For A/d = 0.5 ~ 0.7 and f_e/f_s = 0 ~ 3.1, five typical flow structures have been identified. Four of them were reported, though at a different combination of f_e/f_s and A/d, by Ongoren and Rockwell (1988b). One of the four displays two rows of vortices symmetrically arranged about the centreline, thus referred to as S-I mode (or S mode in Ongoren and Rockwell 1988b), while the other three consist of vortices anti-symmetrically arranged about the centreline, called A-I, A-III and A-IV mode, following Ongoren and Rockwell's categorisation. The four modes will be discussed further in Sction 2.5. At the higher range of f_e/f_s for the present A/d range, a symmetrically formed binary vortex street (Figure 2-7, 2-8, 2-9) occurs. This flow structure is apparently different from the S-I mode flow structure; it is composed of binary vortices. Each binary vortex encloses two counter-rotating vortices. We therefore refer to the flow structure as the S-II mode.

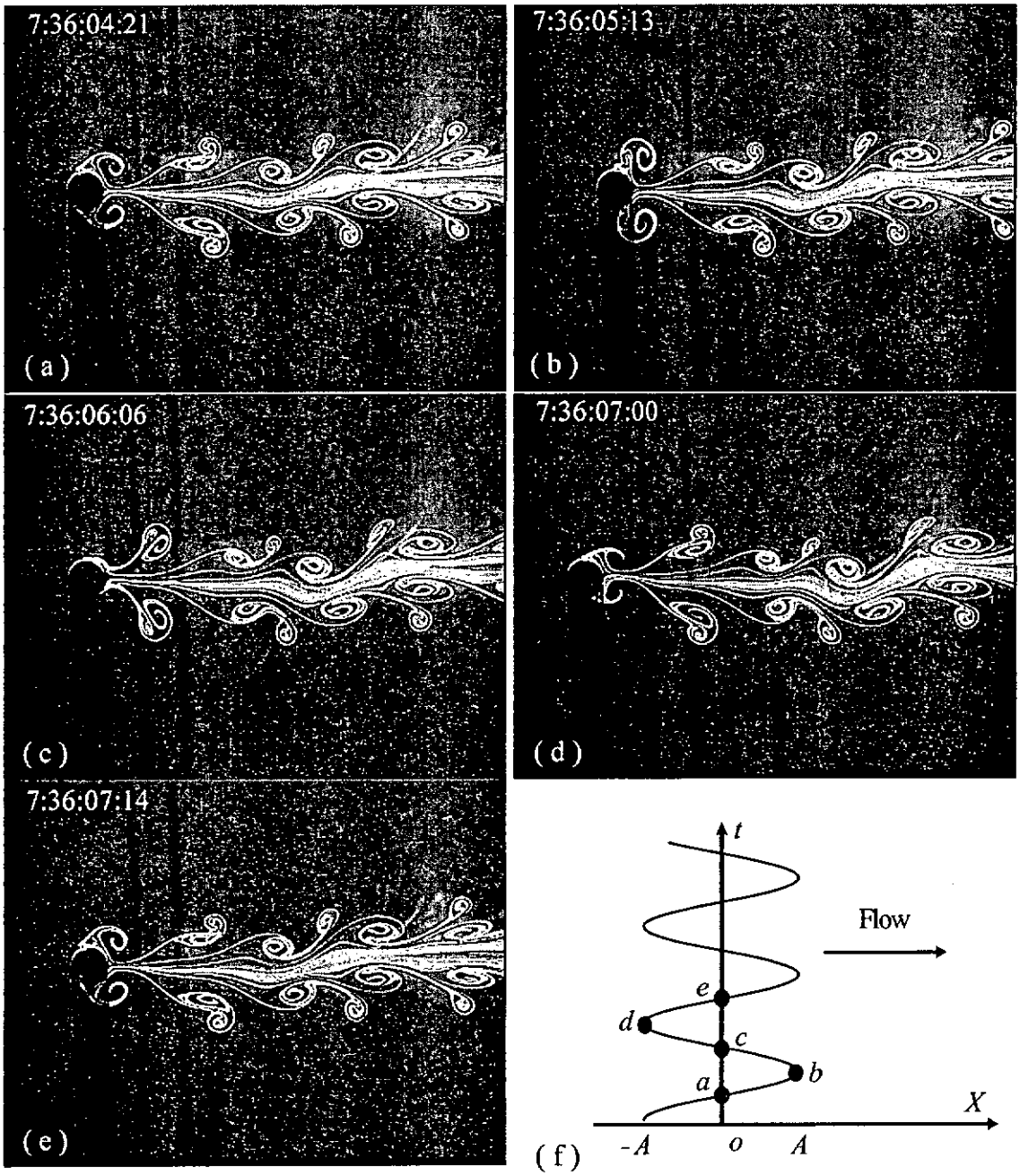

Figure 2-7 Sequential photographs of a symmetric binary vortex street at f_e/f_s = 1.6, Re = 130 and A/d = 0.5.

Figure 2-8 presents the sequential photographs of various phases in one typical cycle of the cylinder oscillation at f_e/f_s = 1.74 and A/d = 0.5. When the cylinder moves

oppositely to the flow direction (Figures 2-8a ~ 2-8c), one clockwise rotating vortex A_1 above the centreline forms due to the natural vortex shedding.

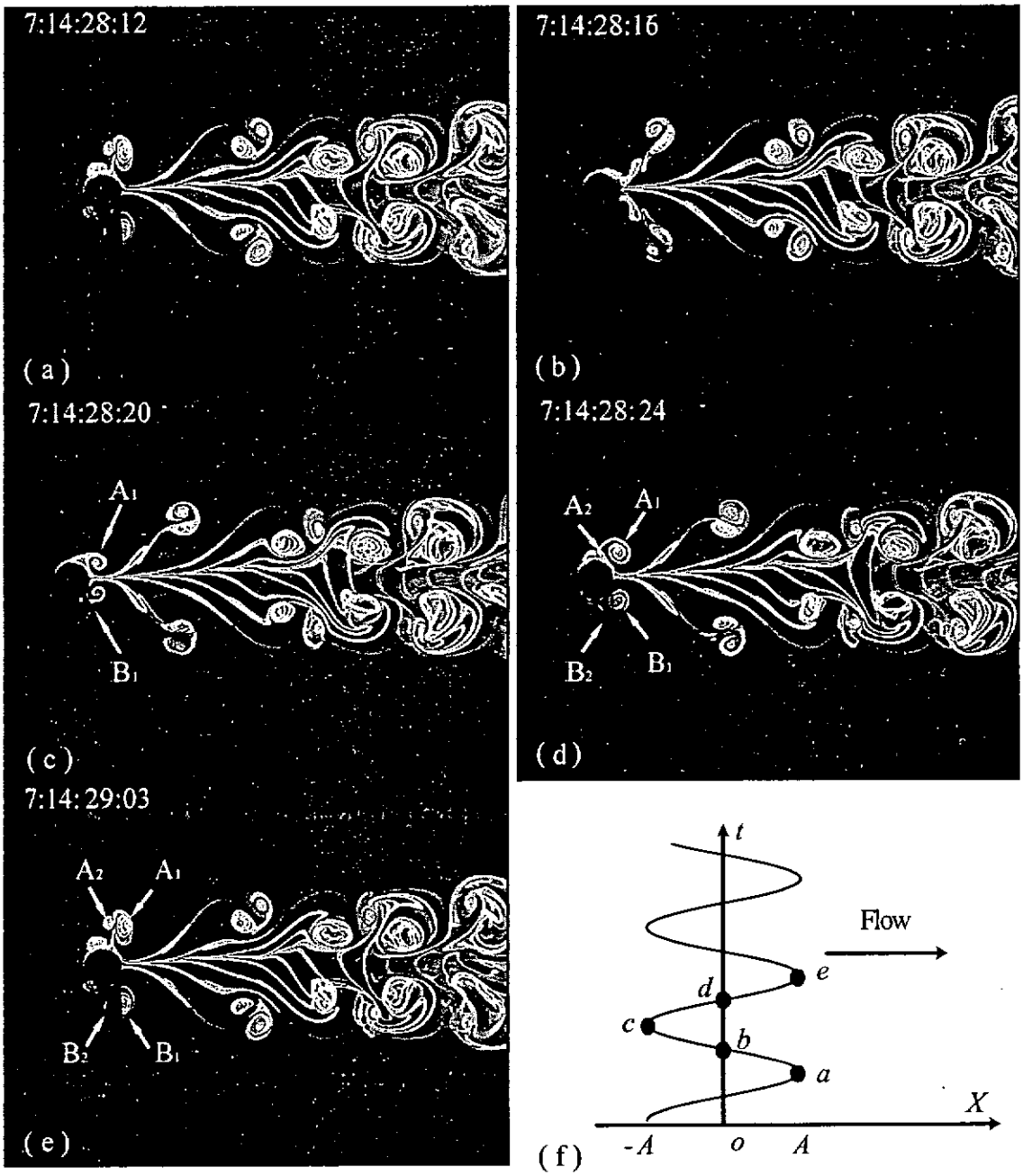

Figure 2-8 Sequential photographs of a symmetric binary vortex street at $f_e/f_s = 1.74$, $Re = 500$ and $A/d = 0.5$.

As the cylinder moves from - A to + A in the same direction as the flow (Figures 2-8c ~ 2-8e), the fluid near the cylinder wall moves along with the cylinder under the viscosity effect, but the fluid further away now moves oppositely (right to left) relative to the cylinder. The average moving velocity of the cylinder is about 3.2 cm/s (f_e = 1.566 Hz), while that of water was 4.5 cm/s. Thus, the maximum velocity of water relative to the cylinder is estimated to be about 0.53 cm/s, resulting in an instantaneous Reynolds number (based on this relative velocity and d) of 58, which exceeds the critical Reynolds number (≈ 40, e.g., Schlichting & Gersten 2000) for vortex shedding. Therefore, a vortex, A_2, of the anti-clockwise sense begins to form. Eventually, the structure containing a pair of counter-rotating vortices A_1 and A_2 separates from the cylinder (Figures 2-8c- 2-8e) and evolves downstream. At the same time, the counter-rotating vortices B_1 and B_2 form another binary vortex and separate from the lower side of the cylinder. The symmetric binary vortex street is also observed at a higher frequency ratio, up to the maximum f_e/f_s = 3.08 (Figure 2-9, Re = 500). Note that the increase in f_e/f_s appears to be causing transition from the laminar (Figures 2-7 and 2-8) to the turbulent state (Figure 2-9).

The flow structure is further evident in instantaneous vorticity contours $\omega^* = \omega d/U_\infty$ (Figure 2-10) obtained from the PIV measurement at A/d = 0.67, Re = 1150 and f_e/f_s = 1.45. In Figure 2-10a, the cylinder motion is right to left, generating clockwise (negative vorticity) and anti-clockwise (positive vorticity) rotating vortices above and below the centreline, respectively. The two structures apparently correspond to vortices A_1 and B_1, in Figure 2-8, respectively. In Figure 2-10b, the cylinder moves left to right. Two binary vortices, each consisting of a pair of counter-rotating vortices, simultaneously spring off

the upper and lower side of the cylinder, respectively, corroborating the observation from the LIF data (Figure 2-8).

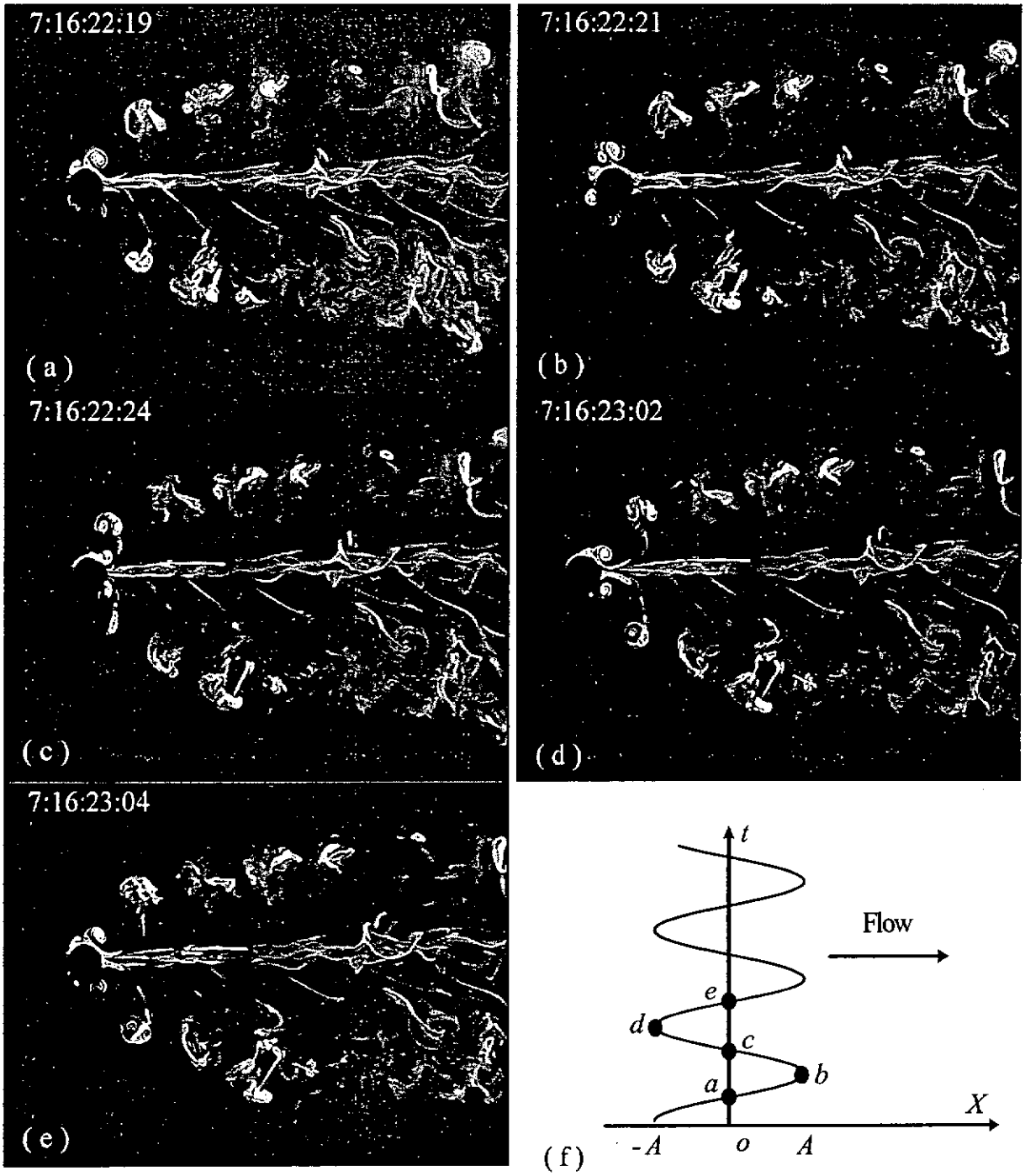

Figure 2-9 Sequential photographs of a symmetric binary vortex street at $f_e/f_s = 3.1$, $Re = 500$ and $A/d = 0.5$.

The normalized vorticity $\omega^*(\equiv \omega d / U_\infty)$ indicates that the downstream vortex, originating from the natural vortex shedding, in the binary vortex is slightly stronger than the upstream one, generated due to the cylinder oscillation. Unless otherwise stated, the asterisk denotes the normalization by d and U_∞ in this dissertation.

Note that the binary vortices appear relatively short-lived and barely identifiable for $x/d > 5$, in qualitative agreement with the LIF data in the turbulent state (c.f., Figure 2-9). This could be largely attributed to a more meandering motion of vortices in the turbulent state, thus accelerating vorticity cancellation between the counter-rotating vortices in a binary vortex.

The frequency of binary-vortex shedding is identical to that of the oscillation. This is evident in the power spectral density function (Figure 2-11) of the hot wire data measured at $x/d = 2$ at the same condition as the PIV measurement (Figure 2-10), which displays one pronounced peak at $f/f_e = 1.0$ across the wake. The spectral phase (not shown) between the signals from the two symmetrically arranged hot-wires is about zero at $f/f_e = 1.0$, further supporting the symmetrical arrangement of binary vortices (Figures 2-7, 2-8 and 2-9).

Another less pronounced peak occurs at $f/f_e = 2.0$. The latter peak is only discernible when the hot wire was placed far away from the centreline ($y/d = 3$), consistent with the lateral location (Figure 2-9) of the binary vortex in a turbulent state. The peak at $f/f_e = 2.0$ is therefore probably due to the fact that each binary vortex includes two vortices.

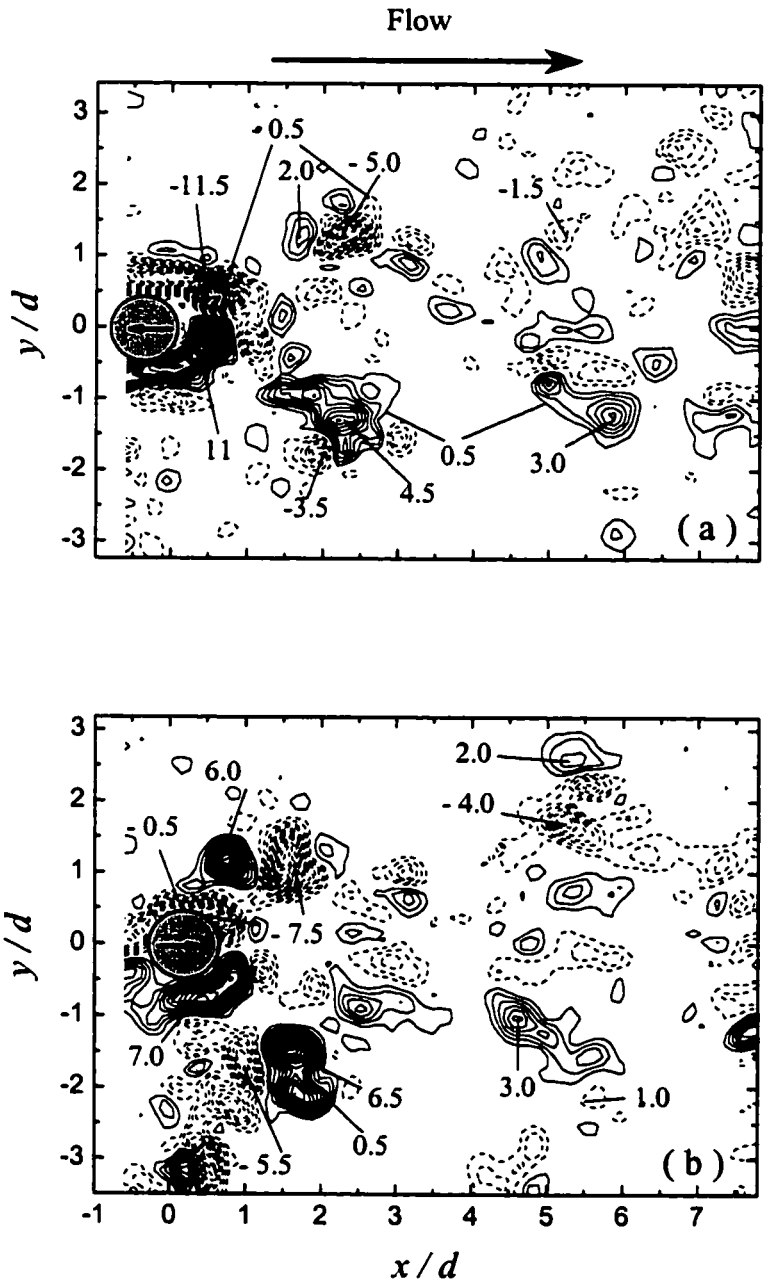

Figure 2-10 Instantaneous vorticity contours $\omega^* = \omega d/U_\infty$ obtained from the PIV measurement (the contour increment = 0.5, $A/d = 0.67$, $Re = 1150$ and $f_e/f_s = 1.45$). (a) The cylinder moves right to left. (b) The cylinder moves left to right.

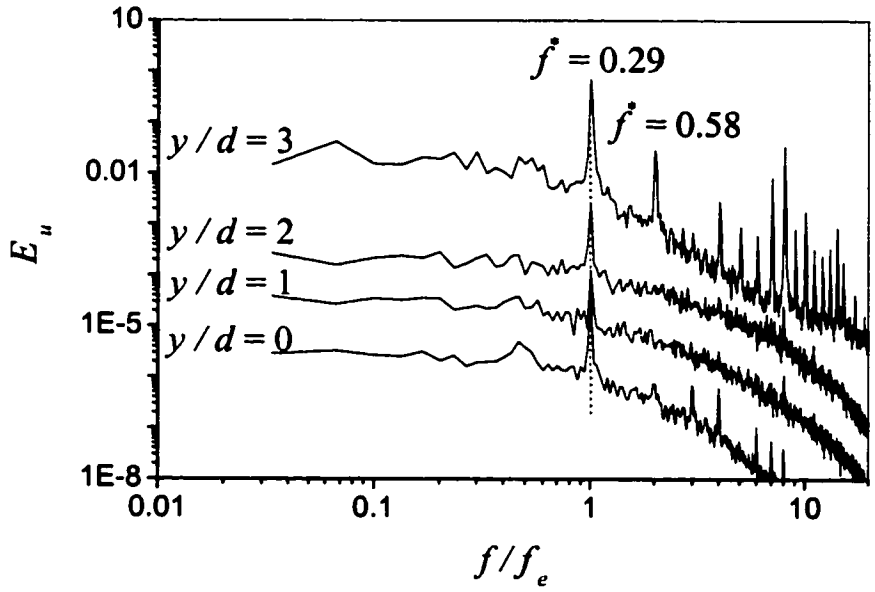

Figure 2-11 Power spectral density function of hot-wire signals obtained at $x/d = 2$. $A/d = 0.67$, $f_e/f_s = 1.45$ and $Re = 1150$.

2. 4 Mechanisms of the symmetrically formed vortex street

For a stationary cylinder, vortex shedding is controlled by the base pressure and feedback from the wake; the feedback mechanism may result in the transverse oscillation of the wake (Karniadakis and Triantafyllou 1989), contributing to the alternate vortex shedding. When the cylinder is forced to oscillate, the cylinder motion gives rise to an additional force on fluid. The streamwise force per unit cylinder length is given by Naudascher (1987):

$$F_X(t) = -\frac{1}{2}\rho A_c U_\infty^2 (1 - \frac{\dot{X}}{U_\infty})^2 C_D + \rho_s A_c \ddot{X}, \qquad (2\text{-}1)$$

where C_D is the drag coefficient, A_c is the cross-sectional area of the cylinder, $\dot{X} = 2\pi f_e A \cos 2\pi f_e t$ (where t is time) is the instantaneous velocity of the oscillating cylinder. Equation (1) can be rewritten as

$$F_X(t) = -\frac{1}{2}\rho A_c U_\infty^2 C_D - \frac{1}{2}\rho A_c C_D \dot{X}^2 + \rho A_c C_D \dot{X} + \rho_s A_c \ddot{X} = -F_{Xs} - F_{Xn} - F_{XI} - F_{XI} . \quad (2\text{-}2)$$

In (2-2), $F_{Xs} = \frac{1}{2}\rho A_c U_\infty^2 C_D$ is the steady drag force; $F_{Xn} = \frac{1}{2}\rho A_c C_D \dot{X}^2 = 2\pi^2 \rho A_c C_D St^2 U_\infty^2 (A/d)^2 (f_e/f_s)^2 \cos^2 2\pi f_e t$ is a non-linear force, where St is the Strouhal number. They both directed along the free stream direction. $F_{XI} = 4(\pi St U_\infty)^2 \rho_s (A_c/d)(f_e/f_s)^2 (A/d) \sin 2\pi f_e t$ is the inertia force, acts on the fluid nearby the upstream/downstream surface of the cylinder; $F_{XI} = -\rho A_c C_D \dot{X} = -2\pi\rho A_c C_D St U_\infty (A/d)(f_e/f_s) \cos 2\pi f_e t$ is the linear damping force, either negative or positive, following the direction of the cylinder motion. The magnitudes of F_{XI}, F_{XI} and F_{Xn} depend on f_e/f_s and A/d. They act on the cylinder symmetrically about the centreline, thus promoting the symmetrical vortex shedding. When f_e/f_s is small for a given A/d (or A/d is small for given f_e/f_s), F_{XI}, F_{XI} and F_{Xn} may be insignificant, compared with the wake feedback effect. This may explain the observation that at relatively low f_e/f_s, the S-I mode is unstable. For example, for $f_e/f_s < 2$ and $A/d = 0.13$, the S-I mode co-exists with those staggered modes, i.e., A-I, A-III or A-IV, and occurs only over a limited number of oscillation cycles; but for $f_e/f_s > 3$ at the same A/d, the S-I mode is quite stable (Ongoren and Rockwell, 1988b) due to an increasing F_{XI}, F_{XI} and F_{Xn} effect, so is the S-II mode, which occurs at an even higher f_e/f_s.

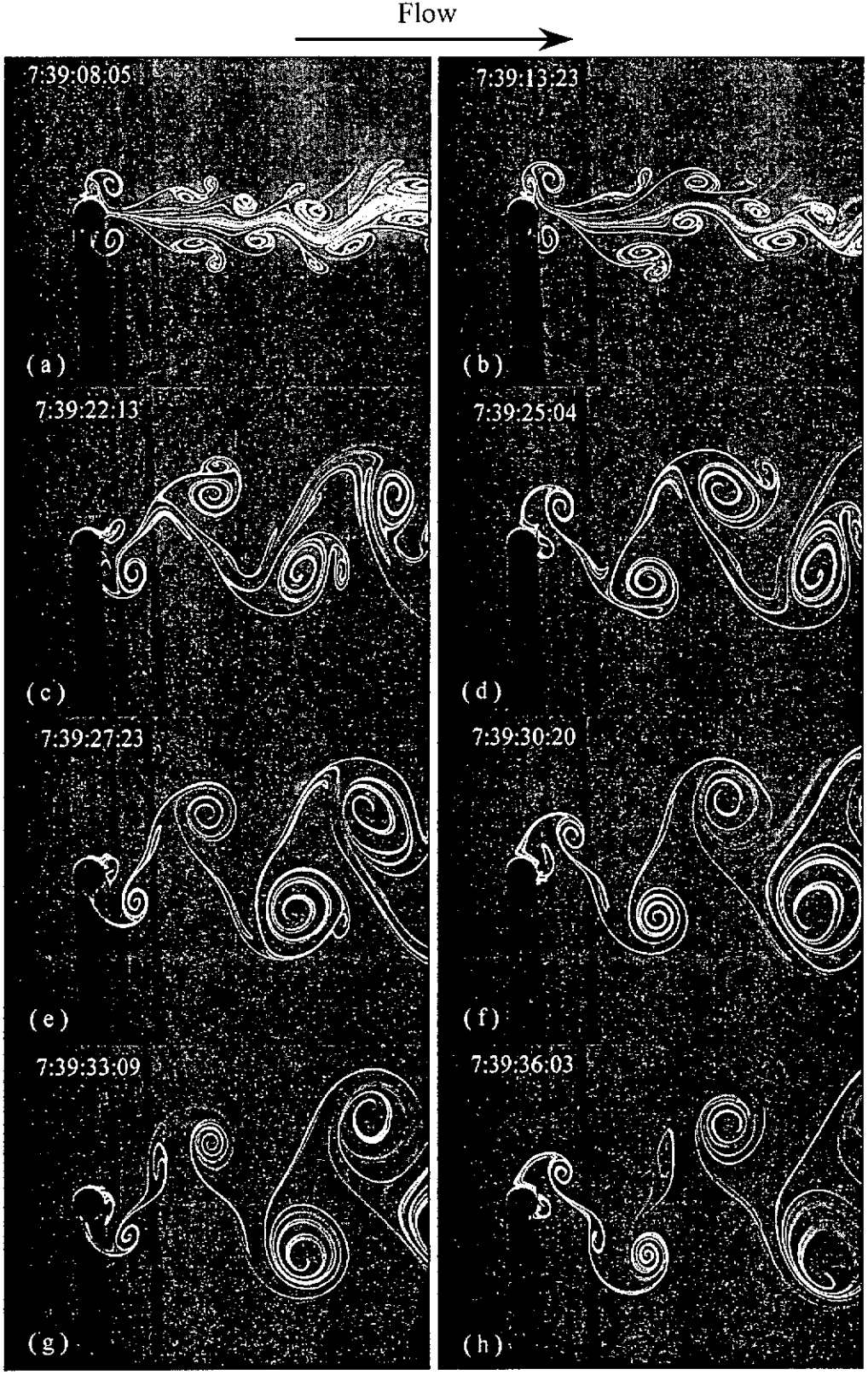

Figure 2-12 Variation from S-II (a) to A-I (e, f), A-III (g) and A-IV mode (h) as f_e/f_s varied slowly from 1.6 in (a) to 1.3 in (h). The cylinder position is at $X = A$. $A/d = 0.5$, $Re = 130$.

The influence of f_e/f_s or the non-linear force and linear damping force on the flow structure can be vividly demonstrated. Figure 2-12 presents sequential photographs when f_e/f_s was adjusted slowly from 1.6 to 1.3 at A/d = 0.5 and Re = 130. During this course, other flow conditions such as Re, A/d, surface roughness of cylinder, etc. were kept unchanged. As f_e/f_s reduced, F_{XI}, F_{XI} and F_{Xn} decreased and their control on the symmetric boundary separation diminished. Consequently, the wake feedback gained control, resulting in the alternate vortex shedding; the flow structure changed from the S-II mode to the A-I (Figure 2-12e-f), A-III (Figure 2-12g) and finally to the A-IV mode (Figure 2-12h).

2. 5 Effect of Frequency and Amplitude Ratios

2. 5.1 Dependence of the flow structure on f_e/f_s and A/d.

Figure 2-13 presents a collection of data available in the literature and those presently obtained. Evidently, the mode of a flow structure can depend on both f_e/f_s and A/d. For example, the flow structure of the A-I mode occurs from f_e/f_s = 1.76 to 2.2 for A/d = 0.06 (Griffin and Ramberg, 1976) and from f_e/f_s = 1.0 to 1.5 for A/d = 0.12 or 0.13 (Ongoren and Rockwell, 1988b). However, the present data shows the occurrence of A-III mode at $f_e/f_s \approx$ 1.3 for A/d = 0.5 and the S-II mode for $f_e/f_s \gtrsim$ 1.6 and A/d = 0.5. In general, for a larger A/d, f_e/f_s is smaller where a particular flow structure mode concerned starts to occur. For a fixed A/d, the S-I mode occurs at the lowest f_e/f_s, followed by the A-I, A-III and A-IV modes as f_e/f_s increases. The S-II mode occurs at the highest f_e/f_s among the five modes.

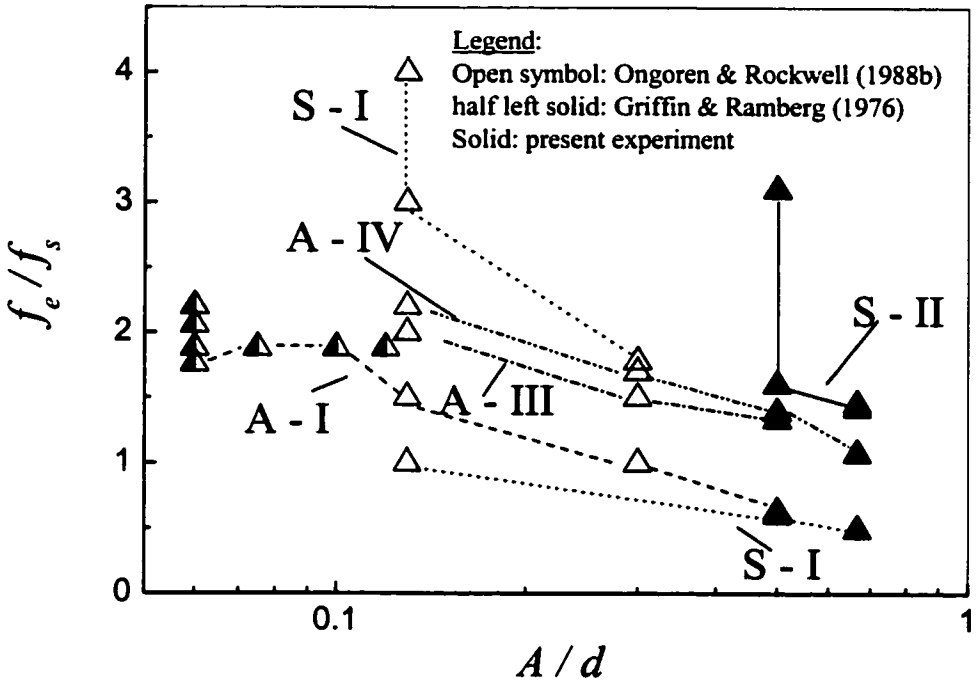

Figure 2-13 Dependence of the flow structure on f_e/f_s and A/d.

2. 5. 2 Prediction for the occurrence of S-II mode

Analysis is presently developed to predict the occurrence of the S-II mode partly because this flow structure is a new finding and partly because the flow consists of a remarkably formed binary vortex street. It is well known that, for a stationary cylinder, the creeping flow regime (no flow separation) occurs for $Re < 5$. For $5 < Re < 40$, the shear layers around the cylinder steadily separate and merge downstream, forming a symmetric and steady twin vortex or closed near-wake (e.g., Zdravkovich 1997; Schlichting & Gersten 2000). The twin vortex is re-circulating in the near wake. For $Re >$ 40, the closed near-wake starts to become unstable and oscillate transversely. The vortex

will separate from the cylinder if Re continues to be increased. For each flow regime, there is a critical Reynolds number. When Re reaches this critical value, the corresponding flow regime occurs.

The critical Reynolds number to form a vortex re-circulating in the near wake is $Re_c \approx 5$. Presumably, the same critical Reynolds number applies in the case of a streamwise oscillating cylinder, though Re_c has to be based on the relative velocity ΔU between the cylinder and fluid around it. When A/d is fixed, the relative velocity could be directed opposite to the free-stream velocity at a large f_e/f_s. As discussed in Section 2.3, the downstream vortex within a binary vortex is formed due to the natural vortex shedding and the upstream one occurs during the cylinder movement from $-A$ to A. In view of a harmonic cylinder oscillation, the cylinder displacement may be written as

$$X(t) = A\sin 2\pi f_e t,$$

where t is time. The cylinder velocity is then given by

$$\dot{X}(t) = 2\pi A f_e \cos 2\pi f_e t.$$

It can be inferred that the maximum velocity of the cylinder occurs at $X = 0$, viz.,

$$\dot{X}_{\max} = 2\pi A f_e. \tag{2-3}$$

For the oscillating cylinder, the Reynolds number Re_r based on ΔU needs to exceed Re_c to form a re-circulating vortex, namely,

$$\mathrm{Re}_r = \Delta U d / \nu \geq \mathrm{Re}_c. \tag{2-4}$$

Let us consider the case when ΔU is opposite to the free-stream velocity, that is,

$$\Delta U = \dot{X}_{\max} - U_\infty = 2\pi A f_e - U_\infty. \tag{2-5}$$

Noting $U_\infty = \nu \mathrm{Re}/d$, combining (2-5) and (2-4) yields

$$f_e \geq \frac{\nu(\mathrm{Re}+\mathrm{Re}_c)}{2\pi A d}. \tag{2-6}$$

Dividing (2-6) by $f_s = \frac{U_\infty St}{d}$, one obtains

$$f_e / f_s \geq \frac{(1+\frac{\mathrm{Re}_c}{\mathrm{Re}})}{2\pi St}\left(\frac{A}{d}\right)^{-1}, \tag{2-7}$$

where St is the Strouhal number in a stationary cylinder case, which may depend on Re for a small Re, that is, $St = St(Re)$. Thus, Equation (2-7) may be rewritten as

$$f_e / f_s \geq \frac{(1+\frac{\mathrm{Re}_c}{\mathrm{Re}})}{2\pi St(\mathrm{Re})}\left(\frac{A}{d}\right)^{-1} = (f_e/f_s)_c, \tag{2-8}$$

where $(f_e/f_s)_c$ is the threshold number for the occurrence of the S-II mode flow structure. The relationship $St = St(Re)$ is well documented in the literature (e.g., Chen 1987, Blevins 1994). Based on (2-8), f_e/f_s is inversely proportional to A/d, in qualitative agreement with the observation from the experimental data (Figure 2-13) that, as A/d increases, the S-II mode starts to occurs at a smaller f_e/f_s. In the limiting cases, if A approaches infinite (e.g., towing a cylinder through a water tank), f_e/f_s approaches zero; if $A = 0$ (a stationary cylinder), $f_e/f_s = \infty$, that is, it is impossible to generate the binary vortex.

When Re is larger than 250, $St\ (Re) \approx 0.2$, $Re_c/Re \approx 0$ ($Re_c = 5$), the Re effect on the generation of the binary vortex should be negligible. Eq. (2-8) can be then simplified as

$$f_e / f_s \geq (f_e / f_s)_c \approx \frac{5}{2\pi}\left(\frac{A}{d}\right)^{-1}. \tag{2-9}$$

Eq. (2-8) or (2-9) is the condition to form the flow structure of the S-II mode.

Figure 2-14 presents the prediction chart based on eq. (2-8), along with experimental data available. The symmetric binary vortex structure occurs in the region above the curve. The open symbols represent the flow structures of S-I, A-I, A-III and A-IV modes experimentally observed, while the solid symbol indicates the occurrence of S-II mode. A number of comments can be made based on the chart:

1 The predicted occurrence of the S-II mode is in good agreement with the available experimental and simulated data.

2 As *Re* increases at a step of 50, the curve translates downwards, indicating a dependence of the occurrence of the S-II mode on *Re*. But the translating increment becomes smaller and smaller as *Re* increases, suggesting a diminishing *Re* effect, in particular for $Re > 250$.

3 At $A/d = 0.13$, f_e/f_s has to be greater than 6.0 to form the flow structure of the S-II mode, while at $A/d = 0.3$, f_e/f_s needs to exceed 2.7. This may explain why Ongoren and Rockwell (1988b) failed to observe the S-II mode (their f_e/f_s was up to 4 at $A/d = 0.13$ and did not exceed 1.8 at $A/d = 0.3$).

4 Other than *Re*, the occurrence of the S-II mode may depend on initial conditions such as turbulence level, roughness of cylinder, neighbouring structures such as cylinders, walls, and so on.

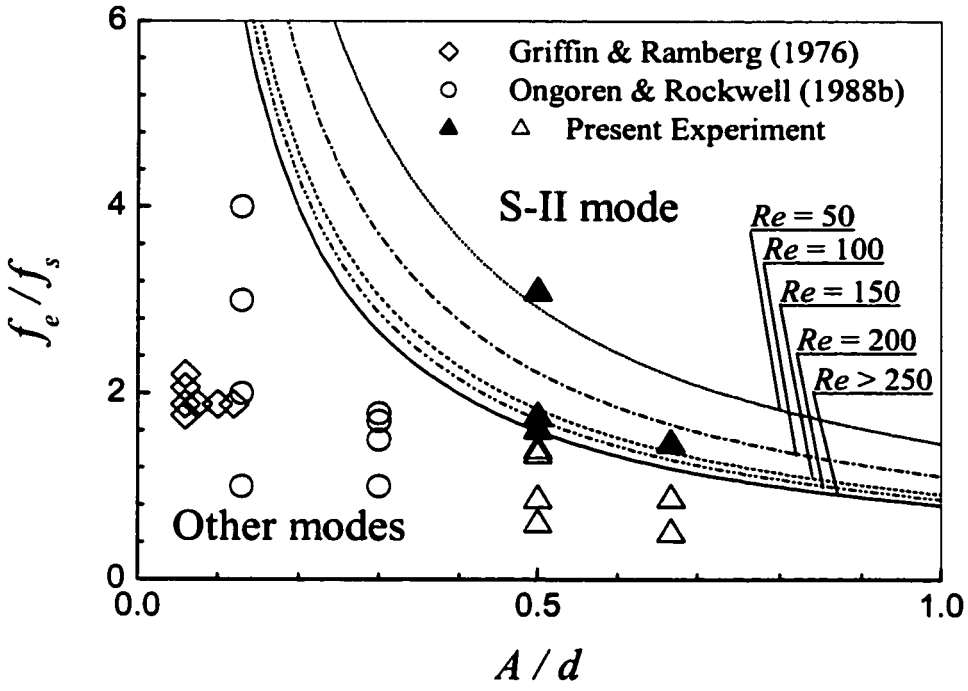

Figure 2-14 Prediction of the flow structure of the S-II mode.

2. 6 Conclusions

The wake of a streamwise oscillating cylinder has been experimentally investigated using the LIF, PIV and hot-wire techniques. The flow structure depends on both f_e/f_s and A/d. Five distinct modes of flow structures have been identified over a range of $0 < f_e/f_s < 3.08$ and $A/d = 0.5 \sim 0.67$, i.e., S-I, A-I, A-III, A-IV, S-II as illustrated in Figure 2-15.

The flow structure of the S-II mode is experimentally observed for the first time. It consists of two rows of binary vortices symmetrically arranged about the wake centreline.

Each binary vortex embraces two counter-rotating vortices sprung off from the same side of the oscillating cylinder, in distinct contrast with the counter-rotating vortex pairs in A-III and A-IV modes, which are shed from the different sides of the cylinder (Ongoren and Rockwell 1988b).

The analysis of forces of the oscillating cylinder on fluid indicates that a non-linear force and a linear damping force generated by the streamwise cylinder oscillation is probably responsible for the occurrence of the symmetrical vortex shedding. The mode of the flow structure could depend on the wake feedback mechanism as well as the two forces. Since the two forces are small if f_e/f_s is low for a given A/d, the wake feedback effect is dominant, resulting unstable S-I mode. As f_e/f_s increases, the two forces may overwhelm the wake feedback mechanism, thus inducing stable symmetrical boundary layer separation and forming a symmetric vortex street, the S-I or S-II mode. The analysis is consistent with previous observation that the movement-induced control was largely dependent on the combination of A/d and f_e/f_s (Karniadakis & Triantafyllou 1989).

Analysis has been conducted to predict the occurrence of the S-II mode flow structure. The critical frequency ratio, $(f_e/f_s)_c$, for the S-II mode to occur is inversely proportional to A/d and dependent on Re. The Re effect is negligible for $Re > 250$. The prediction is in excellent agreement with experimental data.

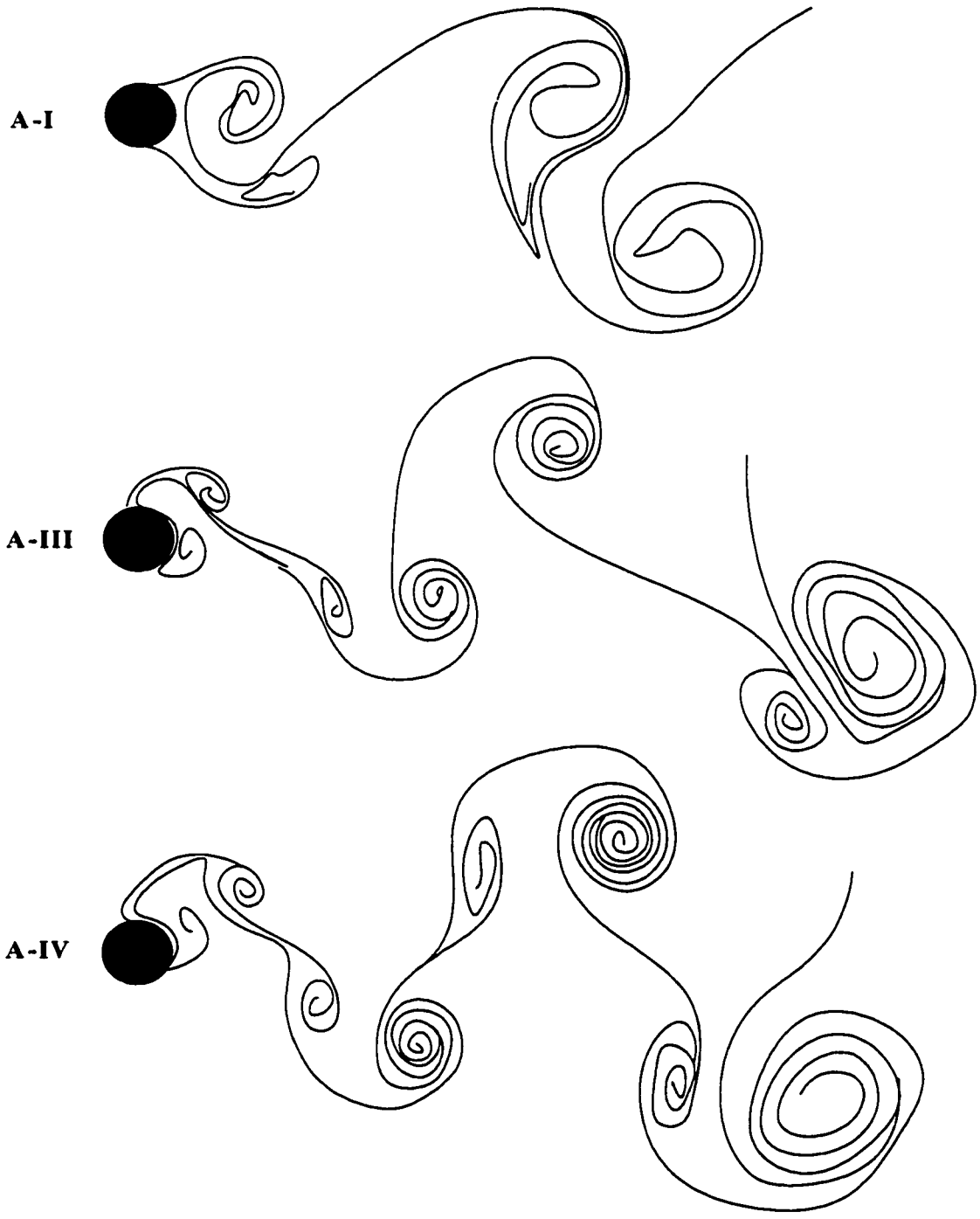

(a)

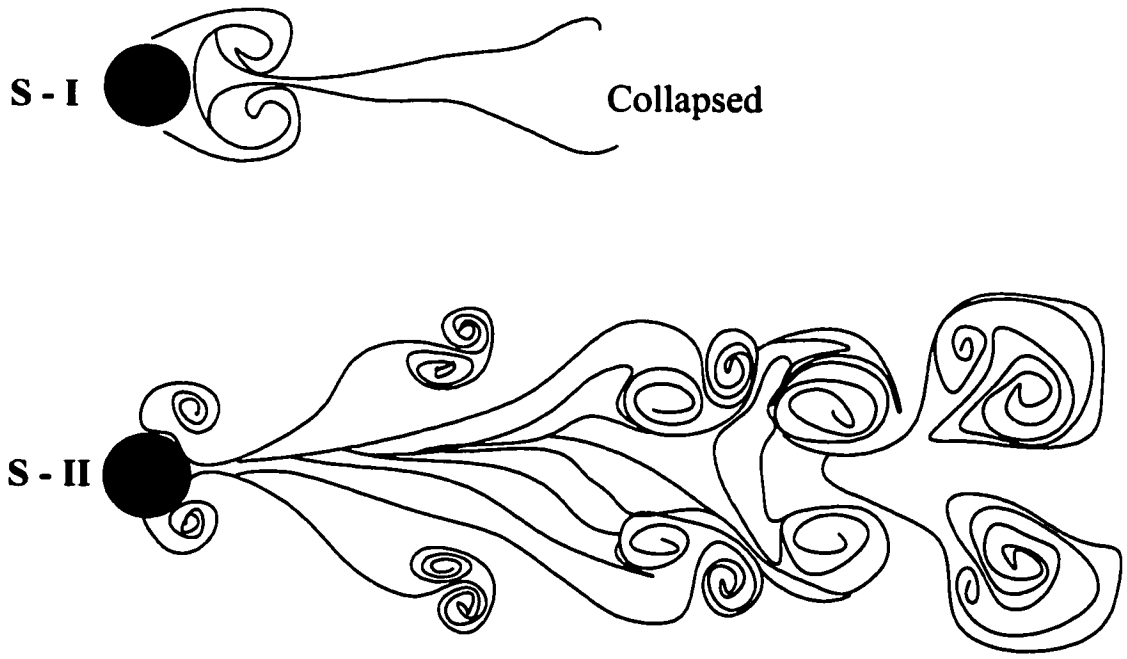

(b)

Figure 2-15 Summary sketches of flow structures: (a) Anti-symmetrical. (b) Symmetrical.

CHAPTER 3

EFFECT OF A STREAMWISE OSCILLATING CYLINDER ON A DOWNSTREAM CYLINDER WAKE

3.1 Introduction

One or more cylinders in the wake of one or more upstream cylinders in a cross flow is a situation frequently seen in engineering. Examples include heat exchangers, offshore structures, power transmission lines and high-rise buildings. When the Reynolds number, *Re*, exceeds a critical value, the boundary layer of a circular will separate from a structure in a flip-flop manner. The alternate flow separation from the structure in turn produces a fluid excitation force, which may, under the right circumstance, induce a structural oscillation at a significant magnitude. This oscillation will then influence the flow around downstream structures. From another point of view, the documentation of the possible influence on the downstream cylinder wake is important for flow-control problems, where the unsteady flow pattern around a structure needs to be altered, either cancelled, e.g., to suppress flow-induced vibration or reinforced such as for transport enhancement in heat transfer applications (Karniadakis & Triantafyllou, 1989). It is

therefore of both fundamental and practical interests to investigate how an oscillating cylinder will alter a downstream cylinder wake.

The simplest case of the multiple structures is a two-cylinder system, which may have side-by-side, in-tandem or staggered arrangements. The structural oscillation can be forced by external loadings or induced by vortex shedding. The oscillation can be in transverse or longitudinal (streamwise or in-line direction by some authors. In this thesis, unless special announced, streamwise will be incited for each Chapter.) or a combination of both. Previous studies mostly focused on the transverse oscillation of a single or two cylinders (e.g., Bearman 1984; Ongoren & Rockwell 1988a; Williamson & Roshko 1988; Staubli & Rockwell, 1989; Griffin & Hall, 1991; Hover *et al.* 1998 and Carberry *et al.* 2001). This is perhaps because the lift force (rms) on a structure is in many cases, say in an isolated cylinder case, (Chen 1987) one order of magnitude larger than the drag force (rms). Subsequently the lateral structural oscillation prevails against that in the streamwise direction. However, the drag force is also significant; it could even exceed the lift, in particular in the context of multiple flexible cylinders.

There have been a number of investigations involving a single streamwise oscillating cylinder (e.g., Bishop & Hassan, 1964; Tanida *et al.* 1973; Griffin & Ramberg, 1976; Naudascher, 1987; Ongoren & Rockwell, 1988b; Griffin & Hall, 1991; Cetiner & Rockwell, 2001), vortex-induced vibration of two flexible cylinders in tandem arrangement (King, 1976; Brika & Laneville, 1999; Laneville & Brika, 1999) and longitudinally forced oscillations of two tandem cylinders (e. g., Tanida et al. 1973; Li *et al.* 1992) in a cross flow. These previous investigations have been surveyed in the

Chapter 1. Furthermore, interactions between a streamwise oscillating cylinder and flow at relatively large *A/d* have also been studied in Chapter 2. However, how a streamwise oscillating cylinder would affect a downstream cylinder wake has not been studied. Investigation on the upstream cylinder or the downstream cylinder oscillates streamwise at a relative large oscillation amplitude has also not been reported in previous studies. Many questions may be asked: How do the wakes of two tandem cylinders, the upstream one vibrating and the downstream one stationary, interact? What is the dominant flow structure when the upstream oscillating cylinder is locked on with the vortex shedding? In this paper, the flow structure refers to the vortex pattern. Also, how would the flow structure change in the absence of locking-on phenomenon? These issues are interesting and motivate the present investigation.

The present work aims to investigate the effect of a streamwise oscillating cylinder on a downstream cylinder wake. The investigation employs a laser-induced fluorescence (LIF) technique to visualise the flow structures behind the oscillating cylinder and the downstream stationary cylinder. The qualitative flow images are examined along with the quantitative flow field as obtained using the particle image velocimetry (PIV).

3.2 Experimental Details

3.2.1 LIF visualization in a water tunnel

The LIF measurements were carried out in a water tunnel introduced in Chapter 1. Further details of the water tunnel can be found in Zhou *et al.* (2001).

Two acrylic circular tubes of an identical diameter d = 0.01 m were horizontally mounted in tandem at the mid-plane of the working section. They were cantilever-supported; the gap between the cylinder tip and the working section wall was about 0.5 mm, thus resulting in a blockage of about 6.7%. The upstream cylinder, driven by a D.C. motor through a linkage system, oscillated harmonically in time in the streamwise direction. The D. C. motor was controlled by a microcomputer so that the oscillating frequency of the cylinder could be precisely obtained. The structural oscillation amplitude was fixed at A/d = 0.5, while f_e was varied so that f_e/f_s ranged from 0 to 2. The first-mode natural frequency of the fluid-cylinder system was estimated to be about 32 Hz, one order of magnitude greater than the maximum f_e (= 2 Hz), that is, the imposed oscillation was far away from resonance.

Note that the cylinder has an aspect ratio of 15. For a stationary cylinder, an aspect ratio of 27 or larger is needed to avoid the problem of end effects (King 1977). However, an oscillating cylinder may reorganise the vortex shedding process to enhance significantly its two dimensionality. Griffin (1980) observed that, when the oscillation amplitude was greater than 0.01-0.02d, the correlation coefficient, ρ_p, between spanwise fluctuating pressures increased greatly, compared with a stationary cylinder. For example, given a threshold of ρ_p = 0.5, the spanwise correlation length was about 1d at A/d = 0.025, 6d at A/d = 0.075 and 10d at A/d = 0.125. For A/d = 0.5, the correlation length was estimated to be over 40d based on an extrapolation of his data, indicating negligible end effects in the present experiments.

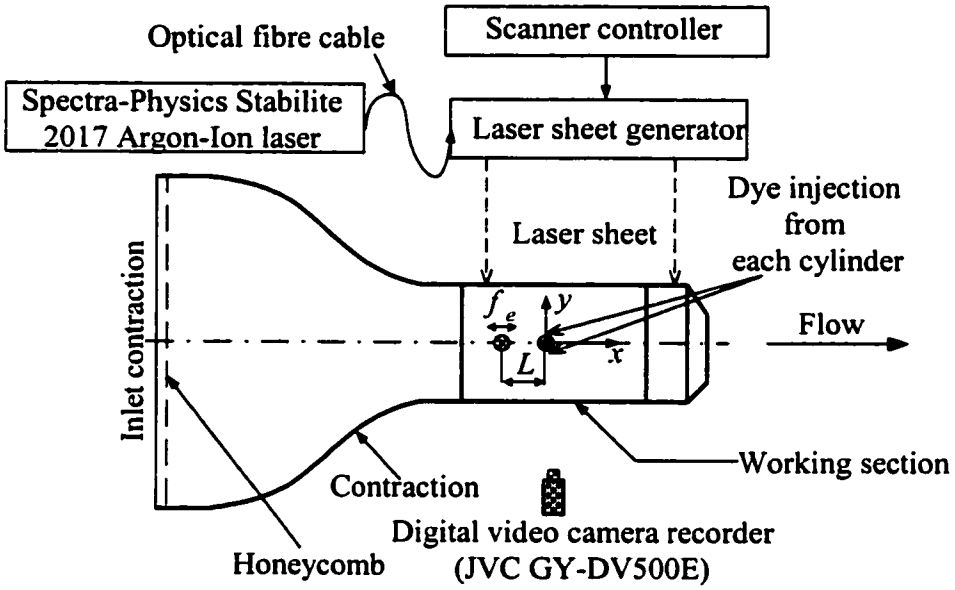

(a)

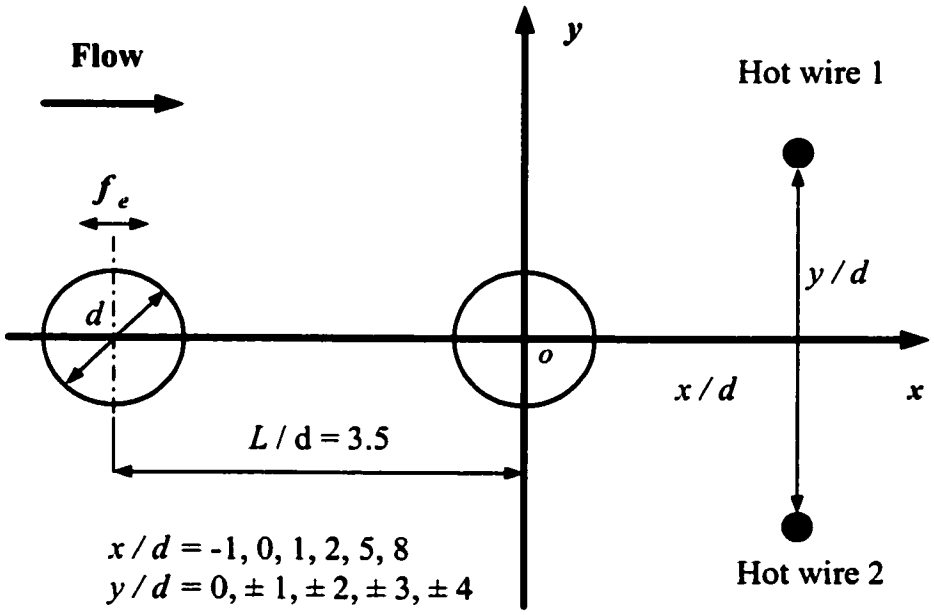

(b)

Figure 3-1 (a) Experimental set-up for flow visualization in a water tunnel. (b) Schematic arrangement of two single hot wires in a wind tunnel.

Dye (Rhodamine 6G 99%), which has a faint red colour and will become metallic green when excited by laser, was introduced through one injection pinhole located at the mid-span of the cylinder at 90°, clockwise and anti-clockwise, respectively, from the leading stagnation point. A thin laser sheet, which was generated by laser beam sweeping, provided illumination vertically over $0 \leq x/d \leq 10$ at the mid-plane of the working section. A Spectra-Physics Stabilite 2017 Argon Ion laser with a maximum power output of 4 watts was used to generate the laser beam and a professional digital video camcorder (JVC GY-DV500E), set perpendicular to the laser sheet, was used to record the dye-marked vortex streets at a framing rate of 25 frames per second.

Measurements were carried out for L/d = 2.5, 3.5 and 4.5 and Re = 150 ~ 1000, where U_∞ is the free stream velocity and ν is the kinematic viscosity.

3.2.2 Wind tunnel experiments

Wind tunnel The PIV measurement was carried out in a closed-loop wind tunnel to obtain both qualitative and quantitative data at a range of $f_e/f_s = 0 \sim 1.5$. Details of the wind tunnel can be found in Chapter 2.

Cylinder Assembly The cylinder assembly was designed similarly to that used for the LIF measurements in the water tunnel. Two aluminium alloy cylinders of an identical diameter of 0.015 m were cantilever-supported in the horizontal mid-plane of the working section. The length of both cylinders inside the tunnel was 0.35 m, thus resulting in a blockage of 1.25% and an aspect ratio of about 23. A 0.15 m long section from the free end of each cylinder was replaced by a transparent acrylic tube in order to

allow the laser sheet to shine through, thus minimizing the shadow effects in the PIV measurement. A microcomputer-controlled DC motor system was used to drive the upstream cylinder to oscillate. The oscillation amplitude varied from A/d = 0.5 to 0.67, and f_e/f_s ranged from 0 to a maximum of 1.5. The first-mode natural frequency of each cylinder was about 272 Hz, which is a factor of 11 times the maximum f_e (= 24 Hz). To minimize the reflection noise generated by the laser sheet shining on the cylinders, the surface of both cylinders were painted black except a 20 mm long section at 0.12 m from the free end on the acrylic section. In the free-stream, the longitudinal turbulence intensity was measured to be approximately 0.4%.

PIV measurements The velocity field was measured using a Dantec standard PIV2100 system for P/d = 3.5 and Re = 1150. The f_e/f_s ratio investigated ranged from 0 to 1.5. The detailed information of PIV2100 has been given in Chapter 1. Each image covered an area of 115 mm × 92 mm of the flow field, i.e., x/d = -4.3 d ~ 4.3 d and y/d = -3.1 d ~ 3.1d; the x and y coordinates and their origin are defined in Figure 3-1b. The longitudinal and lateral image magnifications were identical, i.e. 0.09 mm/pixel. Each laser pulse lasted for 0.01 μs. The interval between two successive pulses was typically 50 μs. Thus, a particle would only travel 0.05 mm (0.56 pixels or 0.003 d) at U_∞ = 1.0 m/s. An optical filter was used to allow only the green wavelength (532 nm) generated by laser to pass.

Since both cylinders were included in the PIV images, which could cause errors in deriving velocities around the cylinders, they were masked using a built-in masking function in the Dantec PIV2001 system before calculation of particle velocities. In the

image processing, 32 × 32 rectangular interrogation areas were used. Each interrogation area included 32 pixels (≈ 0.2 d) with 50% overlap with other areas in both the longitudinal and lateral directions. The ensuing in-plane velocity vector field consisted of 79 × 63 vectors, which gave the same number of spanwise vorticity component, ω_z, which may be approximately obtained based on particle velocities. The spatial resolution for vorticity estimate was about 1.43 mm or 0.095 d.

Hot-wire measurements The dominant frequencies of the two cylinder wakes were measured using two hotwires in the wind tunnel. Two single hot-wires were placed symmetrically at x/d = -1, 0, 1, 2, 5, 8 and y/d = 0, ± 1, ± 2, ± 3, ± 4, respectively (Figure 3-1*b*), to monitor simultaneously the instantaneous flow velocity behind each cylinder. Constant-temperature circuits were used for the operation of the hot wires. Experiments were carried out for L/d = 3.5 and Re = 11500. Signals from the circuits were offset, amplified and then digitized using a 16-channel (12bit) Analog/Digital board and a personal computer at a sampling frequency $f_{sampling}$ = 1.5 kHz per channel. The typical duration of each record was about 30 s.

Mean Drag and Lift measurement of the downstream cylinder The pressure distribution of the downstream cylinder was measured using a single wall-pressure tap at 0.12m from the free end of the cylinder. The tap was connected to a digital pressure transducer (Furness, least count = 0.098 mm H_2O). The cylinder was rotated at an interval of 7.5^0. The mean drag and lift were calculated by integrating the wall static pressure around the cylinder. Measurements were conducted at a range of $f_e/f_s = 0 \sim 1.5$, $L/d = 3.5$, $A/d = 0.67$ and $Re = 1150$.

3. 3 Typical Flow Structures

It has been found that the flow structure around the two cylinders largely depends on the combination of f_e/f_s and A/d for $L/d = 2.5 \sim 4.5$, bearing a similarity to the flow around an isolated oscillating cylinder (e.g., Karniadakis & Triantafyllou 1989). This could suggest the dominance of the oscillating-cylinder wake over that of the downstream cylinder. Three typical flow structures have been identified when the vortex shedding frequency is locked on with the oscillation of the upstream cylinder, each showing a completely distinct behaviour.

3. 3. 1 Symmetric-antisymmetric complex street (SA-mode)

For $f_e/f_s \geq 1.6$ and a fixed $A/d = 0.5$, the flow behind the downstream cylinder is characterized by a binary street that consists of two outer rows (toward the free stream) of symmetrically arranged vortices originated from the upstream oscillating cylinder and two inner rows (near the centerline) of antisymmetrically arranged vortices generated by the downstream stationary cylinder. The downstream cylinder sheds vortices alternately, while the upstream one sheds symmetrically, as is evident in photographs (Figure 3-2) obtained from the LIF measurement in the water tunnel ($f_e/f_s = 1.8$, $A/d = 0.5$ and $Re = 300$). Note that each structure shed from the upstream cylinder embraces a pair of counter-rotating vortices. We may refer to this structure as a binary vortex. In order to understand the formation of this pair of vortices, sequential photographs of various phases in one typical cycle of the cylinder oscillation (Figure 3-2) are examined.

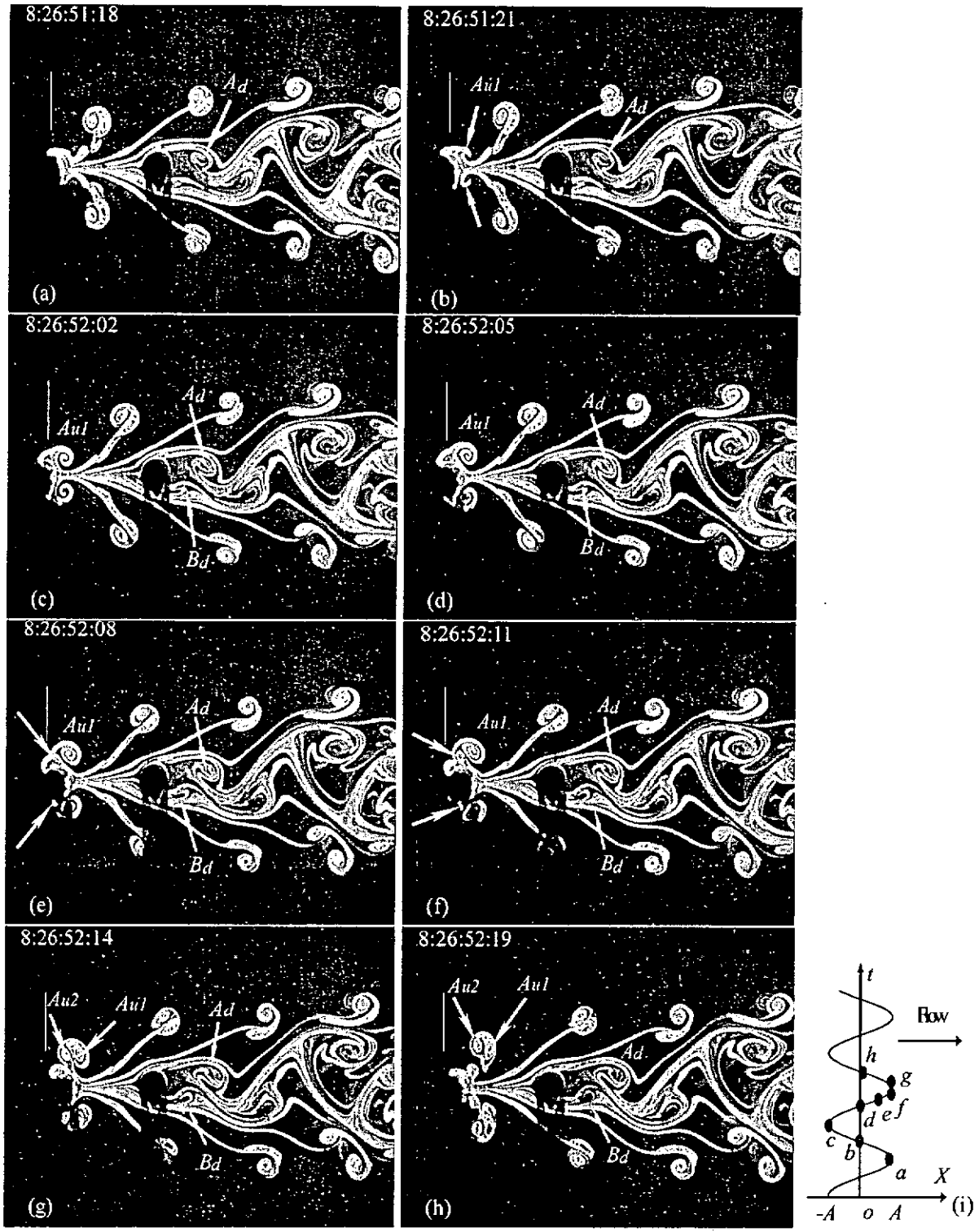

Figure 3-2 Sequential photographs of a symmetric-antisymmetric complex street at f_e/f_s = 1.8. $L/d = 3.5$, $Re = 300$, $A/d = 0.5$.

The phase of each photo is indicated in Figure 3-2i, where t and X represent time and the streamwise displacement, from the reference position ($X = 0$), of the upstream cylinder, respectively. The reference position is marked by a vertical line near the upstream cylinder. When the upstream cylinder moves oppositely to the flow direction (Figure 3-2a to 3-2c), one clockwise rotating vortex A_{u1} above the centreline forms due to the natural vortex shedding. As the cylinder moves from $-A$ to $+A$ in the same direction as the flow (Figure 3-2c to 3-2f), the fluid near the cylinder wall moves along with the cylinder under the viscosity effect, but the fluid further away now moves oppositely (right to left) relative to the cylinder. The average moving velocity of the cylinder is about 2.4 cm/s (f_e = 1.2 Hz), while that of water was 2.7 cm/s. Thus, the maximum velocity of water relative to the cylinder is estimated to be about 1.07 cm/s, resulting in an instantaneous Reynolds number (based on this relative velocity and cylinder diameter) of 120, which exceeds the critical Reynolds number ($\approx$ 40, e.g. Schlichting & Gersten 2000) for vortex shedding. Therefore, a vortex, A_{u2}, of the anti-clockwise sense begins to form. Eventually, the structure containing a pair of counter-rotating vortices A_{u1} and A_{u2} separates from the cylinder (Figure 3-2f to 3-2h) and evolves downstream. A similar flow structure was observed in the turbulent flow regime, as illustrated in Figure 3-3 (Re = 500).

The PIV measurement may provide quantitative as well as qualitative information. The maximum f_e/f_s achievable for the present experimental set-up was 1.5 in the wind tunnel. In order to obtain the symmetric and staggered binary street at this f_e/f_s, A/d was increased to 0.67.

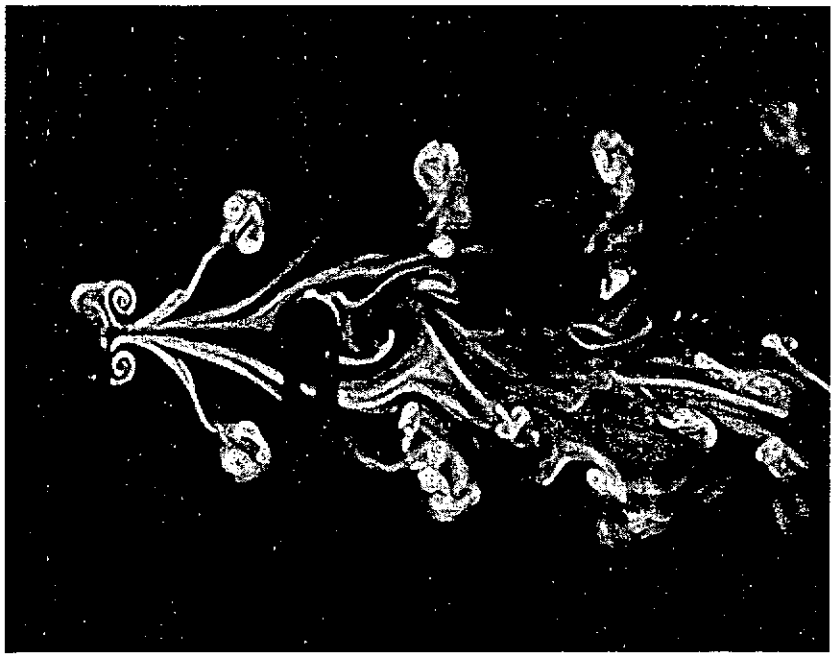

Figure 3-3 A symmetric-antisymmetric complex street at f_e/f_s = 1.8. L/d = 3.5, Re = 500, A/d = 0.5.

Figure 3-4 presents two typical plots of the contours of spanwise vorticity $\omega_z^* = \omega_z d / U_\infty$ obtained from the PIV measurement (L/d = 3.5, A/d = 0.67, Re = 1150, f_e/f_s = 1.45). Vortices generated by the downstream cylinder exhibit a spatially staggered arrangement, consistent with the LIF measurement (Figures 3-2 and 3-3). The binary vortices or counter-rotating vortex pairs near the upstream cylinder are evident in both plots and are identifiable beyond the downstream cylinder. These vortices are formed symmetrically about the flow centreline and remain so as they move downstream. The observation supports the earlier interpretation on the formation process of A_{u1} and A_{u2} based on sequential photographs (Figure 3-2). The negative vorticity concentration, corresponding to the naturally shed vortex A_{u1} in Figure 3-2, in the binary vortex above the flow

centreline shows the approximately the same maximum ω_z^* as that of the positive concentration corresponding to A_{u2}. However, the size of A_{u1} is significantly larger than that of A_{u2}. This is reasonable. When the cylinder moves oppositely to the flow to form A_{u1}, the velocity gradient in the shear layer is expected to increase, thus generating the vortex of a larger strength. The maximum magnitude of ω_z^* of the binary vortex is about 9, significantly larger than that (3.6) shed from the downstream cylinder. Two factors could be responsible. Firstly, the lock-on condition will surely enhance the binary vortex strength. Secondly, the upstream cylinder movement opposite to the flow increases the velocity gradient of the shear layer and subsequently the vorticity concentration of the binary vortices. The binary vortex is characterized by a very fast decay, its maximum magnitude of ω_z^* dropping from 7 ~ 9 near the upstream cylinder to about 3 when reaching the downstream cylinder. This is likely due to the cancellation between the positive and negative vorticity concentrations within the binary vortex.

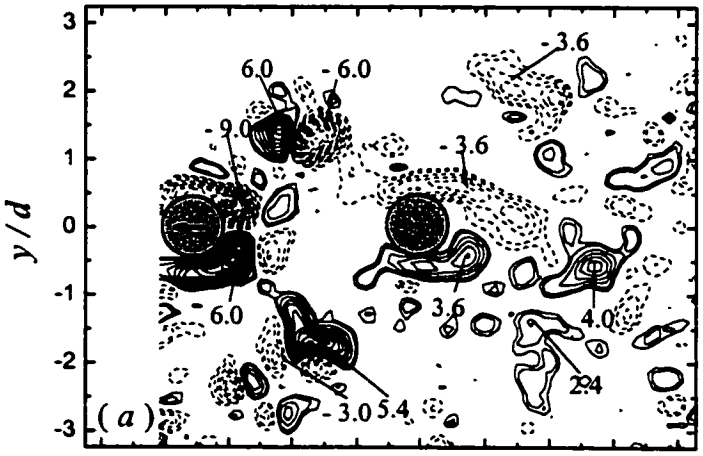

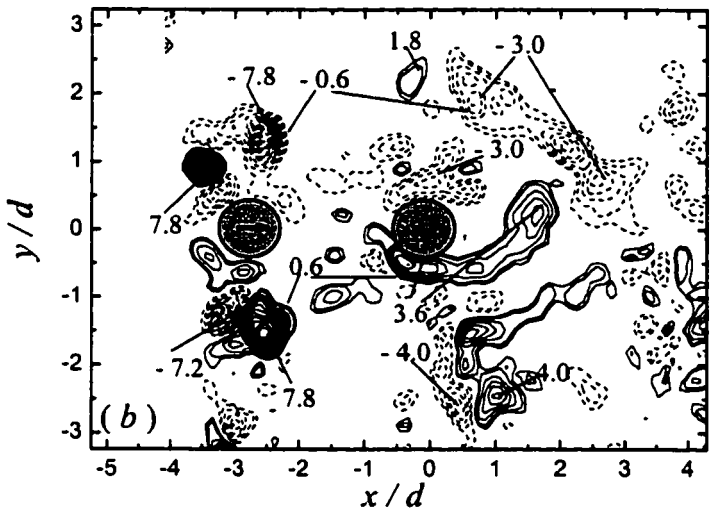

Figure 3-4 Instantaneous vorticity contours $\omega_z^* = \omega_z d / U_\infty$ obtained from the PIV measurement (the contour increment = 0.6, A/d = 0.67, Re = 1150, L/d = 3.5. f_e/f_s = 1.45).

Figure 3-5 presents the power spectral density function, E_u, of measured hot-wire signals above the centreline. The calculated E_u below the centreline is essentially the same and thus is not shown. At x/d = -1, i.e., between the two cylinders, E_u exhibits one pronounced peak at f/f_e = 1.0 (f^* = 0.29) across the wake, indicating the occurrence of lock-on between the frequency of binary vortices and that of the cylinder oscillation. The spectral phase (not shown) between the signals measured from the two hot-wires arranged symmetrically about y/d = 0 is zero at f/f_e = 1.0, reconfirming the symmetrical arrangement of binary vortices (Figures 3-2 to 3-4). At y/d > 1, another peak occurs at f/f_e

= 2 ($f^* = 0.58$) and becomes more pronounced for increasing y/d, consistent with the fact that each binary vortex includes two counter-rotating vortices (Figure 3-2).

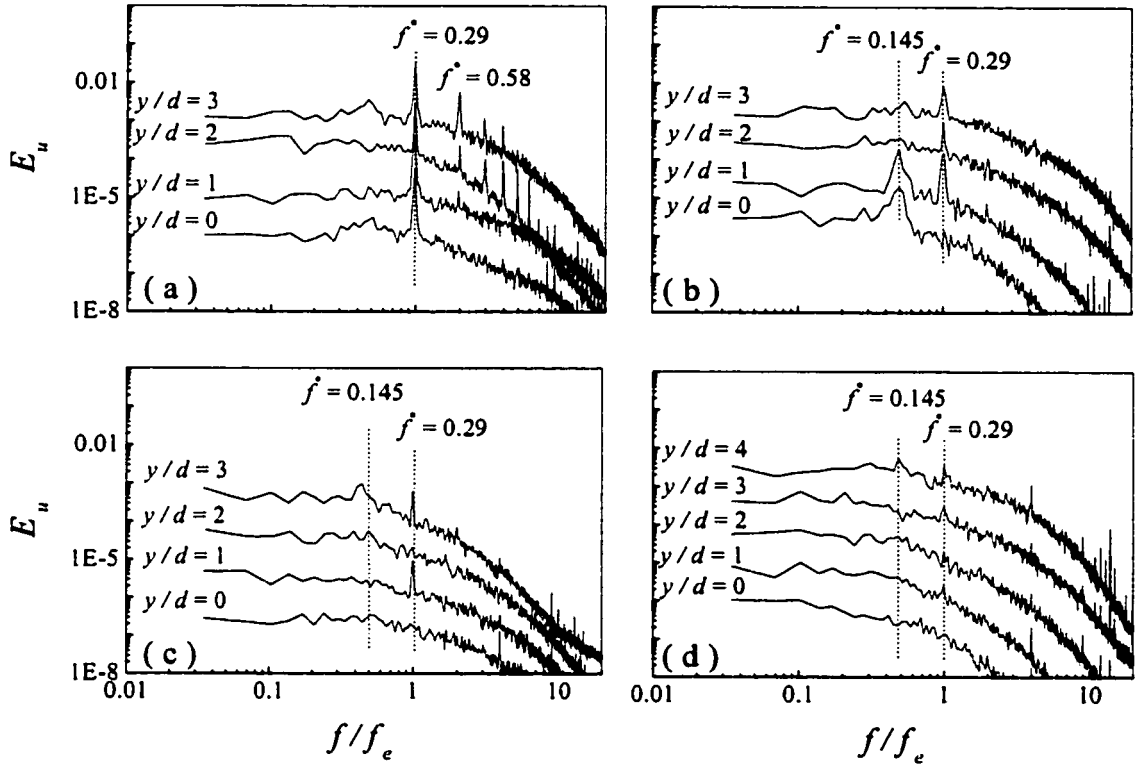

Figure 3-5 Power spectral density function of hot-wire signals at $f_e/f_s = 1.45$, $A/d = 0.67$, $L/d = 3.5$ and $Re = 1150$. (a) $x/d = -1$; (b) $x/d = 2$; (c) $x/d = 5$; (d) $x/d = 8$.

At $x/d = 2$, one rather strong peak occurs at $f/f_e = 0.5$ for $y/d \leq 1$ but not for $y/d > 1$. The frequency of vortex shedding from the downstream cylinder was estimated to be $0.5f_e$ by means of counting consecutive vortices (about 50 pairs) for a certain period on

the video record obtained in the LIF measurement. The peak at $f/f_e = 0.5$ is thus ascribed to the two inner rows of vortices. This is further corroborated by a spectral phase at $f/f_e = 0.5$ of near π (not shown) between the hot-wire signals, consistent with the anti-symmetrical arrangement of the two inner rows (Figures 3-2 and 3-3). It is then inferred that the vortex shedding frequency of the downstream stationary cylinder halves that of binary vortices.

For $y/d \geq 2$, E_u displays a peak only at $f/f_e = 1.0$ ($f^* = 0.29$), apparently consistent with the observation that the symmetrical arranged binary vortices originated from the upstream oscillating cylinder occurred fairly far away from $y/d = 0$ (Figures 3-2 and 3-3). The peak at $f/f_e = 2$ or $f^* = 0.58$ in Figure 3-5a is not identifiable at $x/d = 2$, indicating that one of the counter-rotating vortices within the binary vortex has vanished due to the vorticity cancellation. The result is internally consistent with the vorticity contours (Figure 3-4), which show for $x/d > 2$ the survival of the naturally shed vortices only. At $x/d = 5$, the peak at $f/f_e = 0.5$ disappears completely (Figure 3-5c), signalling the absence of the alternating inner vortex street generated by the downstream stationary cylinder. By $x/d = 8$, all peaks are barely identifiable in E_u. The fast decay of both inner and outer streets is probably attributed to the strong interaction between the two streets.

It is worthwhile comparing the above spectral result with that (Figure 3-6) when the upstream cylinder does not oscillate, i.e., $f_e/f_s = 0$. E_u displays one peak at $f/f_e = 0.127$ behind both upstream and downstream cylinders.

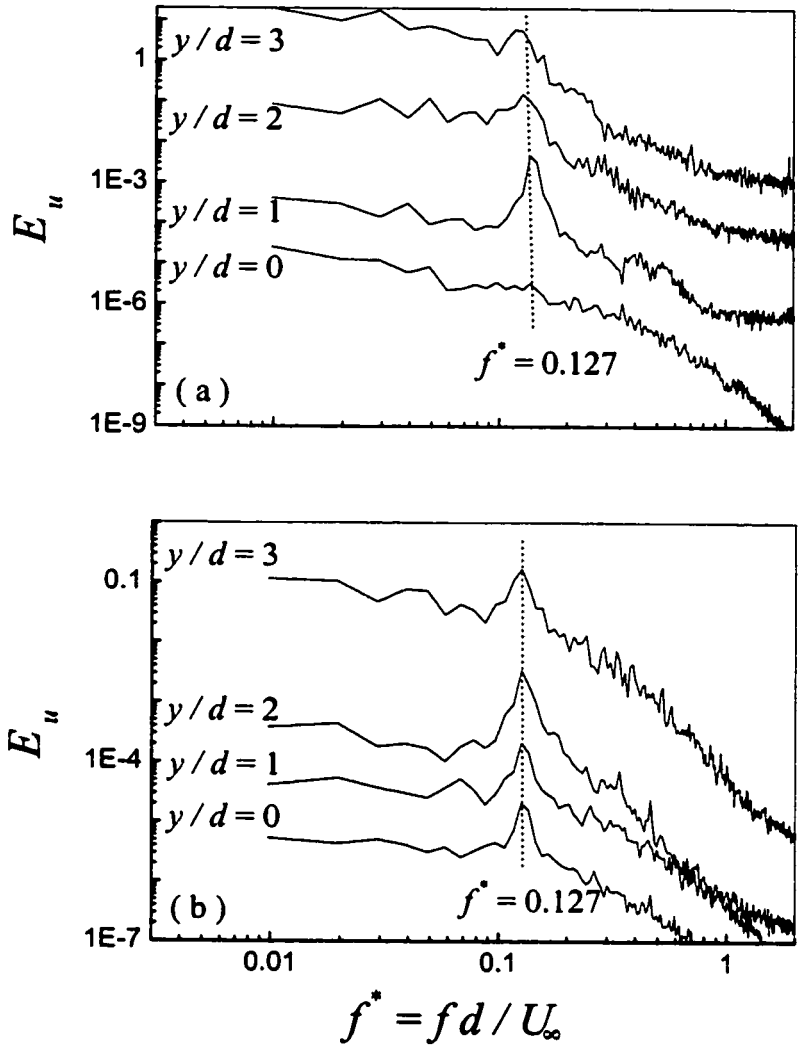

Figure 3-6 Power spectral density function of hot-wire signals: (a) x/d = -1, (b) 2. L/d = 3.5, $f_e/f_s = 0$ and $Re = 1150$.

Evidently, the cylinder oscillation has altered the frequency of vortex shedding from f/f_e = 0.127 to 0.29 for the upstream cylinder and to 0.145 for the downstream cylinder. It is not accidental that the vortex shedding frequency of the downstream

cylinder halves that of the upstream cylinder. This is required by the stability of the binary street, which consists of two inner anti-symmetrically arranged rows and two symmetrically arranged rows, behind the downstream cylinder. On the other hand, the two shedding frequencies should be identical if the two outer rows are also anti-symmetrically arranged, as observed in the following section.

3.2 Antisymmetric-antisymmetric complex street (AA-mode)

As f_e/f_s reduces to 1.0 ~ 1.6 at $A/d = 0.5$, the flow structure experiences a dramatic change into a more complicated structure, as illustrated in Figure 3-7 for $f_e/f_s = 1.08$. A careful examination reveals that the flow behind the downstream stationary cylinder consists of two outer rows of binary vortices such as A_u and B_u, originated from the upstream cylinder, and two inner rows of single vortices, denoted by A_d and B_d, generated by the downstream cylinder. Alternate vortex shedding occurs for both cylinders. However, the two successive vortices alternately shed from the upstream cylinder quickly move to one side of the wake before reaching the downstream cylinder. For example, A_{u2} was shed from the upper side of the upstream cylinder but crossed the centreline to approach A_{u1} shed from the lower side of the same cylinder (Figure 3-7a). The two vortices eventually paired to form a binary vortex in the lower outer row of the binary street behind the downstream cylinder (Figure 3-7b to 3-7d). But A_{u2} appears losing its identity quickly probably because of vorticity cancellation with A_{u1}; a single vortex A_u emerges (Figure 3-7e to 3-7h). The evolution of vortices B_{u1} and B_{u2}, which were shed from the upper and lower side of the upstream cylinders, respectively, is quite similar to

that of A_{u1} and A_{u2}, though they end up with a binary vortex and a single vortex in the upper outer row of the binary street.

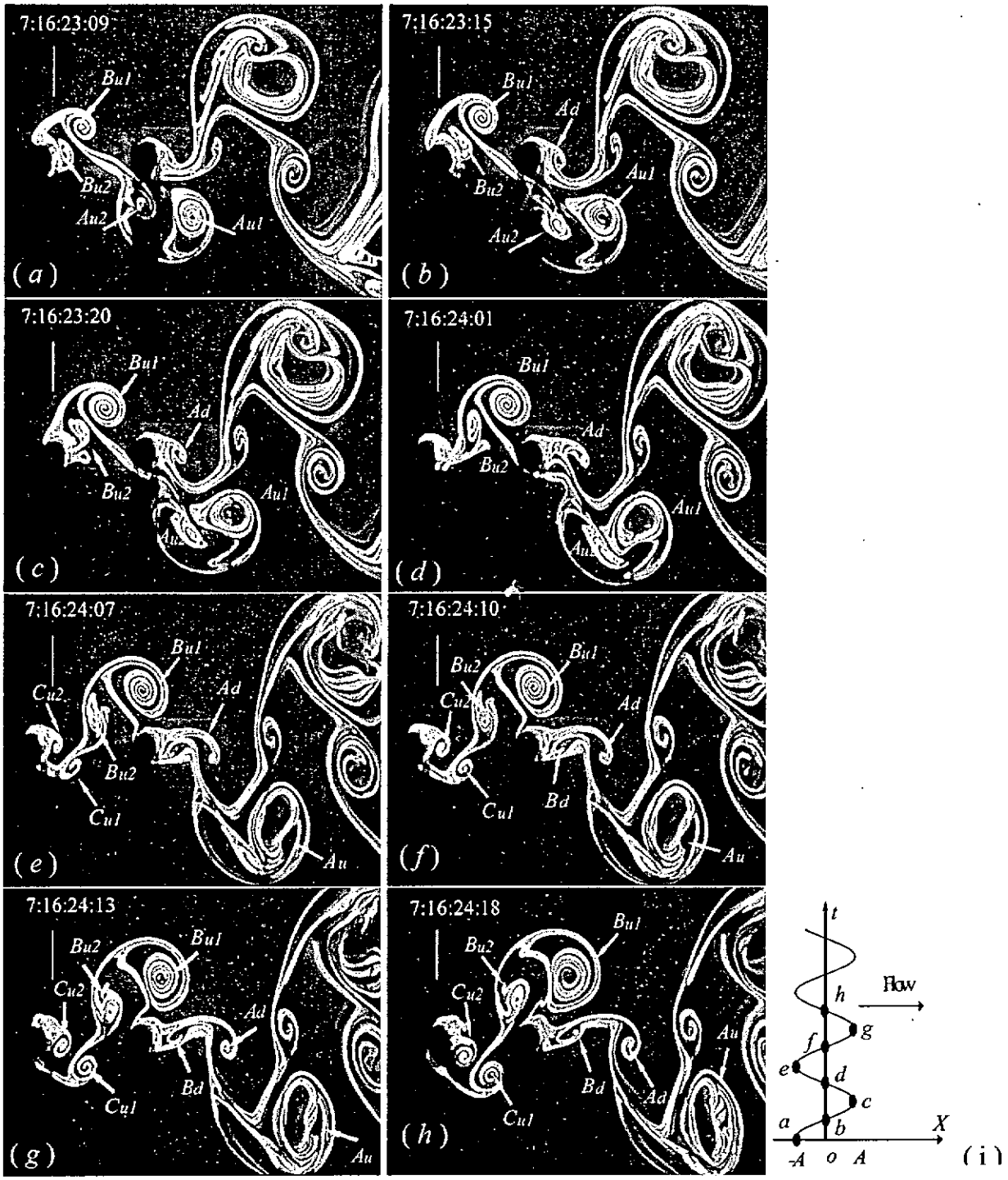

Figure 3-7 Sequential photographs of an antisymmetric-antisymmetric complex street at $f_e/f_s = 1.08$. $L/d = 3.5$, $Re = 300$, $A/d = 0.5$.

The upstream cylinder movement plays a key role to induce a vortex across the centreline merging with the vortex on the other side of the wake. Noting the vortex shedding frequency f_{su} of the upstream cylinder is locked on to f_e. Each time when the cylinder moves oppositely, right to left, to the flow direction, one vortex begins to form and separate from the cylinder. This process is exemplified in Figure 3-7(d) to 3-7(f), where the vortex C_{u1} is in its initial stage of formation. The cylinder movement opposite to the flow is likely to reduce the backpressure of the cylinder. The very low pressure in the base region draws in C_{u1} to cross the centreline. The ensuing cylinder movement in the flow direction (Figure 3-7g to 3-7h) may act to push C_{u1} further down.

The flow structure observed in the LIF photographs is identifiable in the ω_z^* contours obtained from the PIV measurement (Figure 3-8). The vortex, shed from the upstream cylinder, crossing the centreline appears weak and quickly becomes difficult to identify, probably because of vorticity cancellation with the one, apparently of a larger strength, shed from the other side of the upstream cylinder. Furthermore, in similarity to the symmetric and staggered binary street (Section 3.1), vortices generated by the upstream oscillating cylinder display a larger strength than those shed from the downstream cylinder; the maximum magnitude of ω_z^* is 9.6 for the former but only 6 for the latter (Figure 3-8b). This is true even at the same x/d behind the downstream cylinder. For example, at $x/d \approx 3$ to 4, vortices from the upstream cylinder retain a vorticity strength of about 3, but those from the downstream cylinder do not exceed 2.4 (Figure 3-8a and 3-8b). The observations are internally consistent with the qualitative results from the LIF photographs.

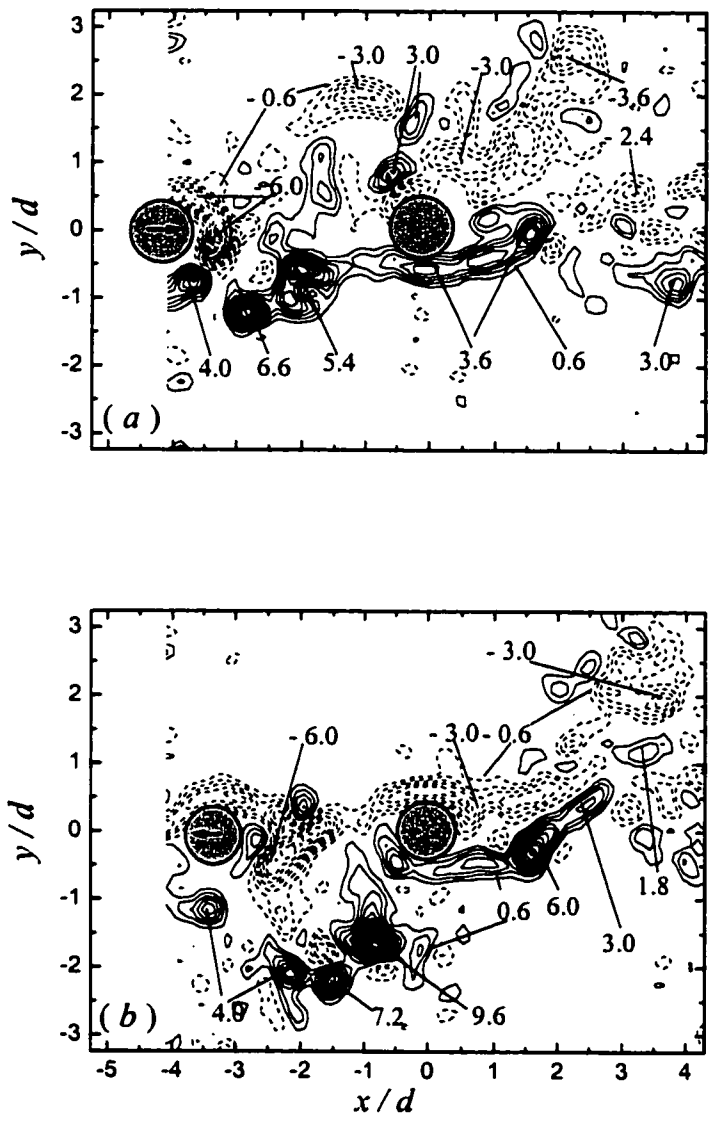

Figure 3-8 Instantaneous vorticity contours $\omega^* = \omega d/U_\infty$ obtained from the PIV measurement (the contour increment = 0.6, $A/d = 0.67$, $Re = 1150$, $L/d = 3.5$. $f_e/f_s = 0.8$).

The u-spectrum, E_u (Figure 3-9a), at f_e/f_s = 0.8 between the cylinders (x/d = -1) displays a peak at f/f_e = 1 because of the occurrence of lock-on between vortex shedding and the upstream cylinder oscillation. The peak impairs as y/d increases. Another peak occurs at f/f_e = 0.5 for $y/d \geq 1$, which is significantly more pronounced. This is probably because every other vortex (e.g., A_{u2} or B_{u2} in Figure 3-7) shed from one side of the oscillating cylinder will cross the centreline to coalesce with the cross-stream vortex and the vortex (e.g., A_{u1} or B_{u1} in Figure 3-7) that stays in its side displays a significantly larger strength (Figure 3-8).

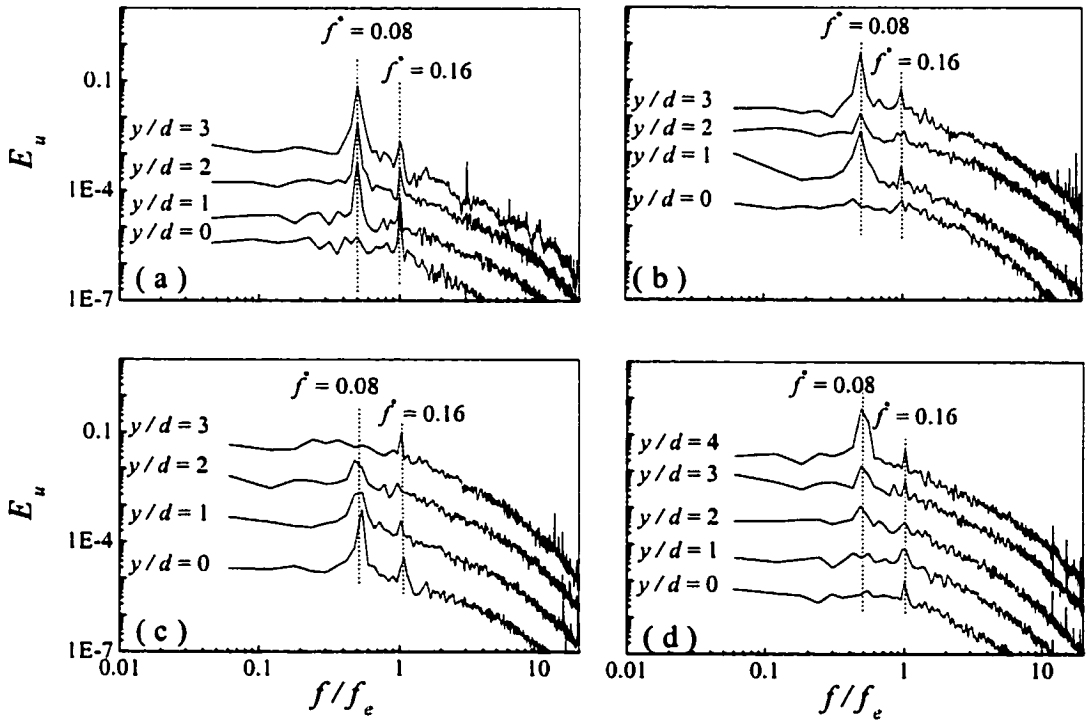

Figure 3-9 Power spectral density function of hot-wire signals at f_e/f_s = 0.8, A/d = 0.67, L/d = 3.5 and Re = 1150. (a) x/d = -1; (b) x/d = 2 ; (c) x/d = 5 ; (d) x/d = 8.

At $x/d = 2$, the peak at $f/f_e = 0.5$ in E_u remains pronounced. The one at $f/f_e = 1$ is also evident, though less pronounced. However, the latter, particularly at a small y/d, is likely attributed to vortex shedding from the upstream cylinder (c.f., Figure 3-7). The assertion is supported by earlier observation that vortices shed from the downstream cylinder display a weak strength in ω_z^* (Figure 3-8), compared with that originating from the upstream cylinder. Both peaks are further identifiable at $x/d = 5$ and 8. But the peak at $f/f_e = 0.5$ appears to be dominant throughout.

3.3 Antisymmetric single street (A-mode)

The flow is characterised by a single staggered street for $0.5 < f_e/f_s \lesssim 1.0$ at $A/d = 0.5$. Figure 3-10 presents representative sequential photographs at $f_e/f_s = 0.5$, $L/d = 3.5$, $A/d = 0.5$ and $Re = 150$ obtained from the LIF measurement. Under the influence of the downstream stationary cylinder, vortices A_u and B_u are separated alternately from the upper and lower sides, respectively, of the upstream cylinder. These vortices appear joining the shear layers around and separate from the downstream cylinder, forming a staggered vortex street downstream. Apparently, the vortex shedding frequency of the downstream cylinder must be identical to that of the upstream cylinder, that is, also locked-on to the upstream cylinder oscillation. This is confirmed by the power spectral density function of the hot-wire signals (Figure 3-12), which exhibits a single peak at $f/f_e = 1$ for $x/d > 0$ as well as $x/d < 0$.

The ω_z^* contours (Figure 3-11) obtained from the PIV measurement display a flow structure is consistent with that observed in the LIF measurement. Vortices

generated by the upstream cylinder are associated with a maximum level of about 4.2, less than one half of that (9.6) at $f_e/f_s = 0.8$ (Figure 3-8) or that (9) at $f_e/f_s = 1.45$ (Figure 3-4).

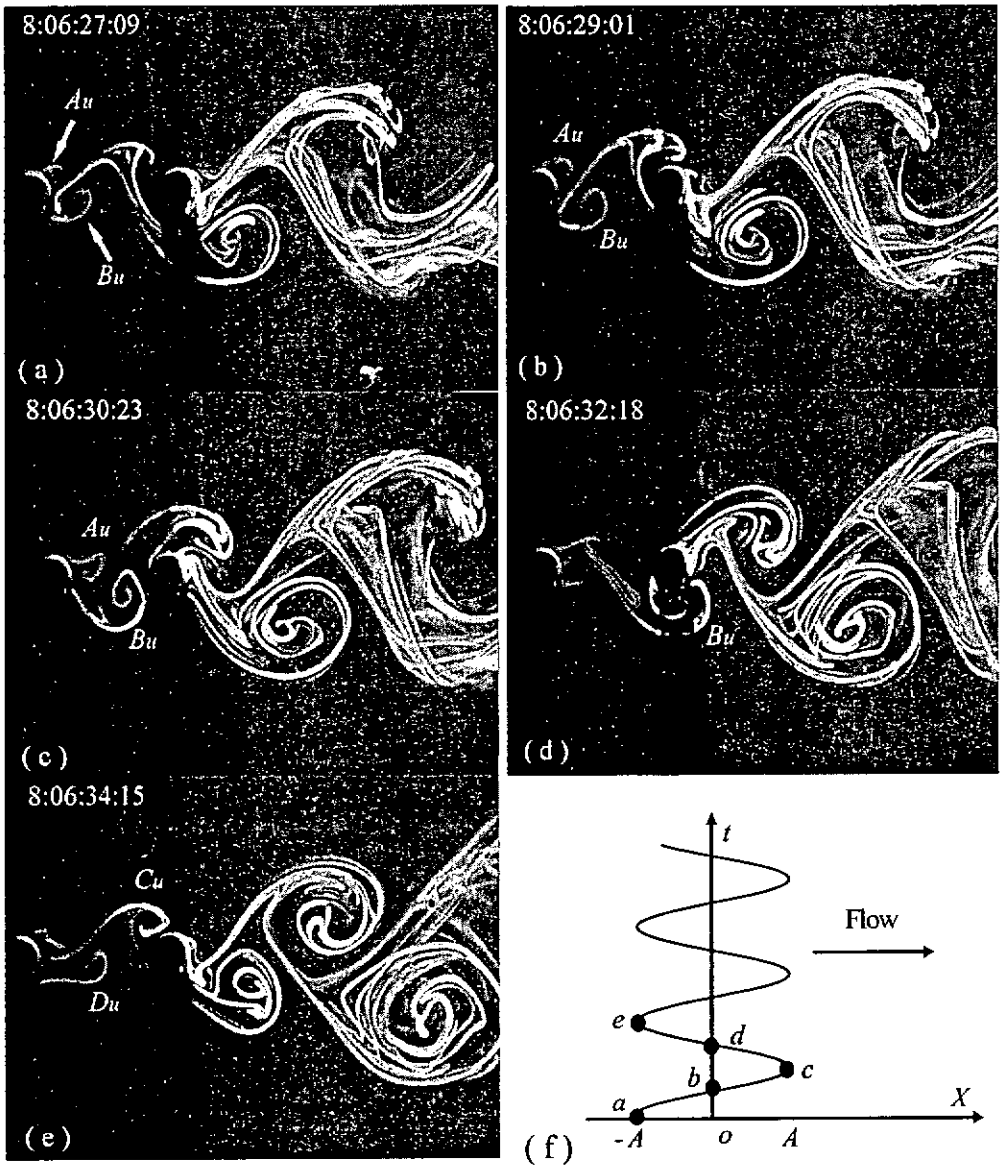

Figure 3-10 Photographs of an antisymmetric single street at $f_e/f_s = 0.5$. $L/d = 3.5$, $Re = 150$, $A/d = 0.5$.

On the other hand, the maximum vorticity level associated with vortices shed from the downstream cylinder is about 3.6, only about 10% weaker than that originating from the upstream cylinder. In contrast, the PIV data recorded 38% and 60% decreases in the maximum vorticity level for f_e/f_s = 0.8 and 1.45, respectively. The difference is largely attributed to the varying strength of vortices from the upstream cylinder at different f_e/f_s since the maximum vorticity level associated with the vortices shed from the downstream cylinder is about 3.6 in all three cases. It may be concluded that, at a fixed A/d, a higher oscillation frequency enhances the strength of vortices shed from the cylinder.

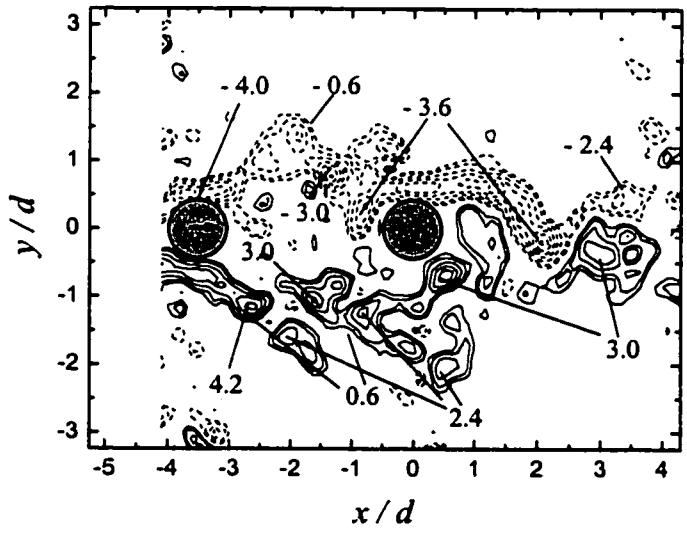

Figure 3-11 Instantaneous vorticity contours $\omega^* = \omega d/U_\infty$ obtained from the PIV measurement (the contour increment = 0.6, A/d = 0.67, Re = 1150, L/d = 3.5. f_e/f_s = 0.45).

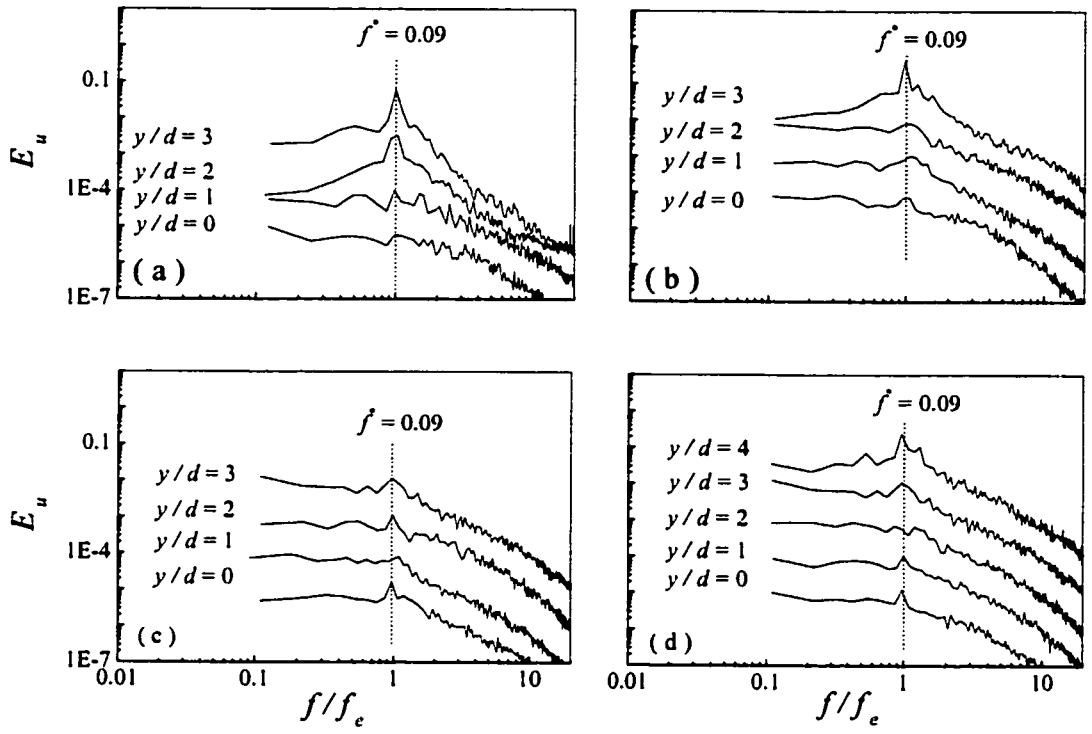

Figure 3-12 Power spectral density function of hot-wire signals at $f_e/f_s = 0.45$, $A/d = 0.67$, $L/d = 3.5$ and $Re = 1150$. (a) $x/d = -1$; (b) $x/d = 2$; (c) $x/d = 5$; (d) $x/d = 8$.

3.4 Loading on the downstream cylinder

The dependence of the typical flow structure on f_e/f_s implies a different loading on the downstream cylinder. Figure 3-13 presents the polar plots of pressure coefficient, $C_p = 2\Delta p/(\rho U_\infty^2)$, around the downstream cylinder at $Re = 1150$, $L/d = 3.5$ and $A/d = 0.67$, where Δp is the average pressure difference between the cylinder wall and an upstream reference point at which the pressure represents the static pressure of the free stream. The experimental uncertainty of the pressure measurement is estimated to be about 0.12 mm

H_2O. The pressure distribution for $f_e/f_s = 0$ (the stationary upstream cylinder) at the same L/d and Re is included in the Figure 3-13 as well as $f_e/f_s \neq 0$ in order to provide the baseline for comparison. The resultant force R is evaluated from $\sqrt{F_D^2 + F_L^2}$, where F_D and F_L are the mean pressure drag and lift pressure forces (the mean drag and lift must consider the contribution of shear stress), respectively, which are calculated by integrating the average pressures around the downstream cylinder. The direction of R is determined by the angle $\theta_R = \tan^{-1}(F_L/F_D)$. The respective force coefficients are defined by $C_L = 2F_L/(\rho U_\infty^2 d)$ and $C_D = 2F_D/(\rho U_\infty^2 d)$.

When the upstream cylinder is stationary, the pressure (Figure 3-13a) is negative everywhere on the downstream cylinder; the pressure coefficient, C_p, at the forward stagnation point is – 0.6, appreciably smaller than its base-pressure at the backward stagnation point, C_{pb} = -0.52. The observation is qualitatively agreeable with Igarashi's measurement (1981) at L/d = 3.5 & Re = 35000 and the Arie *et al.* results at L/d =4.0 and Re = 157000. The pressure distribution is also consistent with the flow structure shown in the photograph (Figure 3-15) from the LIF measurement and the vorticity contours (Figure 3-16) from the PIV measurement. For the present experimental conditions, the shear layers separating from the upstream cylinder reattach, before rolling up to form vortices, the downstream cylinder, thus enclosing 'backwater' between the cylinders. This could imply the forward stagnation pressures of the downstream cylinder comparable to the negative base-pressure of the upstream cylinder. The flow structure or

pressure distribution naturally corresponds to a very small C_D, about 0.1, and virtually zero C_L (Figure 3-14).

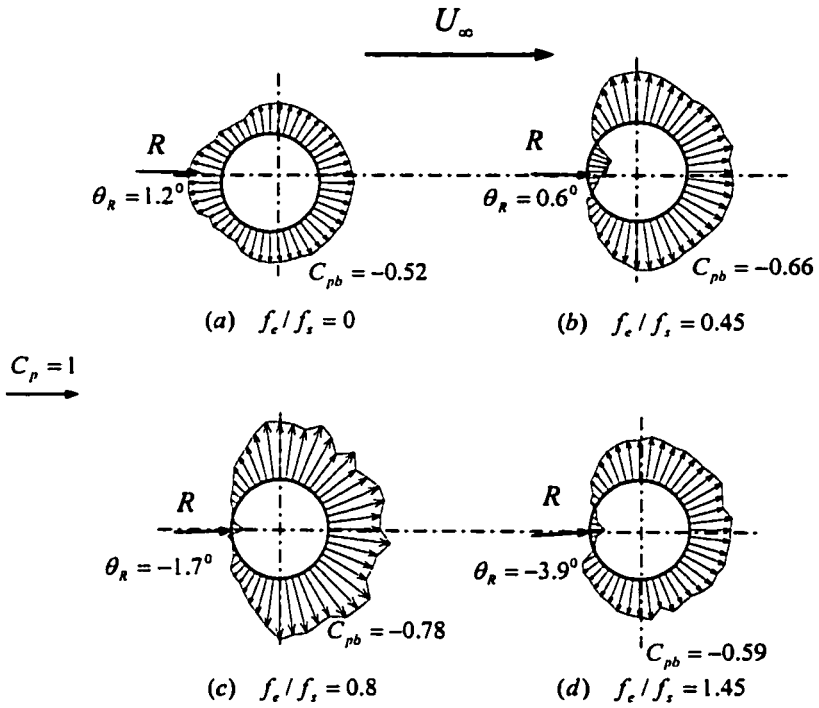

Figure 3-13 Polar plot of the circumferential distribution of average pressure coefficient at different frequency ratio for the downstream cylinder. L/d = 3.5, A/d = 0.67 and Re = 1150.

When the upstream cylinder oscillates streamwise at f_e/f_s = 0.45, vortices are shed from both cylinders. Those from the upstream cylinder could impinge on the downstream cylinder, as suggested by the LIF (Figure 3-10) and PIV data (Figure 3-11), thus resulting in positive pressure around the forward stagnation point of the downstream cylinder. Consequently, C_D increases greatly, reaching 0.63 in spite of a smaller C_{pb} (-0.66). As

f_e/f_s increases further to 0.8, one vortex shed from the upstream cylinder moves away from the centreline, while the other crosses the centreline to coalesce with the cross-stream vortex (Figures 3-7 and 3-8). Neither of them appears to be impinging on the downstream cylinder. Therefore, the positive pressure region around the forward stagnation point of the downstream cylinder shrinks. Nevertheless, there is a considerable increase in C_{pb} (-0.78) of the downstream cylinder. The combined effect leads to a slight increase in C_D (0.68).

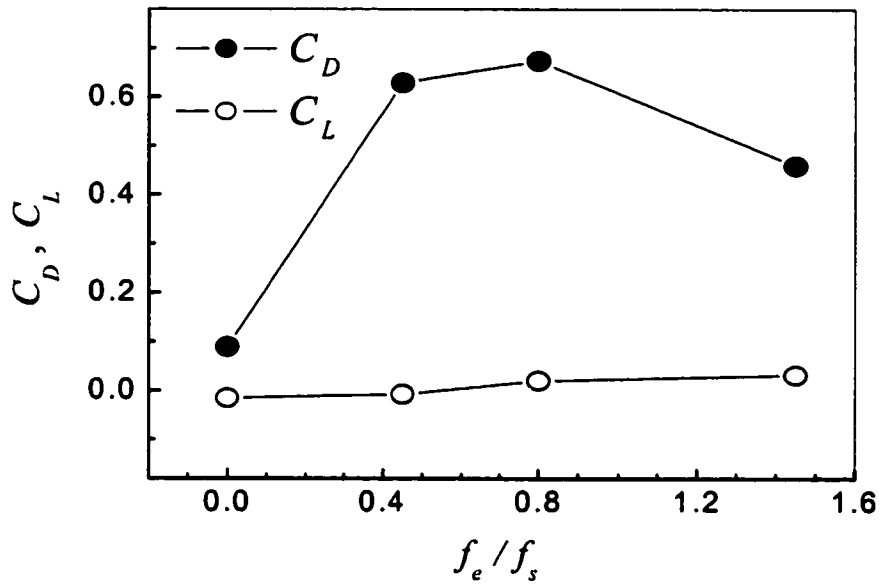

Figure 3-14 Effect of f_e/f_s on the mean drag and lift coefficients of the downstream cylinder. $L/d = 3.5$, $A/d = 0.67$ and $Re = 1150$.

At f_e/f_s =1.45, the upstream cylinder generates vortices symmetrical about the centreline. These vortices move toward the free-stream while advected downstream. The positive pressure region around the forward stagnation point of the downstream cylinder

grows slightly, compared with f_e/f_s = 0.8. But C_{pb} increases appreciably, about -0.59. Therefore, C_D reduces to 0.46.

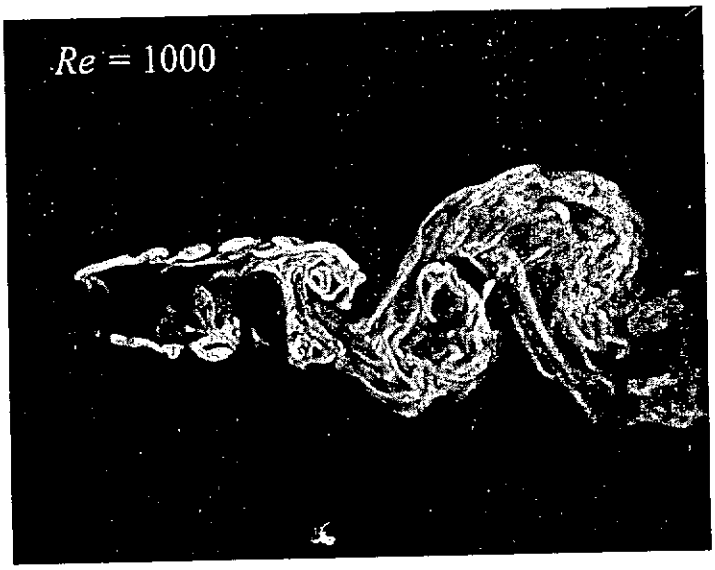

Figure 3-15 The wake of two stationary cylinders in tandem arrangement. L/d = 3.5.

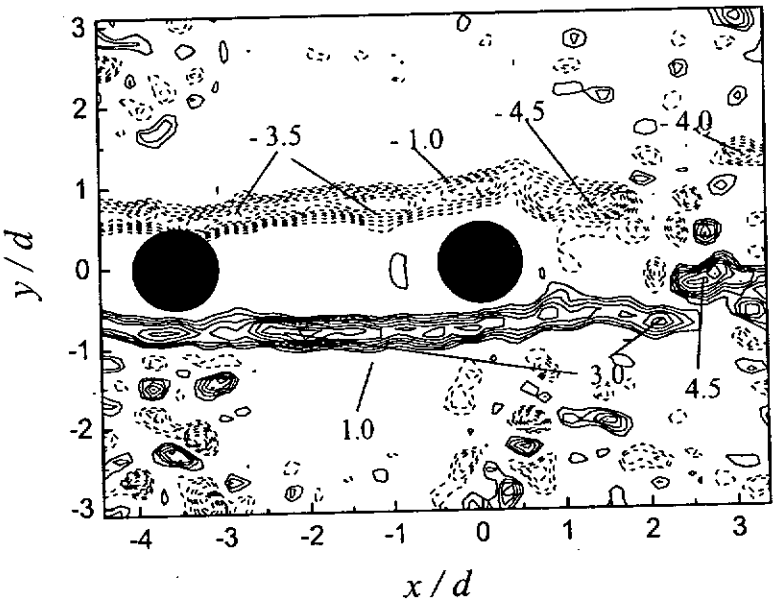

Figure 3-16 Instantaneous vorticity contours $\omega^* = \omega d/U_\infty$ obtained from the PIV.

In the wake of the downstream cylinder, the symmetrically arranged vortices originating from the upstream cylinder tend to have a strength larger than those shed alternately from the downstream cylinder. This could imply a very small fluctuating lift on the downstream cylinder. Note that the mean lift coefficient is almost close to zero in all cases.

3.5 Effect of *L/d* and *Re* on the Flow Structures

The typical flow structures (Figure 3-17) at $A/d = 0.5$ and $f_e/f_s = 1.8$ are qualitatively the same, showing the SA-mode structure, irrespective of the value of L/d (= 2.5 ~ 4.5). Similarly, the AA- and A-mode structures have been observed as f_e/f_s reduced to 0.5, which remain the same as L/d varied from 2.5 to 4.5. In contrast, the flow behind two stationary circular cylinders in the tandem arrangement depends on L/d, which is classified into three flow regimes (Igarashi 1981; Zdravkovich 1987).

For L/d in the range of 1 to 1.2 ~ 1.8, the free shear layers separated from the upstream cylinder do not reattach on the downstream cylinder. The vortex street behind the latter originates from the shear layers detached from the former. For $1.2 \sim 1.8 < L/d < 3.4 \sim 3.8$, the shear layers, separated from the upstream cylinder, reattach on the upstream side of the downstream cylinder. A vortex street is formed only behind the downstream cylinder. For $L/d > 3.4 \sim 3.8$, the separated shear layers roll up alternately and form vortices between the two cylinders. Both cylinders generate vortices. It may be inferred

that, as the upstream cylinder oscillates at reasonably large amplitude, the oscillation plays a dominant role in the formation of the flow structure behind the cylinders.

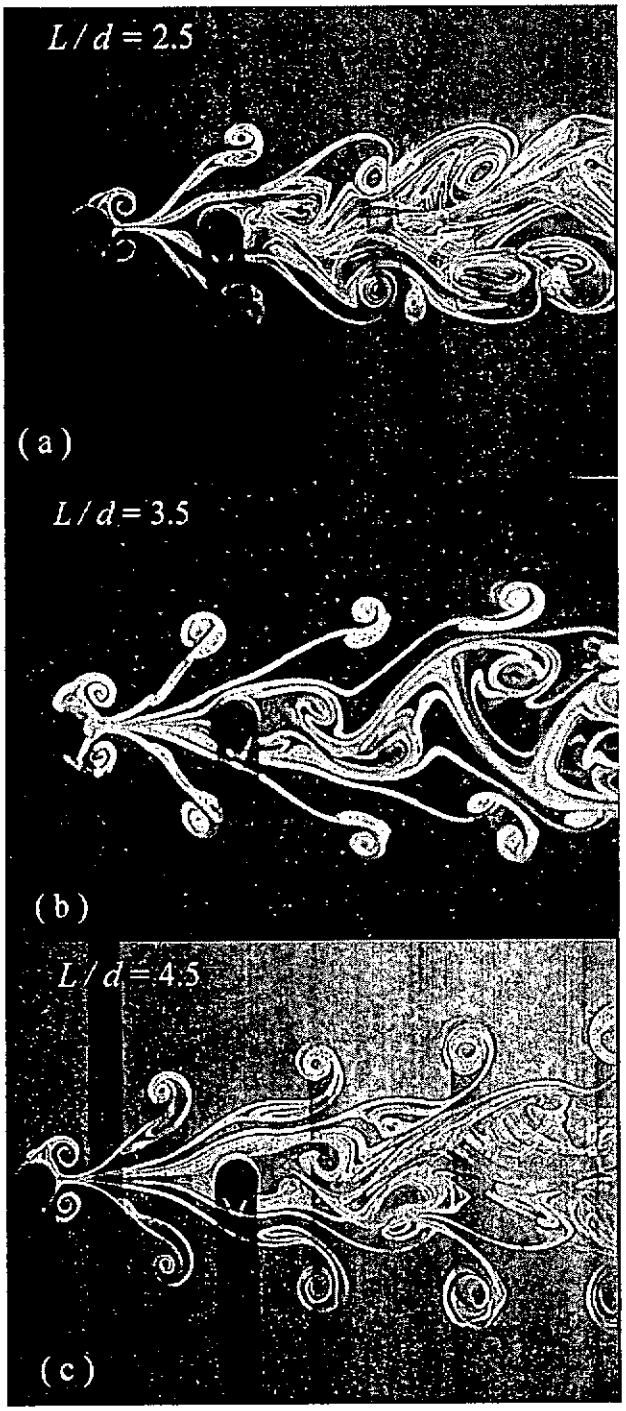

Figure 3-17 Flow structure at various L/d. $Re = 300$ and $f_e/f_s = 1.8$.

As the upstream cylinder oscillates, *Re* does not seem to affect the typical flow structure to any significant extent. As illustrated in Figure 3-18, the same mode of the flow structure is observed as *Re* increases from 300 to 800. It has been established that, for two stationary inline cylinders, the critical *L/d*, at which the flow structure changes from one flow regime to another, depends on *Re* (e.g., Ljungkrona *et al.* 1991), which is further connected to the *Re* dependence of the vortex formation length of single cylinders (e.g., Gerrard 1978).

In the oscillating upstream cylinder case, however, our measurements (not shown) at a fixed *A/d* (= 0.5) indicated a negligible *Re* effect on the critical f_e/f_s, where the flow structure changes from one mode to another. It is likely that, in the present case of the oscillating upstream cylinder, it is the cylinder oscillation that controls the near-wake fluid dynamics, and *Re* may have little effect on the vortex formation length, which is also consistent with the observation that the flow structure is independent of *L/d*.

There have been a number of investigations involving a streamwise oscillating cylinder in a cross-flow (e.g., Tanida *et al.* 1973; Griffin & Ramberg 1976; Ongoren & Rockwell 1988b). Ongoren & Rockwell categorized the typical flow structures behind a streamwise oscillating cylinder as four modes, i.e., one symmetrical, S mode, and three asymmetrical modes: A-I, A-III and A-IV. A comparison between the present observations and those discussed in Ongoren & Rockwell (1988b) indicates that the flow structure behind the upstream cylinder in the present A-mode ($0.45 \sim 0.5 < f_e/f_s < 0.8 \sim 1.0$) is the same as A-I mode ($f_e/f_s = 1.0 \sim 1.5$), and that in the AA-mode ($0.8 \sim 1.0 < f_e/f_s < (f_e/f_s)_c$ is as same as A-IV ($f_e/f_s = 1.8 \sim 2.2$) mode.

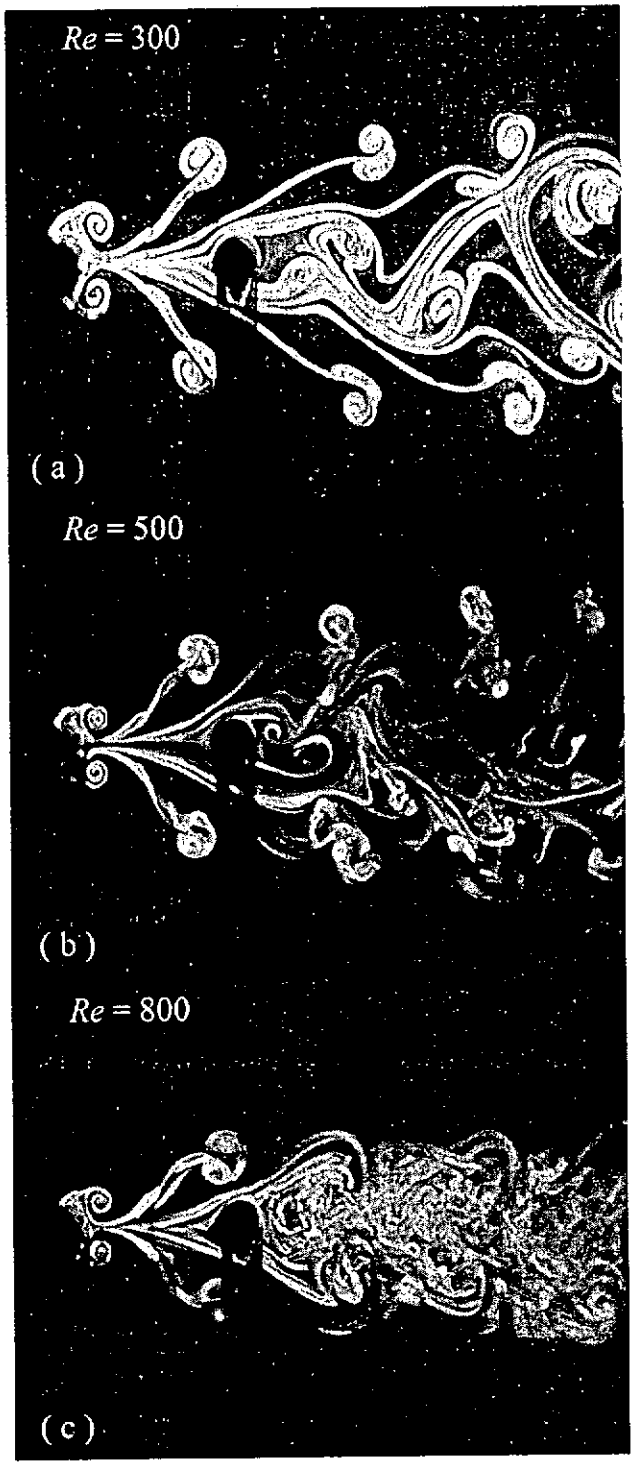

Figure 3-18 Flow structure at various *Re*. $L/d = 3.5$ and $f_e/f_s = 1.8$.

However, the S and A-III modes could not be observed in the present measurement, should due to the effect of the downstream cylinder. On a similar note, the flow structure

behind the upstream cylinder in the SA-mode however cannot be identified with any flow structure discussed by Ongoren & Rockwell (1988b). This point will be addressed in the following section.

3. 6 Dependence of the Flow Structure on A/d and f_e/f_s

Figure 3-19 presents the dependence of the flow structure on A/d and f_e/f_s based on present measurements. The dashed line is indicative of separation between the A- and AA-mode structures, while the dotted line indicates separation between the lock-on and non lock-on states. Since this work is focused on the lock-on state, the data of the non lock-on state is not presented. It is evident that the flow structure depends on the combination of A/d and f_e/f_s. The observation is quite similar to that in the case of an isolated streamwise oscillating cylinder (Karniadakis & Triantafyllou 1989). At A/d = 0.5, the A-, AA- and SA-modes occur at $f_e/f_s \approx$ 0.5 to 1.0, 1.1 to 1.6 and greater than 1.6, respectively. At A/d = 0.67, the corresponding f_e/f_s range changes to 0.45 to 0.8 for the A-mode, 0.8 to 1.45 for the AA-mode and 1.45 and above for the SA-mode. In general, as A/d increases, the critical f_e/f_s, at which the flow structure changes from one mode to another, reduces.

In the SA-mode, the flow behind the upstream cylinder consists of a remarkably symmetric binary vortex street. To our knowledge, this flow structure has never been reported in previous flow measurements behind an isolated streamwise oscillating cylinder. Therefore, an analysis is presently developed to predict the occurrence of this flow structure.

The formation of binary vortices, each consisting of a pair of counter-rotating vortices, from the upstream cylinder is apparently linked to the cylinder oscillation, and has little, at least for the L/d range presently investigated, to do with the presence of the downstream cylinder. Therefore, the same analytical approach addressed in Chapter 2 can be used here. We can give the threshold frequency ratio $(f_e/f_s)_c$ for the occurrence of the SA-mode flow structure as

$$f_e / f_s \geq \frac{(1+\frac{\mathrm{Re}_c}{\mathrm{Re}})}{2\pi St(\mathrm{Re})}\left(\frac{A}{d}\right)^{-1} = (f_e/f_s)_c, \tag{3-1}$$

The relationship $St = St(Re)$ is well documented in the literature (e.g., Chen 1987, Blevins 1994). Based on Eq. (3-1), $(f_e/f_s)_c$ is inversely proportional to A/d, in qualitative agreement with the observation from the experimental data (Figure 3-19). In the limiting cases, if $A = 0$ (two stationary cylinders), $f_e/f_s = \infty$, that is, it is impossible to generate the binary vortex.

When Re is large, say > 250, $St\ (Re) \approx 0.2$, $Re_c/Re \approx 0$ ($Re_c = 5$), the Re effect on the generation of the binary vortex should be negligible. Equation (3-1) can be then simplified as

$$f_e / f_s \geq (f_e / f_s)_c \approx \frac{5}{2\pi}\left(\frac{A}{d}\right)^{-1}. \tag{3-2}$$

The relationship of Eq. (2), given by the solid curve in Figure 3-19, may be used to predict the occurrence of the SA-mode, which falls in the region above the curve. The prediction agrees well with the available experimental data. Other than Re, the occurrence

of the SA-mode flow structure may depend on initial conditions such as turbulence level, roughness of cylinder and so on.

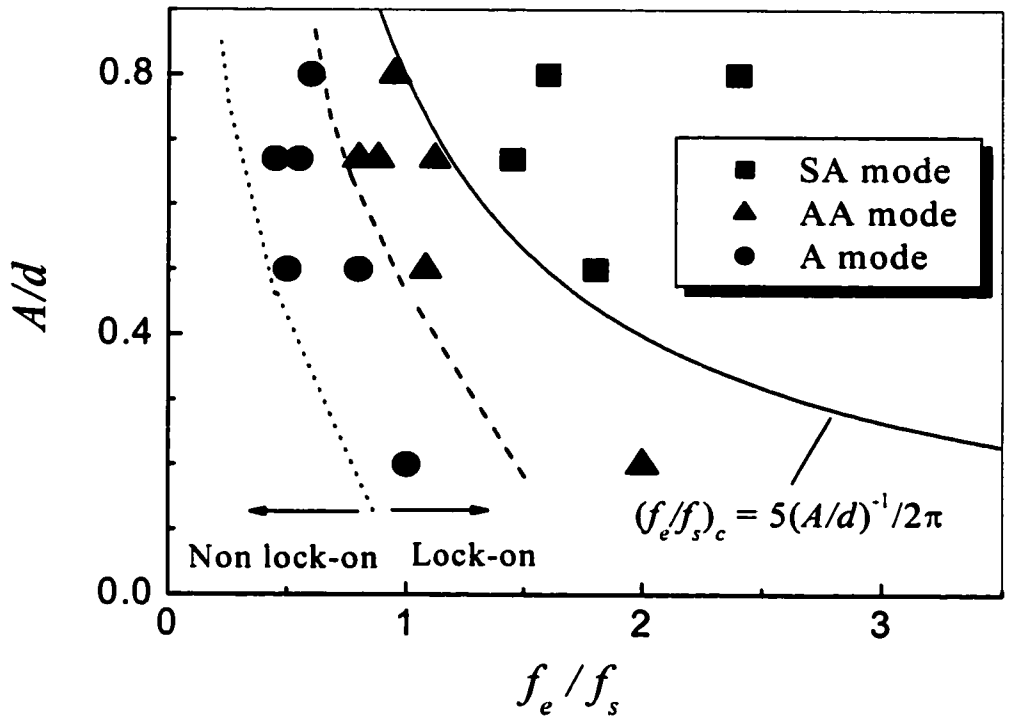

Figure 3-19 Dependence of the flow structure on A/d and f_e/f_s. ——, indicative of separation between the AA and SA mode; ------, indicative of separation between the A and AA mode; ·····, indicative of separation between the non lock-on and lock-on state.

3.7 Conclusions

The effect of a streamwise oscillating cylinder at $f_e/f_s = 0 \sim 2$ and $A/d = 0.5 \sim 0.67$ on the downstream cylinder wake has been experimentally investigated for $L/d = 2.5 \sim$

4.5 and $Re = 150 \sim 1150$ using the LIF, PIV and hot-wire techniques. The mean pressure, drag and lift on the downstream cylinder were also measured. The investigation leads to the following conclusions.

The flow structure behind the cylinders depends on the combination of A/d and f_e/f_s. Three distinct flow regimes have been identified for $0 < f_e/f_s < 2$ and $A/d = 0.5 \sim 0.67$ as summarized in Figure 3-20, i.e., the symmetric-antisymmetric complex street (SA-mode), the antisymmetric-antisymmetric complex street (AA-mode) and single antisymmetrical street (A-mode). The SA-mode occurs for $f_e/f_s > (f_e/f_s)_c$ (about 1.45 for $A/d = 0.67$, 1.6 for $A/d = 0.5$). The upstream oscillating cylinder generates binary vortices symmetrically arranged about the centreline, each binary vortex consisting of a pair of counter-rotating vortices. Meanwhile, the downstream cylinder sheds vortices alternately. Its frequency is one half of the oscillation frequency. A complex vortex street occurs behind the downstream cylinder, which includes two outer rows of symmetrically arranged binary vortices originating from the upstream oscillating cylinder and two inner rows of staggered vortices generated by the downstream stationary cylinder. Analysis has been developed to predict the occurrence of the SA-mode flow structure, which is in excellent agreement with the experimental data. The AA-mode occurs for 0.8 ($A/d = 0.67$) $\sim$ 1.0 ($A/d = 0.5$) $\lesssim f_e/f_s \lesssim (f_e/f_s)_c$, when alternate vortex shedding occurs for both cylinders. The flow behind the downstream cylinder is characterised by a complex vortex street that consists of two outer rows of binary vortices, originated from the upstream cylinder, and two inner rows of single vortices shed by the downstream cylinder. The vortices in the two outer or two inner rows are spatially antisymmetrical about the centreline. The A-

mode emerges behind the downstream cylinder at $0.45 \sim 0.5 \lesssim f_e/f_s \lesssim 0.8$ (A/d =0.45)~ 1.6 (A/d = 0.67). In general, f_e/f_s, at which a particular mode of the flow structure occurs, decreases as A/d increases.

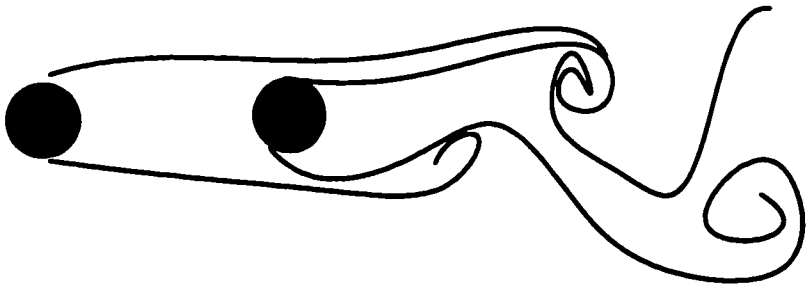

(a)

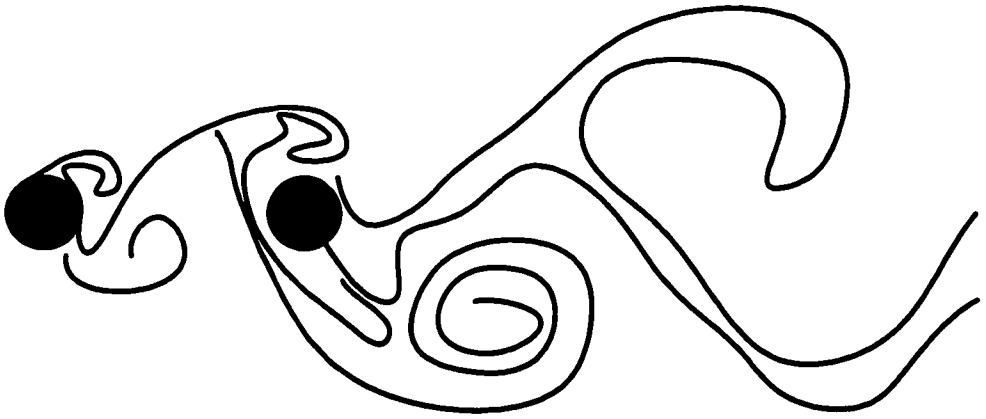

(b)

Figure 3-20 Summary of dominant flow structures. (a) $f_e/f_s = 0$; (b) $0.45 \sim 0.5 < f_e/f_s < 0.8 \sim 1.0$.

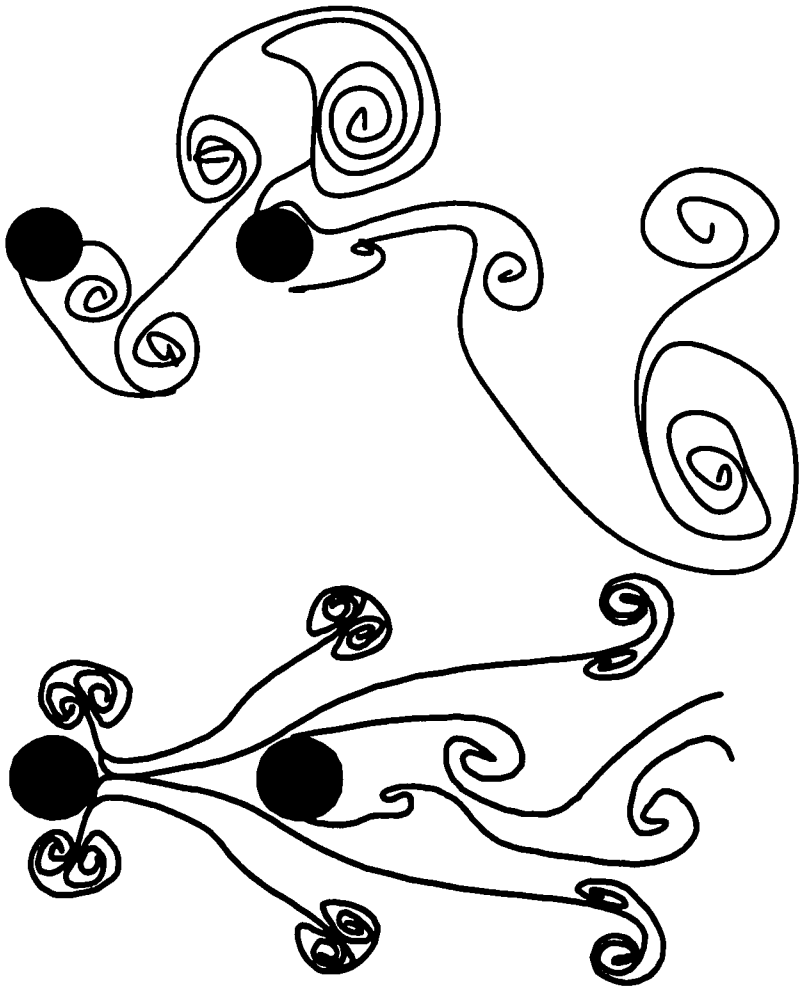

(c)

(d)

Figure 3-20 (Continued). (c) $0.8 \sim 1.0 < f_e/f_s < (f_e/f_s)_c$; (d) $f_e/f_s > (f_e/f_s)_c$. $2.5 \leq L/d \leq 4.5$, $0.5 \leq A/d \leq 0.67$.

The drastic in the flow structure with f_e/f_s at a fixed A/d results in different pressure distribution on the downstream cylinder and further results in a variation on the mean drag. The mean drag is largest for the AA-mode and smallest for the SA-mode. In

all cases, the mean drag is significantly larger than the case of two stationary cylinders of the same L/d. This is linked to the generation of vortices between the cylinders by the oscillation of the upstream cylinder. In contrast, there are no vortices generated between the two stationary cylinders.

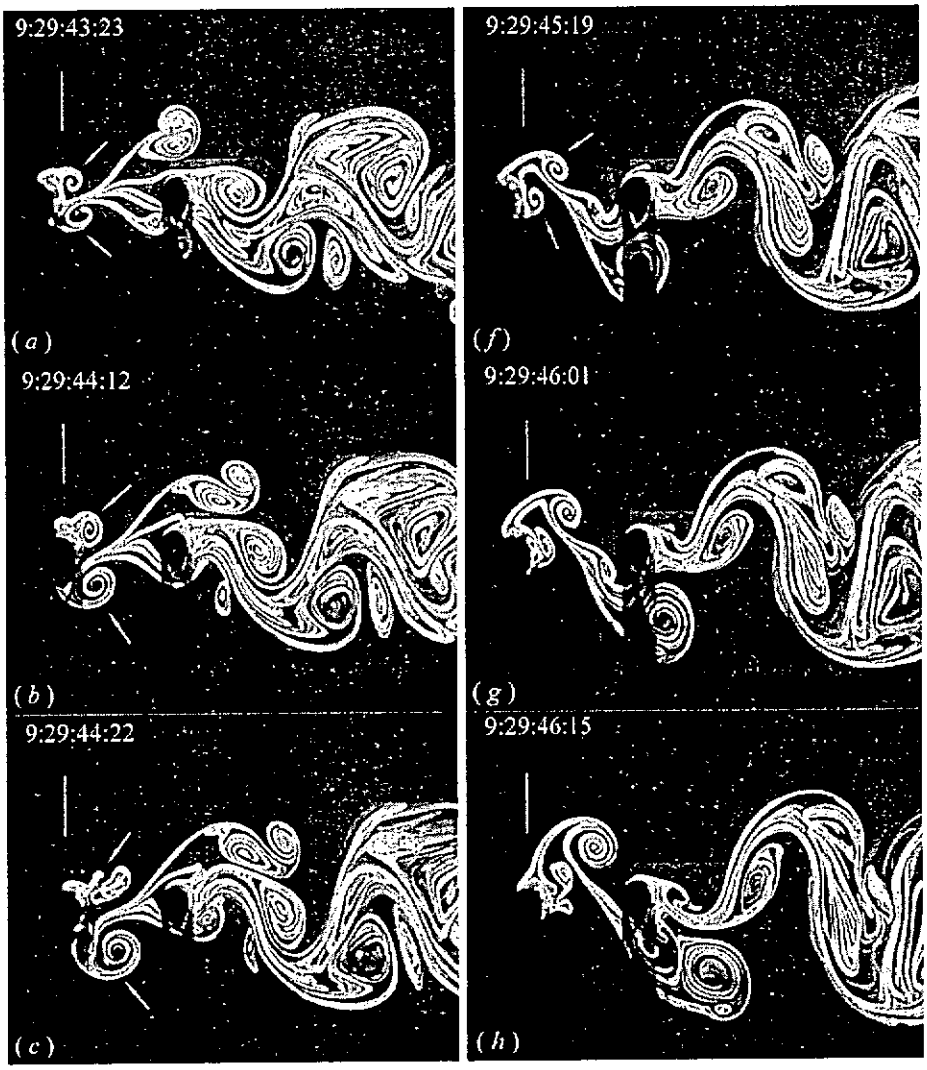

Figure 3-21 Variation from SA-mode (a) to AA-mode (g, h, i, j) during the frequency ratio reduces from 1.7 to 1.5. $L/d = 3.5$, $A/d = 0.5$ and $Re = 300$.

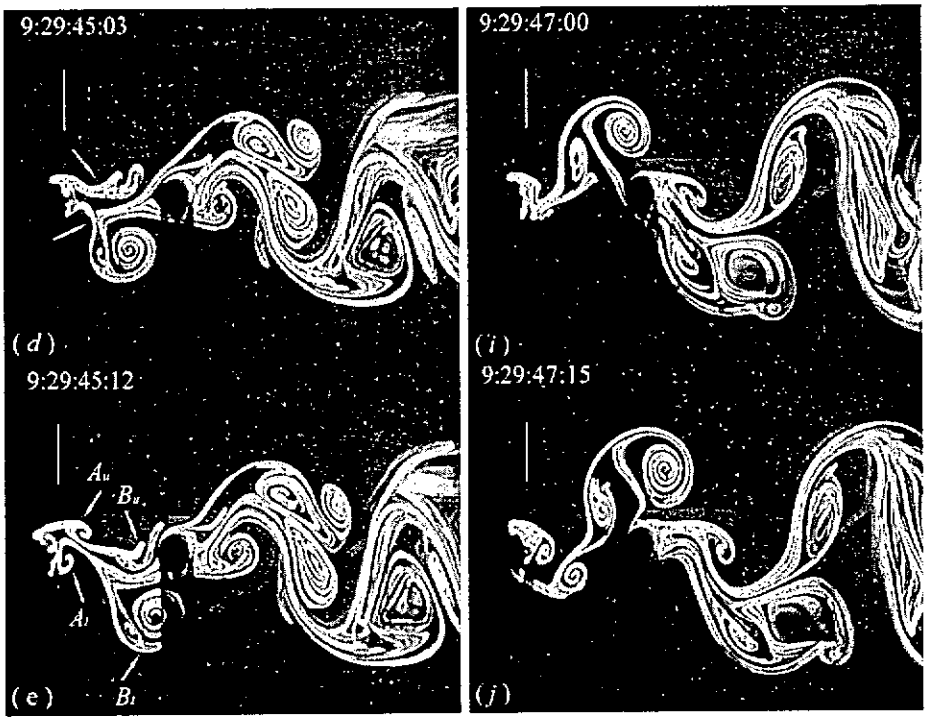

Figure 3-21 (Continued).

In the wake of two inline stationary cylinders, the flow structure depends on *L/d*. The critical *L/d* may vary with *Re* because of the *Re* dependence of the vortex formation length. When the upstream cylinder oscillates, however, the oscillation appears to control fluid dynamics around the two cylinders and *Re* is probably of secondary importance (Figure 3-21), showing a negligible effect on the occurrence of the flow structure of different modes. The occurrence of the flow structure mode is further independent of *L/d* (= 2.5 ~ 4.5).

CHAPTER 4

WAKE BEHIND A STATIONARY CYLINDER AND A STREAMWISE OSCILLATING CYLINDER

4.1 Introduction

In Chapters 1 to 3, interactions of a streamwise oscillating cylinder in the presence/absence of a downstream cylinder have been addressed. In spite of these studies, the possible impact of the streamwise structural oscillation on the flow field is far from complete. For example, how would the flow be affected if a streamwise oscillating cylinder is immersed in a stationary-cylinder wake? What is the dominant flow structure when the cylinder oscillation is locked on with the vortex shedding? How would the flow structure change in the absence of the lock-on phenomenon? These issues are interesting and motivate the investigation in this chapter.

This work aims to investigate interference between a stationary cylinder and a downstream streamwise oscillating cylinder, specifically, to address the issues raised above. The interference is possibly affected by a number of dimensionless parameters,

including L/d, f_e/f_s and the Reynolds number Re. The focus is on the effect of L/d on the flow structure. A laser-illuminated fluorescence (LIF) technique is employed to visualize the flow structure behind the stationary and the downstream oscillating cylinder. The flow structure is compared with that behind two stationary cylinders.

4.2 Experimental Details

The LIF measurements were carried out in a water tunnel. The details of the water tunnel have been documented in Chapters 1, 2 and 3. Two inline acrylic circular tubes of an identical diameter $d = 0.01$ m were cantilever-supported in the horizontal mid-plane of the working section. The gap between the cylinder free end and the working section wall was about 0.5 mm, thus resulting in a blockage of about 6.7%. The downstream cylinder, driven by a D.C. motor through a linkage system, oscillated harmonically in the streamwise direction. The D. C. motor was controlled by a microcomputer so that the desired oscillating frequency of the cylinder could be precisely obtained. The structural oscillation amplitude was fixed at $A/d = 0.5$ and f_e/f_s investigated ranged from 0 to 2.

Again, dye (Rhodamine 6G 99%), which has a faint red color and becomes metallic green when excited by laser light, was introduced through one injection pinhole located at the mid-span of each cylinder at 90°, both clockwise and anti-clockwise, respectively, from the leading stagnation point. A thin laser sheet, which was generated by laser beam sweeping, provided illumination over $0 \leq x/d \leq 10$ at the vertical mid-plane of the working section. A Spectra-Physics Stabilite 2017 Argon Ion laser source with a maximum power output of 4 watts was used to generate the laser beam. The dye-marked

vortex streets were recorded by a professional digital video camcorder (JVC GY-DV500E) at a framing rate of 25 frames per second. Measurements were carried out for L/d = 2.5, 3.5 and 4.5 and Re = 150, 300, 600 and 1000, where U_∞ is the free-stream velocity and ν is the kinematic viscosity.

4.3 Flow Structure behind two Stationary Cylinders

Zdravkovich (1987) categorized the flow around two inline stationary cylinders into three flow regimes for $L/d < 6$. At $L/d < 1.2 \sim 1.8$, the free shear layers from the upstream cylinder do not reattach on the downstream cylinder; they roll up to form a vortex street behind the downstream cylinder. For $1.2 \sim 1.8 < L/d < 3.4 \sim 3.8$, there is again no vortex shedding from the upstream cylinder, but the free shear layers from the upstream cylinder reattach on the downstream cylinder. A vortex street is generated behind the downstream cylinder. For $L/d > 3.4 \sim 3.8$, i.e., the critical spacing, vortices are generated from both cylinders. Furthermore, the shedding of vortices from the two cylinders is synchronized. A binary vortex street is developed behind the downstream cylinder. Igarashi (1981) proposed a similar classification. Nevertheless, the LIF measurements were conducted presently for two stationary cylinders of L/d = 2.5 and 4.5, which covered two flow regimes, to provide data for comparison with that when the downstream cylinder oscillates. Experiments were also carried out at L/d = 3.5 in order to examine the flow structure near the critical L/d.

Figure 4-1 shows typical photographs from the LIF flow visualization for L/d = 2.5, 3.5 and 4.5 at Re = 300.

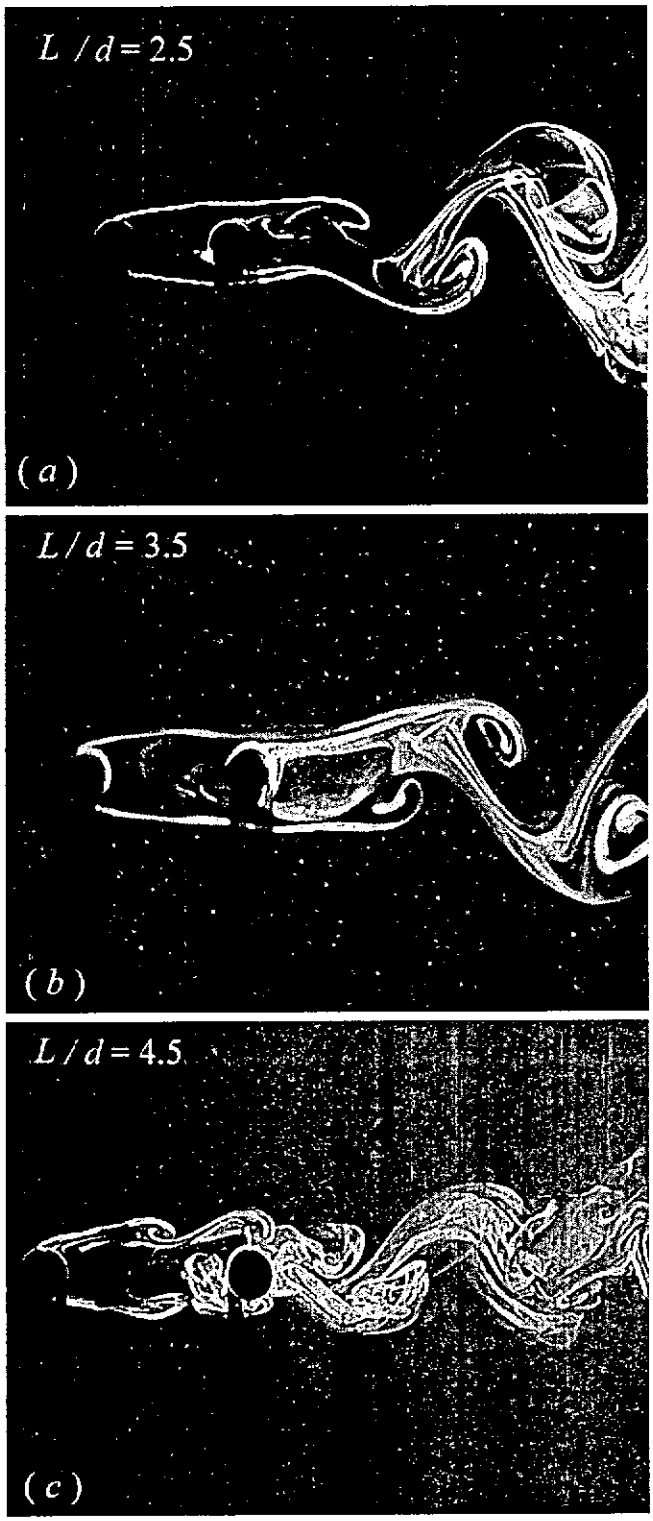

Figure 4-1 Typical flow structures behind two inline stationary cylinders at various L/d ($f_e/f_s = 0$, $Re = 300$).

Evidently, vortices are shed only from the downstream cylinder for L/d = 2.5 and 3.5 since the two L/d values fall into the same flow regime. At L/d = 4.5, vortices are shed from both cylinders. The observation agrees with previous reports (e.g., Igarashi 1981; Zdravkovich 1987).

4.4. Effect of Oscillation on the Flow Structures

When the downstream cylinder oscillates, the flow structure is not dependent on L/d only but also Re, f_e/f_s and A/d. This section is largely devoted to the flow behaviors at different L/d. It has been seen that in the case of stationary cylinders at L/d = 3.5 and Re = 300, vortices are alternately shed from the downstream cylinder but not from the upstream cylinder. This is completely different when the downstream cylinder oscillates. Oscillation phases of the downstream cylinder for Figures 4-3 to 4-5 are illustrated in Figure 4-2. Figure 4-3 presents the sequential photographs of various phases in a typical cycle of the cylinder oscillation for L/d = 2.5, f_e/f_s = 1.8 and Re = 300. The specific phases are indicated in a drawing where t and X represent time and the streamwise displacement from the reference position (X = 0) of the downstream cylinder, respectively. The maximum displacement A is $0.5d$. Note that the shear layers from the upstream cylinder now appears to be rolling up to form vortices near the downstream cylinder probably as a result of interaction between the shear layers and the oscillation of the downstream cylinder. Furthermore, the vortices from both cylinders occur symmetrically about the flow centerline. The symmetrical vortex street behind the downstream cylinder does not seem to be stable though; it quickly collapsed, with a

staggered vortex street emerging downstream. The frequencies of the vortices shed from the cylinders were estimated by means of counting consecutive vortices (about 20 pairs) for a certain period. It has been verified that the vortex shedding frequency, $f_{s,d}$ from the downstream cylinder is identical to that, $f_{s,u}$, from the upstream cylinder, both locking on with f_e. A similar observation is made for $L/d = 3.5$ (Figure 4-4).

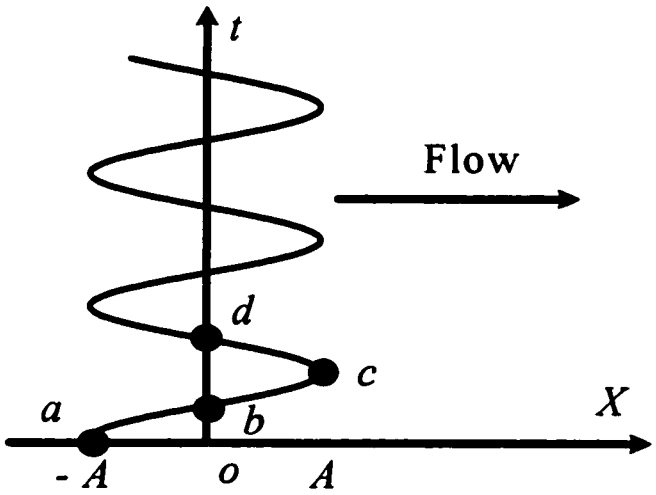

Figure 4-2 Phases of the oscillating downstream cylinder in the Figures 4-3 to 4-5.

As L/d reaches 4.5, both upstream and downstream cylinder shed vortices (Figure 4-5), rather similar to the case of the stationary cylinders. The wake width, however, increases substantially. The flow structure is totally different from that when $L/d \leq 3.5$. The vortices are shed alternately from each side of either cylinder; a staggered arrangement of vortices occurs behind the downstream cylinder.

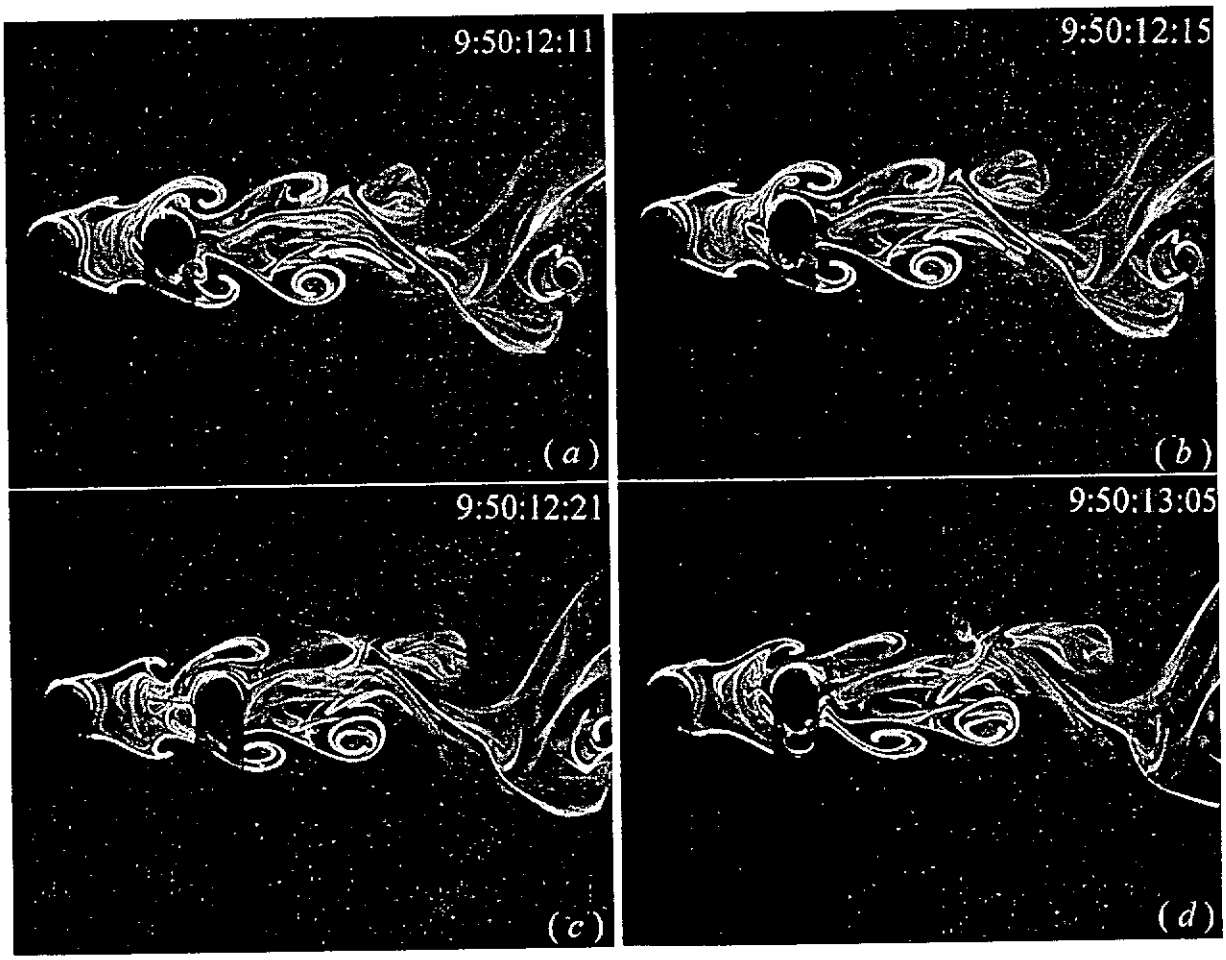

Figure 4-3 Symmetric vortex formation from two inline cylinders at L/d = 2.5 in one oscillation cycle (the downstream cylinder oscillates at A/d = 0.5). Re = 300 and f_e/f_s = 1.8.

When a streamwise oscillating cylinder is placed in the near wake of a stationary cylinder, the excitation motion by the oscillating cylinder may dominate, in particular at a small L/d. Subsequently the free shear layers separated from the upstream cylinder as well as those from the downstream cylinder may lock on with the downstream cylinder oscillation. Therefore, we see a symmetrical vortex shedding from the downstream cylinder (Figures 4-3 and 4-4).

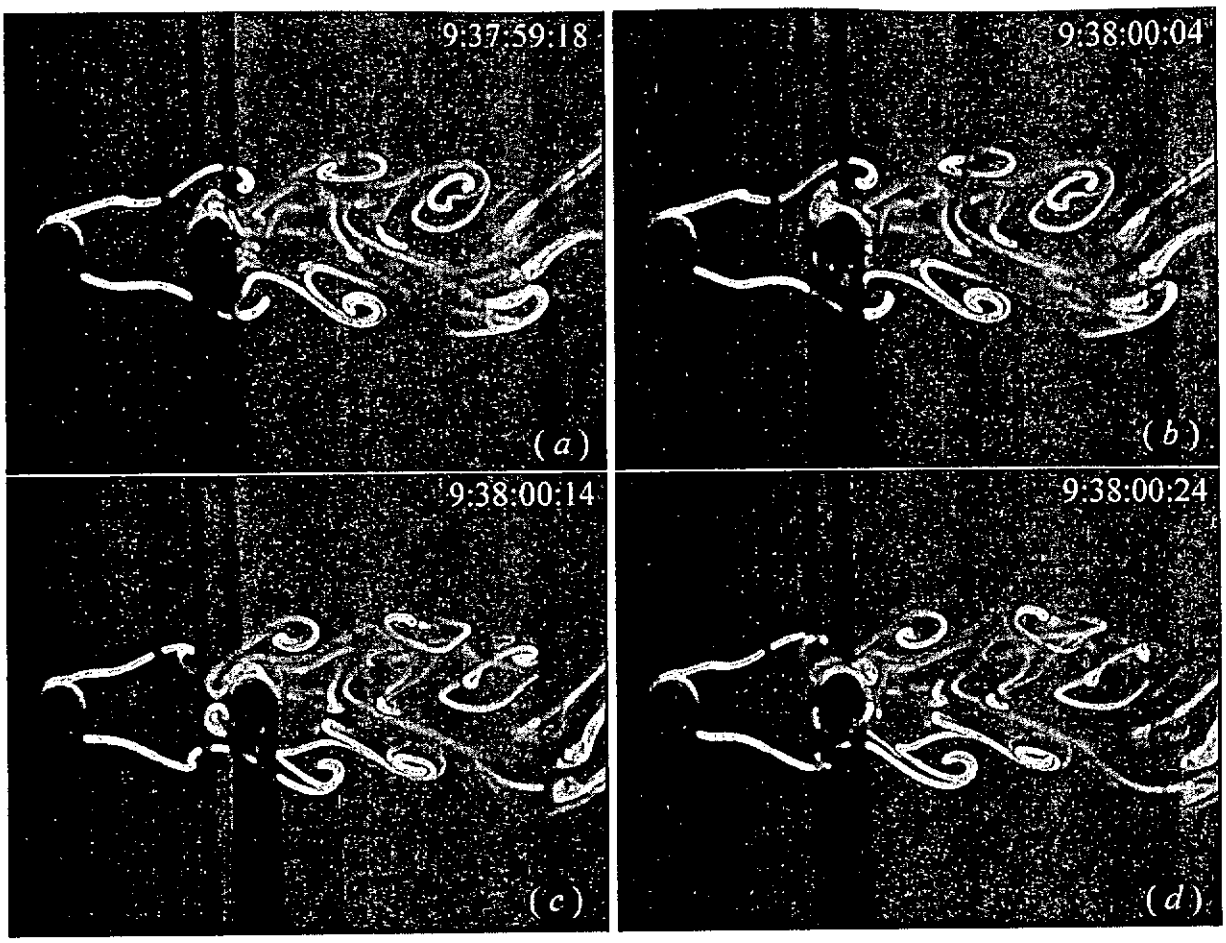

Figure 4-4 Symmetric vortex formation from two inline cylinders at L/d = 3.5 in one oscillation cycle (the downstream cylinder oscillates at A/d = 0.5). Re=300 and $f_e/f_s = 1.8$.

On the other hand, for large L/d, the excitation of the oscillating cylinder may not be strong enough to alter vortex shedding from the upstream cylinder. Thus, the classical vortex shedding occurs, namely, vortices are shed alternately from either side of the upstream cylinder. The spatially anti-symmetrically arranged vortices subsequently

impose an alternate excitation force on the downstream oscillating cylinder, which suppresses the symmetrical vortex shedding, induces alternate vortex shedding. The scenario corroborates the findings by Li *et al.* (1992) that, at a large *L/d*, the street generated by the upstream cylinder was important compared to the forced oscillation and dominated the flow, but at small *L/d* this street became weak and had little effect on the downstream cylinder wake.

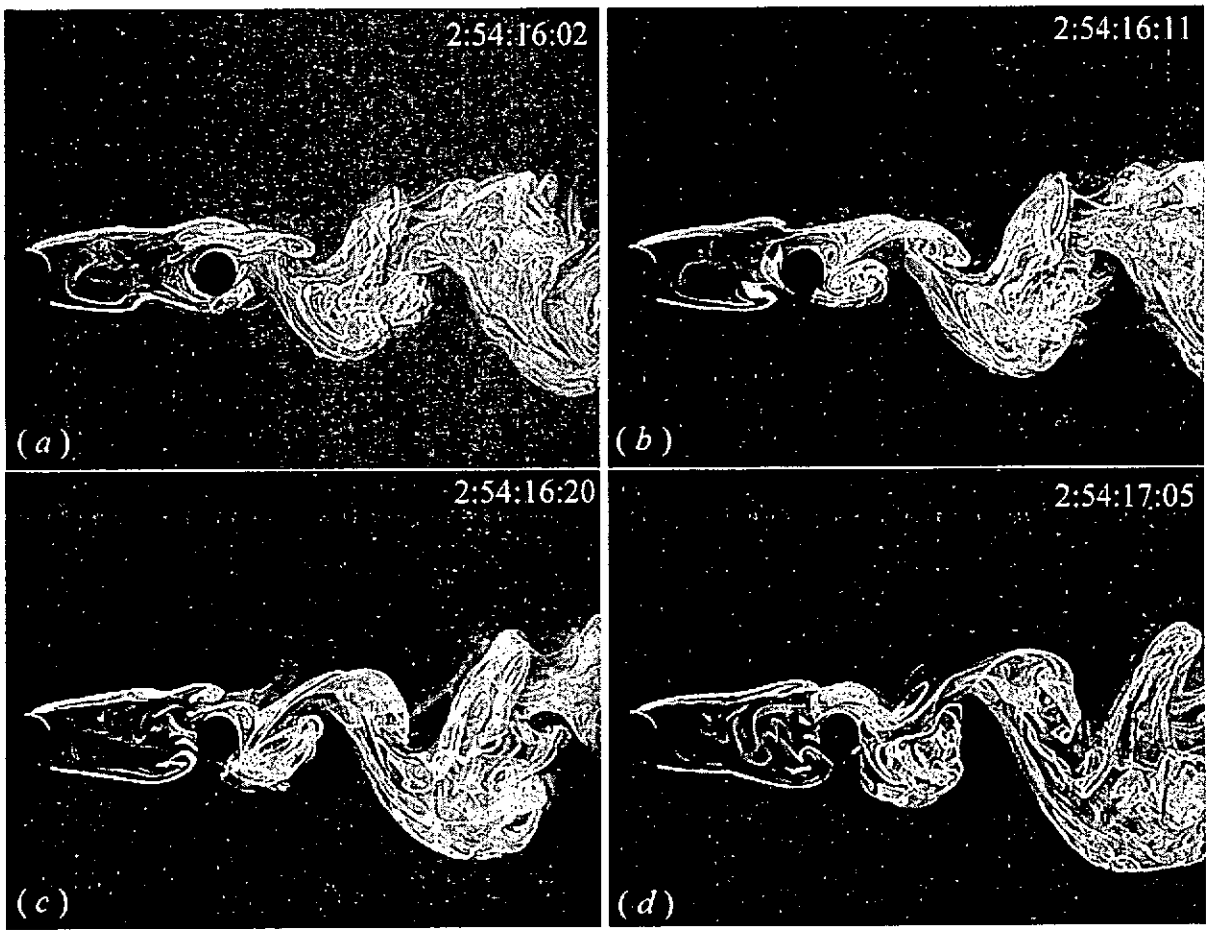

Figure 4-5 Anti-symmetric vortex formation from two inline cylinders at L/d = 4.5 (downstream cylinder oscillates at A/d = 0.5). Re = 300 and f_e/f_s = 1.8.

4.5 Conclusions

The interference between the wakes of a stationary cylinder and an inline downstream cylinder that oscillates in the streamwise direction has been investigated based on flow-visualization. With the oscillation of the downstream cylinder fixed at A/d = 0.5 and f_e / f_s = 1.8, the investigation focuses on the effect of L/d on the flow structure. Two flow regimes have been identified, i.e., the 'single-cylinder shedding regime' and 'two-cylinder shedding regime'. At a small L/d, the streamwise oscillation of the downstream cylinder dominates. The shear layers separated from the upstream cylinder do not have sufficient space to develop into vortices, while those from the downstream cylinder are shed symmetrically to form a symmetrical vortex street. The flow structure is in distinct contrast with the case of two stationary cylinders where vortices are shed alternately from the downstream cylinder. As L/d increases, the oscillation effect on the shear layer separation from upstream cylinder impairs so that the alternate vortex shedding resumes. The anti-symmetrically arranged vortices generated by the upstream cylinder may subsequently impose an alternate excitation on the downstream oscillating cylinder, which suppresses the symmetrical vortex shedding, inducing alternate shedding.

CHAPTER 5

EFFECTS OF REYNOLDS NUMBER ON FLOW STRUCTURES BEHIND TWO SIDE-BY-SIDE CYLINDERS

5.1 Introduction

Two side-by-side circular cylinder wake has attracted considerable interest in the past because of its practical significance in many branches of engineering (Chapter 1). As a result, our understanding of this flow has been greatly improved. However, many aspects remain to be clarified, in particular, in the asymmetrical flow regime, i.e., $T/d <$ 2.0. Literature data indicates a lack of consistency in the previously reported vortex shedding frequencies for the range as reviewed in Section 1.2.3, for $1.2 < T/d < 1.5$. Ishigai *et al.* (1972) measured two dominant frequencies in the range $T/d = 1.25 \sim 1.5$, namely $f_0^* = f_0 d / U_\infty \approx 0.1$ and 0.3, respectively, where f_0 is the dominant frequency and U_∞ is the free-stream velocity. The two frequencies were also detected by Spivac (1946) in the range, $T/d = 1.5 \sim 2.0$. Spivac further detected a frequency at 0.2, which could be interpreted as the second harmonic of 0.1. However, he failed to detect $f_0^* = 0.3$ at $T/d \approx$ 1.25. Kim & Durbin (1988) measured two frequencies, near 0.1 and 0.3, respectively, for

T/d = 1.5 ~ 2.0, but detected only one, $f_0^* = 0.1$, for T/d < 1.5. Are these scattered observations related to the effect of initial conditions, especially Re? Does the effect depend on T/d? How is the flow structure affected? These questions motivate the present investigation.

This chapter aims to study the effect of Re on the flow structure behind two side-by-side cylinders and to investigate the possible relationship between the flow structure and the scattered observation of the dominant frequencies. The flow structures were measured using a laser-induced fluorescence (LIF) visualization technique and the particle image velocimetry (PIV) method. The qualitative data is examined along with the quantitative information of the dominant frequencies determined from the measurements of two hot wires.

5.2 Experimental Details

5.2.1 LIF visualization in a water tunnel

The same water tunnel and LIF experimental facilities employed in Chapters 2 to 4 were used in this measurement. Two side-by-side acrylic circular tubes with an identical diameter d = 10 mm were horizontally mounted 0.20 m downstream of the exit plane of the tunnel contraction and placed symmetrically to the mid-plane of the working section. They spanned the full width of the tunnel. The resulting blockage was 13.3%. The effect of this blockage was corrected for the final results. Similarly, dye (Rhodamine 6G 99%) was introduced through injection pinholes located at the mid-span of each cylinder at

$\pm 90°$ from the forward stagnation point. A thin laser sheet, which was generated by laser beam sweeping, provided illumination vertically over $0 \leq x/d \leq 10$ at the mid-plane of the working section. A Spectra-Physics Stabilite 2017 Argon Ion laser with a maximum power output of 4 watts was used to generate the laser beam and a professional digital video camcorder (JVC GY-DV500E), set perpendicular to the laser sheet, was used to record the dye-marked vortex streets at a framing rate of 25 frames per second. Experiments were carried out for $T/d = 1.2$ to 1.6 at Re ($\equiv U_\infty d / \nu$) = 150 ~ 1000.

The LIF measurement was also conducted in the wind tunnel using the PIV system. See Section 5.2.2 for more details.

5.2.2 Wind tunnel experiments

Both PIV and hot-wire experiments were carried out in a closed circuit wind tunnel to obtain both qualitative and quantitative data and also to cover a large range of Re. The wind tunnel has a square working section (0.6 m x 0.6 m) of 2.4m in length. The working section walls were made of optical glass to provide best quality in flow visualization and PIV measurements. The wind speed in the working section can be adjusted from about 0.3 m/s to 50 m/s. The wake was generated by two brass cylinders (d = 12.7 mm) arranged side-by-side. The cylinders were installed horizontally in the mid-plane and spanned the full width of the working section. They were located 20 cm downstream of the exit plane of the contraction. This resulted in a maximum blockage of about 4.2% and an aspect ratio of 47. In the free-stream, the longitudinal turbulence intensity was measured to be approximately 0.4%. Flow visualization was conducted in

the wind tunnel using the visualization function of the PIV system in order to investigate the flow structure at *Re* higher than that investigated in the water tunnel. Experimental setup was exactly the same as the PIV measurements. The camera was operated in the single frame mode. A wide-angle lens was used to increase the view-field up to $14.1d$ $\times 10.7d$. The recording interval between a pair of successive images was 0.2 s. Experiments were carried out for T/d = 1.2 to 1.6 and Re= 300 to 1500. More than 100 images were collected for each *Re*.

5.2.2.1 PIV measurements

A Dantec standard PIV2100 system was used as same as Chapter 2. Flow was seeded by the smoke, generated from Paraffin oil, of a particle size of 1 to 3 μm in diameter. Each image covered an area of 75mm × 60mm of the flow field, i.e., $x/d = 0.8d$ ~ $6.8d$ and $y/d = -2.5d \sim + 2.5d$. The horizontal image magnification was about 0.06mm/pixel. Each pulse lasted for 0.01 μs. The interval between two successive pulses was typically 50 μs. Thus, a particle would only travel 0.5 mm (8.3 pixels or 0.04 d) at U_∞ = 10 m/s. To minimize reflection noise, the cylinder surface and the working section wall hit by the laser-illuminated sheet were painted black. Furthermore, an optical filter was used to allow only the green wavelength (532 nm) generated by laser to pass. The raw vector field of particle displacement was computed using a cross-correlation algorithm (Willert & Gharib 1991), which was built into the correlator units in the Dantec FlowMap processor. Interrogation area consisted of 64 pixels ($\approx 0.3\ d$) with 25% overlap in the horizontal and vertical direction, respectively. Accordingly, the in-plane velocity vector field included 26×21 vectors, giving 26×21 vorticity points. The

spatial resolution for the vorticity estimate was about 0.23 d. The experiment was carried out for $T/d = 1.3$ and $Re = 350 \sim 680$.

5.2.2.2 Hot-wire measurements

The vortex shedding frequencies of the two cylinders were measured using two hotwires in the wind tunnel. Two single hot-wires were placed symmetrically at $x/d \approx 4$ and $y/d \approx \pm (T/2d + 2)$, respectively (Figure 5-1), to monitor simultaneously the instantaneous flow velocity behind each cylinder. Constant-temperature circuits were used for the operation of the hot wires. Experiments were carried out for $T/d = 1.2 \sim 1.6$ and $Re = 300 \sim 14300$. Signals from the circuits were offset, amplified and then digitized using a 16 channel (12bit) Analog/Digital board and a personal computer at a sampling frequency $f_{sampling} = 3.5$ kHz per channel. The duration of each record was about 40 s.

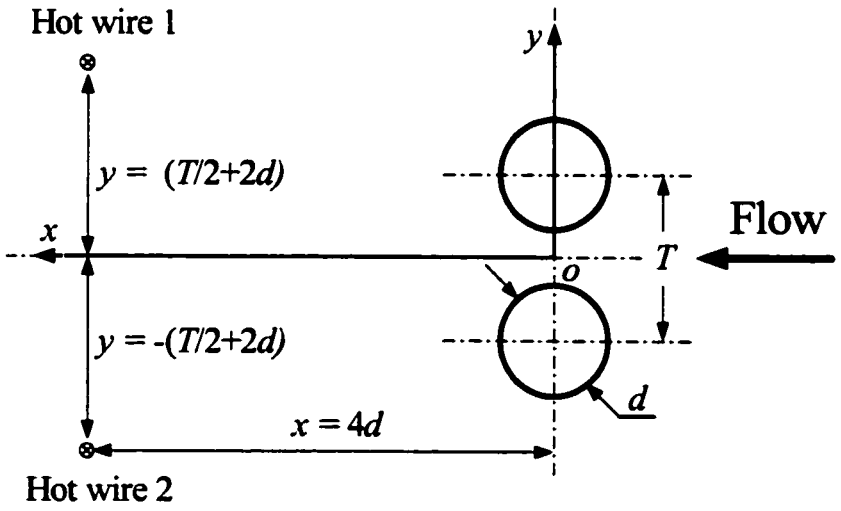

Figure 5-1 Schematic arrangement of hot-wires in the wind tunnel.

5.3 Effect of *T/d* and *Re* on Dominant Frequencies

As noted in the Introduction, previous reports of the number of dominant frequencies for $T/d = 1.2 \sim 1.5$ were not consistent (e.g., Ishigai *et al.* 1972; Spivac 1946; Kim & Durbin 1988). Zhou *et al.* (2002) speculated that a possible transition occurred between $T/d = 1.2 \sim 1.5$ from the regime of a wide and a narrow vortex street to that of a single vortex street. During transition, the gap flow would probably deflect, as evidenced by different base pressures associated with the two cylinders (Kim & Durbin 1988). However, gap vortices might or might not be generated, depending on the initial conditions or experimental set-up, thus giving rise to inconsistent observations. The present measurement indeed reconfirmed the occurrence of one dominant frequency at $f_0^* = f_0 d / U_\infty \approx 0.09$ or two at $f_0^* \approx 0.09$ and 0.3, respectively, for $1.25 < T/d < 1.6$. It was further found that the number of dominant frequencies was dependent on *Re* as well as *T/d*.

At $T/d = 1.3$ and $Re = 300$, the power spectra of both hot-wire signals (Figure 5-2) display one single peak at $f_0^* \approx 0.09$. As *Re* is increased to 500, the *u*-spectrum from hot wire 1 showed one more peak at $f_0^* \approx 0.3$, whereas the peak in the *u*-spectrum from hot wire 2 remains at $f_0^* \approx 0.09$. This suggests that the flow structure or pattern may be quite different between the low and high *Re*, which is verified by the flow visualization data (Section 5.4). More discussion will be provided in Section 5.4 on the occurrence of two dominant frequencies detected from hot wire 1.

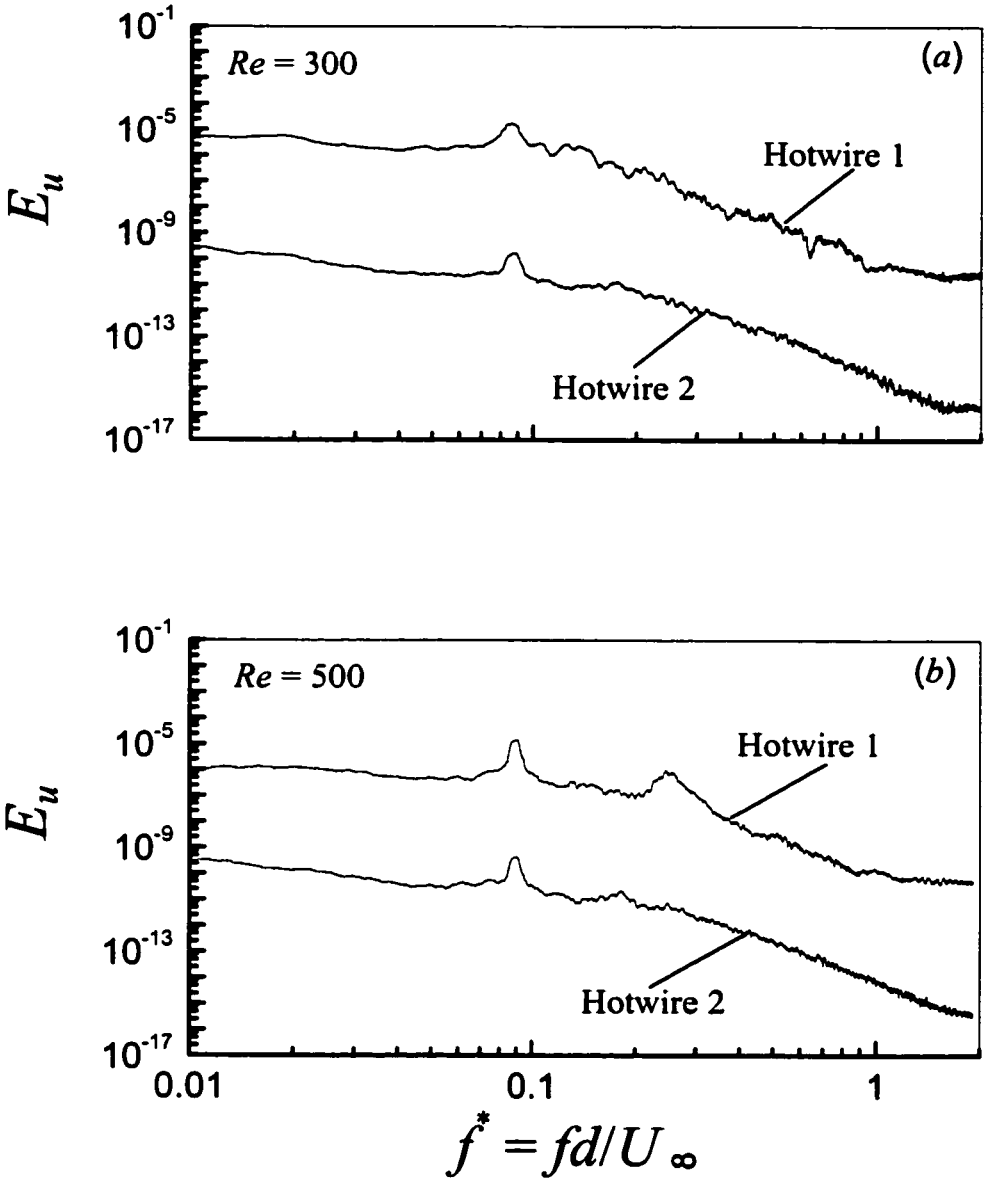

Figure 5-2 Typical power spectra of the hot-wire signal u at $T/d = 1.3$. The two hot wires were placed at $x = 4d$ and $y = \pm (T/2+2d)$ (see Figure 5-1).

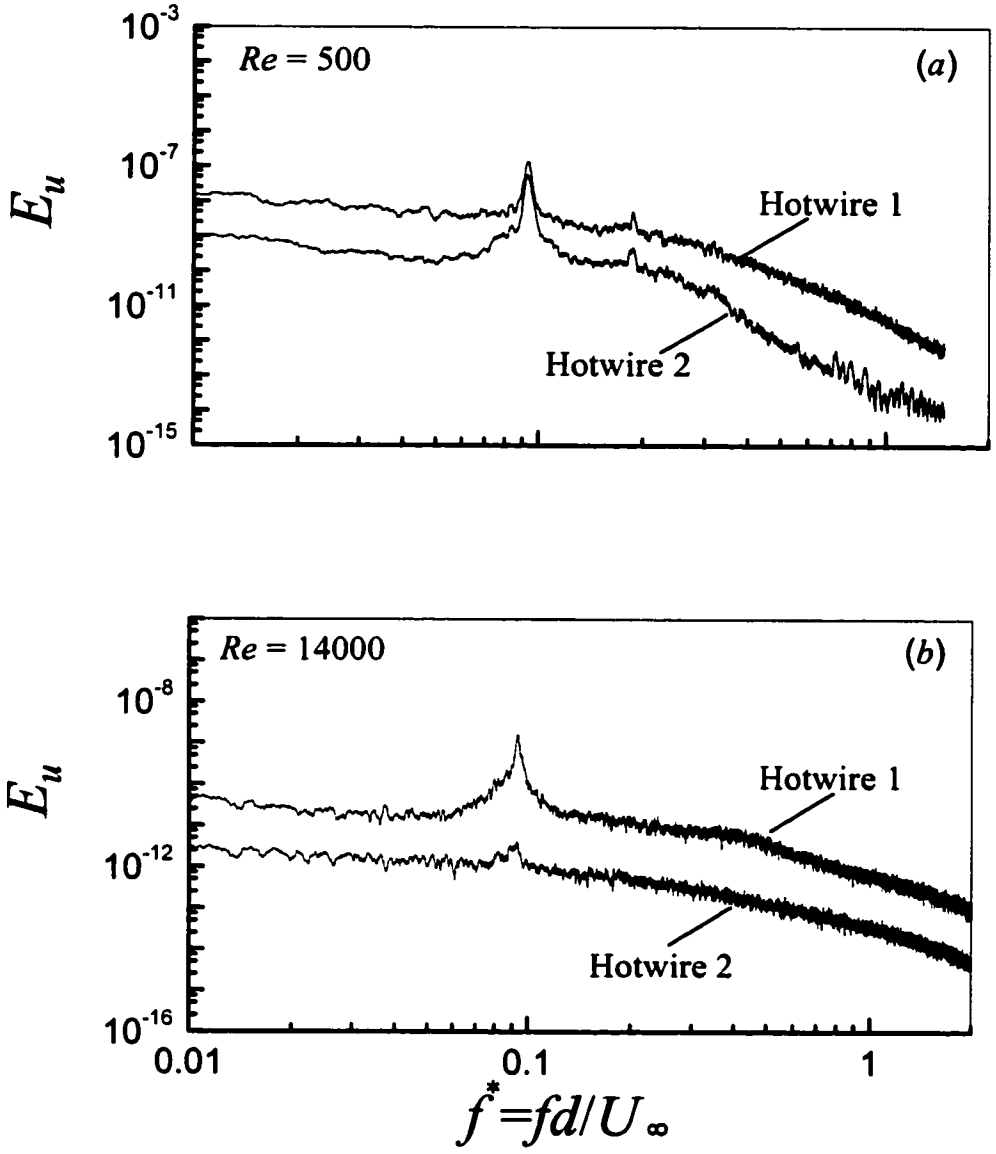

Figure 5-3 Typical power spectra of the hot-wire signal u at T/d = 1.25. The two hot wires were placed at $x = 4d$ and $y = \pm (T/2+2d)$ (see Figure 5-1).

Similar observations were made for 1.25 < T/d < 1.6, i.e., the detected dominant frequency changes from one to two as *Re* increases. However, at $T/d \leq 1.25$, one dominant frequency only was detected, as illustrated in Figure 5-3, which shows one single peak at $f_0^* \approx 0.09$ in the *u*-power spectra of both hot wires ($T/d = 1.25$), even though *Re* has been increased to 14,000. This could imply a flow structure different from that at $T/d > 1.25$, as confirmed in Section 5.4. Note that a minor peak occurs at $f_0^* \approx 0.18$ in Figure 5-3a, which is likely to be the second harmonic of $f_0^* \approx 0.09$.

Figure 5-4 summarizes the dominant frequencies detected at various *T/d*. The present data are essentially in agreement with those reported in the literature, which are also included in the figure. Apparently, one single frequency occurs at $f_0^* \approx 0.1$ for $T/d < 1.25$; it shifts to $f_0^* \approx 0.2$ for $T/d > 2.0$. When *T/d* is between 1.6 and 2.0, two frequencies occur. For $1.25 \leq T/d \leq 1.6$, one or two frequencies are possible, perhaps depending on the *Re*. Note that Bearman & Wadcock (1973) observed one dominant frequency at $f_0^* \approx 0.1$ for $1 < T/d < 1.5$. Zhang & Zhou (2001) measured the flow up to $x/d = 10$ behind three side-by-side cylinders ($T/d = 1.5$, $Re = 5800$) using both hot-wire and laser-induced fluorescence visualization techniques. They observed a wide wake behind the central cylinder and a narrow wake on each side of the wide wake. It was found that the vortical structures in the narrow wakes, which were shed from the side cylinders, interacted with the wide wake and could not be detected at $x/d \approx 5$ by hot wires.

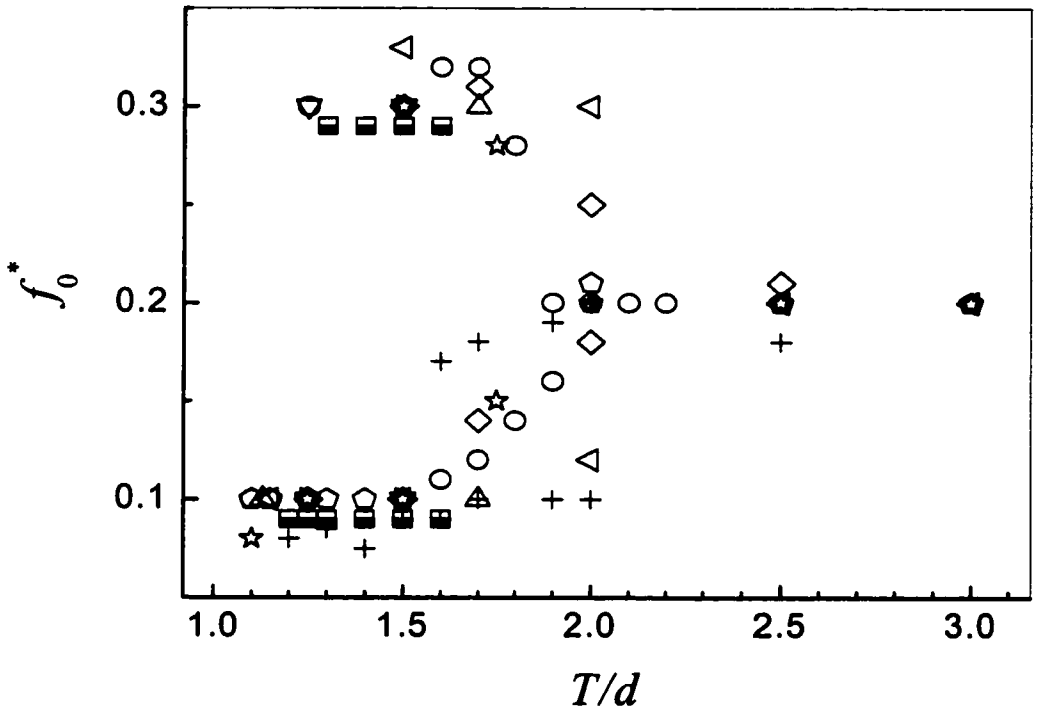

Figure 5-4 Dependence of dominant frequencies on spacing between two side-by-side cylinders in a cross flow. ⬠, Bearman and Wadcock (1973), *Re* = 25000; ▷, Ishigai *et* al. (1972), *Re* = 1500; ☆, Kamemoto (1976), *Re* = 30000; ◇, Kim & Durbin (1988), *Re* = 3300; +, Williamson (1985a), *Re* = 200; ▽, Quadflieg (1977), *Re* = 30000; ○, Spivak (1946), *Re* = 28000;◁, Sumner *et al.*(1999), *Re* = 1900; △, Zhou *et al.* (2001) *Re* = 120 & 3500; ⬓, present data, *Re* = 300 to 14300.

On the other hand, the vortical structures in the wide wake started to roll up at *x/d* ≈5 (*Re* > 450). They were very weak initially but grew in strength with increasing *x/d*,

resembling those in a screen near-wake, which were ascribed to the shear layer instability of the developing wake (Zhou & Antonia 1994; 1995). The two-cylinder case may bear a resemblance to that of three cylinders. This is supported by Zhou *et al.* (2001) observation at T/d = 1.7 that the two cross-stream vortices in the narrow wake amalgamated with the gap vortex in the wide wake, forming a single street downstream. The vortices seen in the wide wake may be generated from the shear layer instability in the developing wake, whereas those shed from the cylinder in the narrow wake probably disappear at $x/d \approx 5$. Note that Bearman & Wadcock (1973) placed their hotwire at $x/d \approx$ 6 and the flow Re was 2.5×10^4. It is well known that the vortex formation length behind an isolated cylinder reduces as Re increases (Gerrard 1966). This is probably also true for the flow behind two side-by-side cylinders, implying that the opposite-sign vortices in the narrow wake may amalgamate with the gap vortex in the wide wake at a location closer to the cylinders for large Re. Therefore, the narrow wake in Bearman & Wadcock's flow could have vanished before x/d = 6, thus leaving only the dominant frequency in the wide wake to be detected.

Figure 5-5 presents the dependence of single- or two-frequency detection on Re and T/d. Again, the data available in the literature are included. It is evident that the number of dominant frequencies is independent of Re provided that $T/d < 1.25$ or $T/d > 1.6$; one frequency occurs for $T/d < 1.25$ but two for $T/d > 1.6$ (but < 2.0). Between T/d = 1.25 and 1.6, the number of dominant frequencies depends on Re as well as T/d. The flow is dominated by one frequency for relatively low Re but two as Re is beyond a critical value. As T/d reduces, the transition from one dominant frequency to two occurs at a

higher *Re*. It is pertinent to point out that the critical *Re* where 'transition' occurs could be affected by the initial conditions, such as boundary conditions, wind tunnel, experimental setup, etc., other than *Re*.

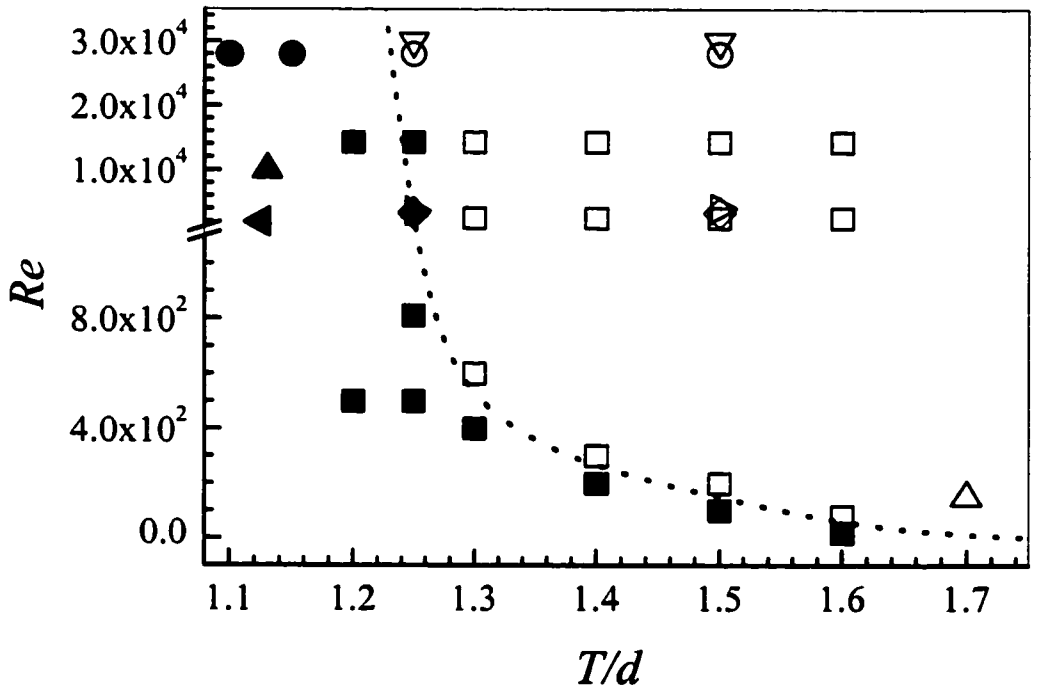

Figure 5-5 Effect of the Reynolds number on the number of dominant frequencies. The solid and open symbols represent the detection of one and two dominant frequencies, respectively; the dotted line is indicative only of the boundary between them. ▷, Ishigai *et* al. (1972);◆&◇, Kim & Durbin (1988); ▽, Quadflieg (1977); ●&○, Spivak (1946);◀, Sumner *et al.*(1999); ▲&△, Zhou *et al.* (2001); ■&□, present data.

5.4 Flow Structures

The dependence of dominant frequencies on both *T/d* and *Re* suggests a variation in the flow structure with these parameters, and it is important to clarify the correspondence between the typical flow structure or pattern and the dominant frequencies (Figure 5-5). Figure 5-6 presents the typical flow structure at $T/d = 1.4$ from the LIF measurement in the water tunnel. At $Re = 150$, the gap flow between the cylinders is biased downwards, resulting in one single vortex street behind the upper cylinder. A small closed near-wake region occurs behind the lower cylinder, without shedding any vortices (Figure 5-6a). This flow structure is rather stable. The same structure is observed for $Re < 300$. As *Re* reaches 300, the gap flow between the cylinders is deflected towards the upper cylinder, forming one narrow street behind the upper cylinder and one wide street behind the lower cylinder (Figure 5-6b). The gap flow may change the direction of deflection and is bi-stable. This flow structure remains unchanged even with further increases in *Re*.

The same observation was made in the wind tunnel using the flow visualization function of the PIV system. Figure 5-7 shows photographs taken at $T/d = 1.3$. The flow at $Re = 450$ (Figure 5-7a) displays one single vortex street, with a closed near-wake region identifiable behind the lower cylinder. At $Re = 1000$, the flow (Figure 5-7b) resembles that in Figure 5-6b, displaying two streets, one narrow and one wide, behind the cylinders. The simultaneous hot-wire measurements indicate one dominant frequency at $f_0^* \approx 0.09$ for the former and two at $f_0^* \approx 0.09$ and 0.3, respectively, for the latter.

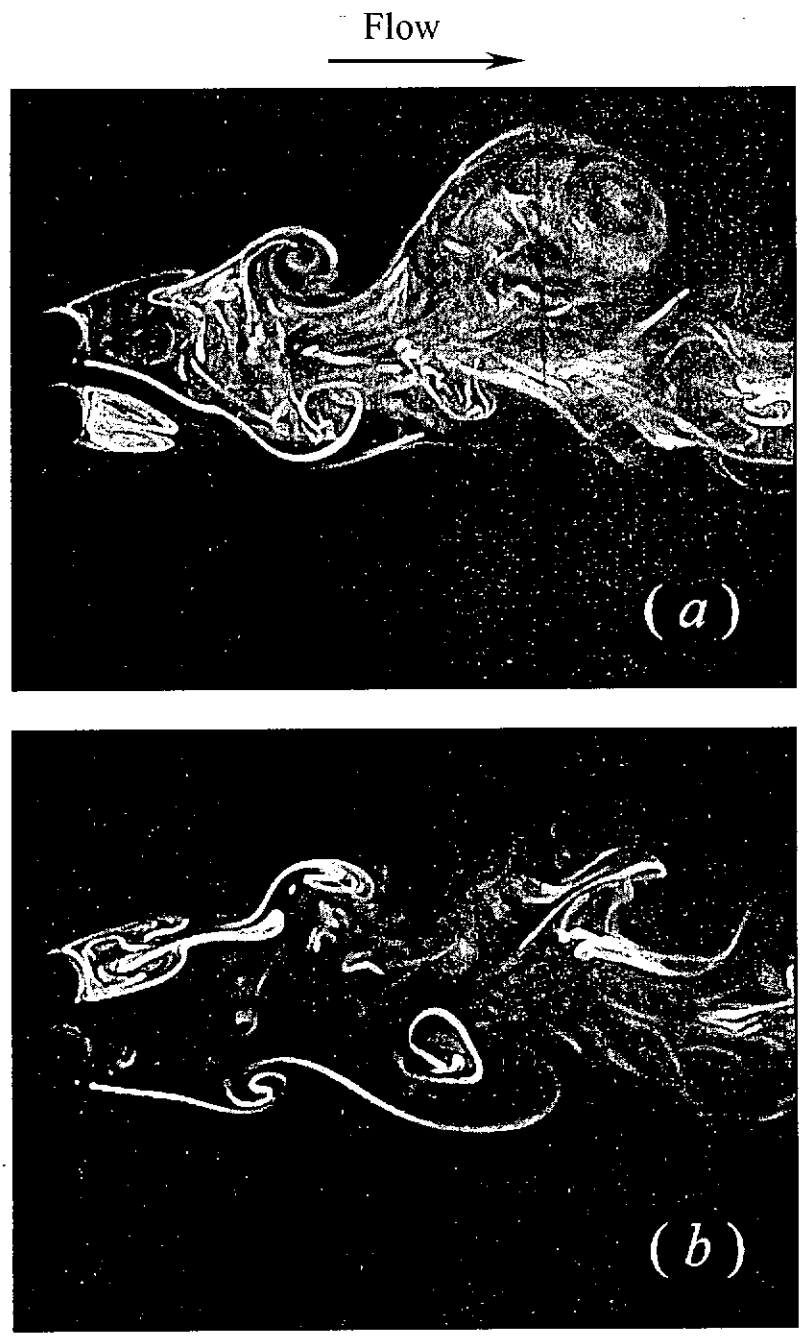

Figure 5-6 Typical flow patterns at $T/d = 1.4$ measured in the water tunnel: (a) one-street flow structure, $Re = 150$; (b) two-street flow structure, $Re = 300$. Flow is left to right.

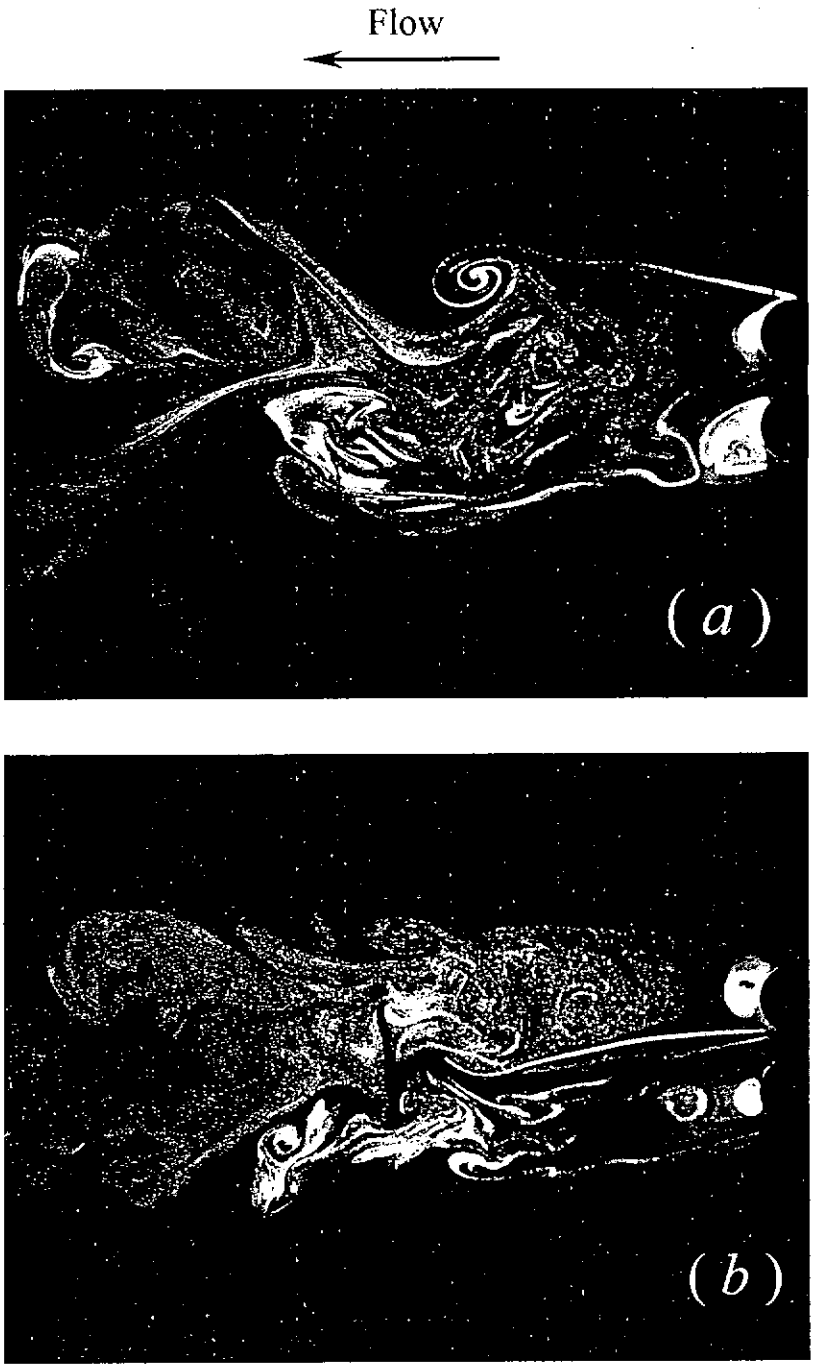

Figure 5-7 Typical flow patterns at T/d = 1.3 measured in the wind tunnel: (a) one-street flow structure, Re = 450; (b) two-street flow structure, Re = 1000. Flow is right to left.

The PIV data provides some quantitative information on the flow structure. The iso-contours of the spanwise vorticity $\omega^* = \omega d / U_\infty$ (Figure 5-8) at *T/d* = 1.3, derived from the PIV measurement of the velocity field, reconfirm the LIF results, i.e., as *Re* increases, the flow changes from one-street structure to two-street structure. The PIV measurement further indicates that for the one-street structure (Figure 5-8a) the vorticity concentration associated with the closed near-wake region is quite comparable to that of the vortex street. In the case of two streets (Figure 5-8b), the maximum vorticity concentration in the narrow street (upper) is comparable with that in the wide wake (lower). The maximum vorticity concentration associated with the inner shear layer, near y/d = 0, of the wide wake is 1.4, appreciably smaller than that (2.0) of the narrow wake or the two outer shear layers towards the free-stream. This may suggest a weak gap vortex in the wide wake. As a matter of fact, flow visualization data indicates that, frequently, the gap vortex in the wide wake could not be seen (e.g., Figure 5-6b).

Similar observation was made for *T/d* = 1.5 and 1.6, that is, one single vortex street occurs for relatively low *Re*, the structure turning into one narrow and one wide vortex street as *Re* increases. Furthermore, the former was dominated by one frequency, while the latter by two. For 1.6 < T/d < 2.0, the one-street structure was not observed, irrespective of the *Re* value. At *T/d* = 1.2 or smaller, however, the flow structure (Figure 5-9) is totally different. The closed near-wake region is absent. Vortices shed from the outer side only of the two cylinders, forming one single vortex street. At such a small *T/d*, the gap bleeding, without the presence of the gap vortex though, is identifiable. It is deflected upwards at higher *Re* (Figure 5-9b) but swerving around the upper cylinder at

lower *Re* (Figure 5-9a). One dominant frequency at $f_0^* \approx 0.09$ was detected across the wake. The present observation is consistent with previous reports (e.g., Sumner *et al.* 1999; Zhou *et al.* 2001).

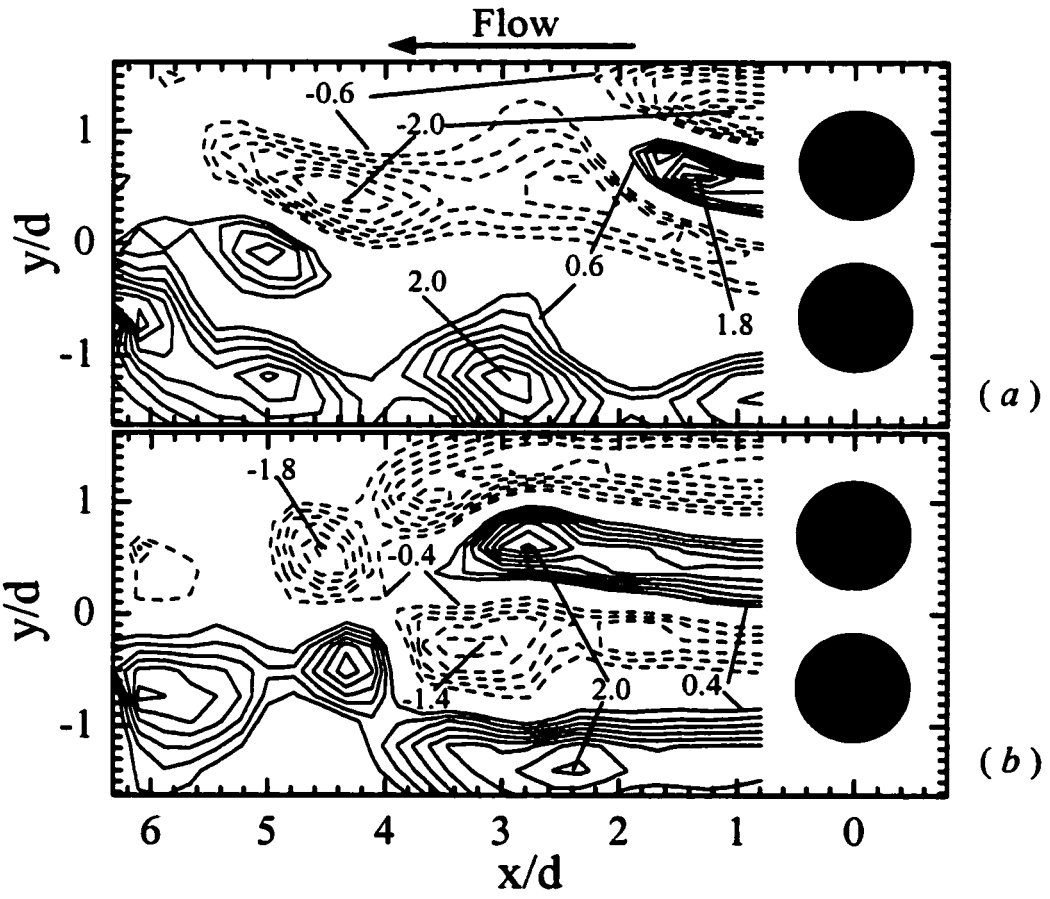

Figure 5-8 The PIV measurement of instantaneous vorticity contours $\omega^* = \omega d/U_\infty$, the contour increment = 0.2, T/d =1.3. (a) One-street flow structure, Re = 350; (b) Two-street flow structure, Re = 680.

It is well known (e.g., Schlichting & Gersten 2000) that a steady separation or closed near-wake is associated with an isolated circular cylinder in the *Re* range, 4 - 5 < *Re* < 30 - 48, and the periodic vortex shedding occurs for *Re* $\gtrsim$ 50. Measurements by Zhou *et al.* (2001) indicate that, as *T/d* is reduced, the pressure between the cylinders increases. This implies a decrease in the gap flow velocity. The corresponding actual *Re* will be small. This may explain why a small closed wake occurs in Figures 5-6a, 5-7a, and 5-8a. When the gap flow velocity increases beyond the critical *Re* for the periodic vortex shedding, a narrow wake is generated, as observed in Figures 5-6b, 5-7b, and 5-8b. The interpretation is also consistent with the observation (Figure 5-5) that the critical *Re* for the transition from the one- to the two-frequency regime increases as *T/d* decreases. For *T/d* < 1.25, because of the near-wall effect, the gap flow velocity is so small that the actual *Re* for the inner side of the cylinders cannot exceed the critical value for periodic shedding, irrespective of the value of U_∞. As a result, vortices shed from the outer layers only of the two cylinders, thus generating a single vortex street or single dominant frequency (Figures 5-3 and 5-9).

Peschard and Le Gal (1996) analyzed the stability of the coupled streets behind two side-by-side cylinders for 1.7 < *T/d* < 6.0 and classified the flow as in-phase locking, asymmetric locking, quasi-periodic and phase-opposition locking as *Re* increased from 90 to 150. A comparison between the present Figure 5 and their Figure 5 indicates that the asymmetric locking, quasiperiodic regime and phase opposition locking in fact correspond to the present two street regime, while in-phase locking coincides with part of

one street regime. However, there is a difference between one street regime and in-phase locking. One street regime consists of one vortex street and one small closed wake (e.g., Fig 5-6a), which is different from in-phase locking wakes.

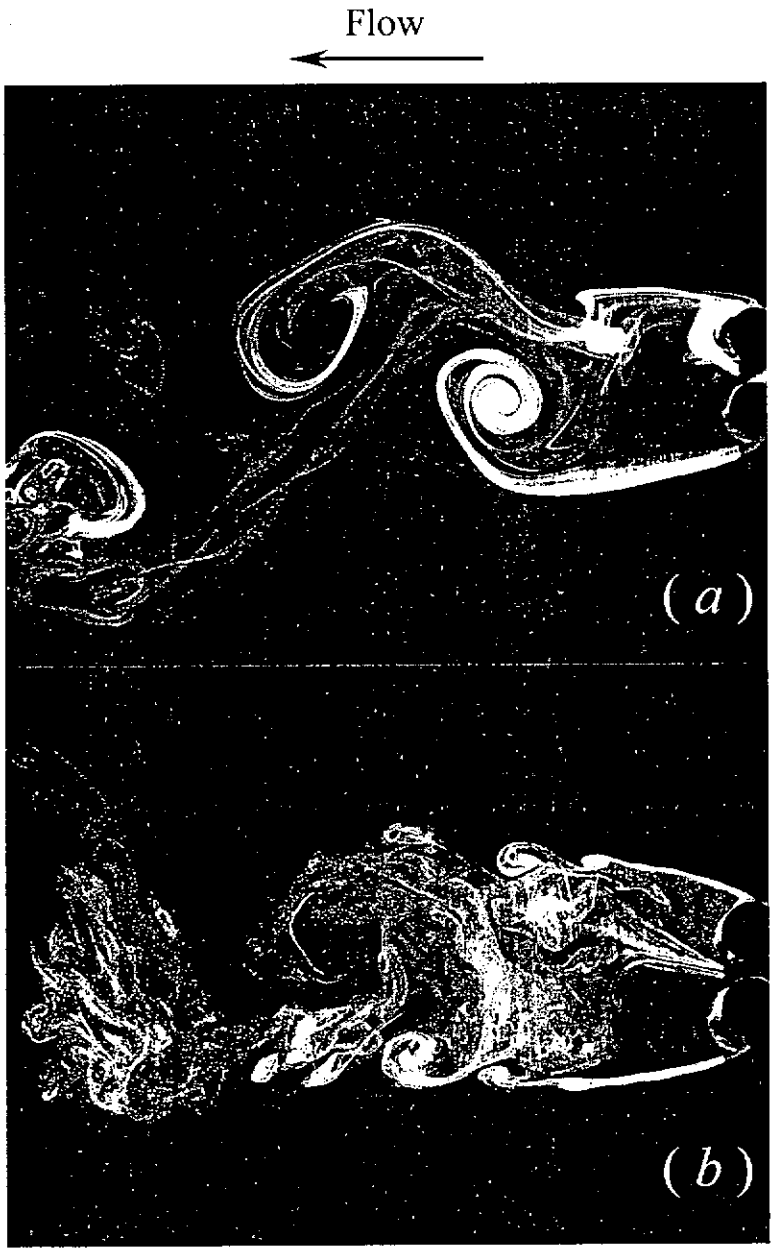

Figure 5-9 Typical flow patterns at T/d = 1.2 measured in the wind tunnel: (a) Re= 450; (b) Re = 1500. Flow is right to left.

5.5 Conclusions

The near wake of two side-by-side cylinders has been measured using LIF, PIV and hotwire techniques. The investigation focuses on the dominant frequencies, flow structures, and their relation in the asymmetrical flow regime, i.e., $T/d < 1.7$. The following conclusions can be drawn.

1 As $T/d < 1.25$, the near-wall effect is dominant; *Re* based on the gap flow velocity is so small that periodic vortex shedding cannot be induced from the inner side of the cylinders. As a result, vortices shed from the outer side only of the two cylinders, generating a single vortex street (see summary sketch 5-10a).

2 For $1.25 \lesssim T/d \lesssim 1.6$, two flow structures have been observed, as summarized in Figures 5-10b and 5-10c. At a relatively low *Re*, a small closed wake occurs behind one cylinder; the flow is characterized by one single vortex street, dominated by a frequency measured at $f_0^* \approx 0.09$. The occurrence of the small wake is probably due to the near-wall effect at small *T/d*. The effect gives rise to a small gap flow velocity. The Reynolds number based on this velocity is then substantially smaller than *Re*, which is based on U_∞. As U_∞ or *Re* increases, the Reynolds number based on the gap flow velocity may exceed a critical value. The small closed wake then ceases to exist. Meanwhile, periodic vortex shedding starts, forming one narrow vortex street, coexisting with the wide street. The narrow and wide street are associated with a dominant frequency of about 0.3 and 0.09, respectively. Apparently, the smaller the gap between the cylinders, the stronger is the near-wall

effect. Consequently, transition from the one-street to the two-street flow structure occurs at a larger *Re*. The present observation and interpretation help clarify the seemingly inconsistent reports of the dominant frequencies for $1.25 \leq T/d \leq 1.5$ in the literature.

3 For $T/d > 1.6$ but < 2.0, the near-wall effect could be negligible, and therefore the one-street flow structure is absent. The flow consists of one narrow and one wide street throughout the *Re* range investigated. At $T/d > 2.0$, two predominantly anti-phase streets occur (Figure 5-10d; e.g., Zhou *et al.* 2001).

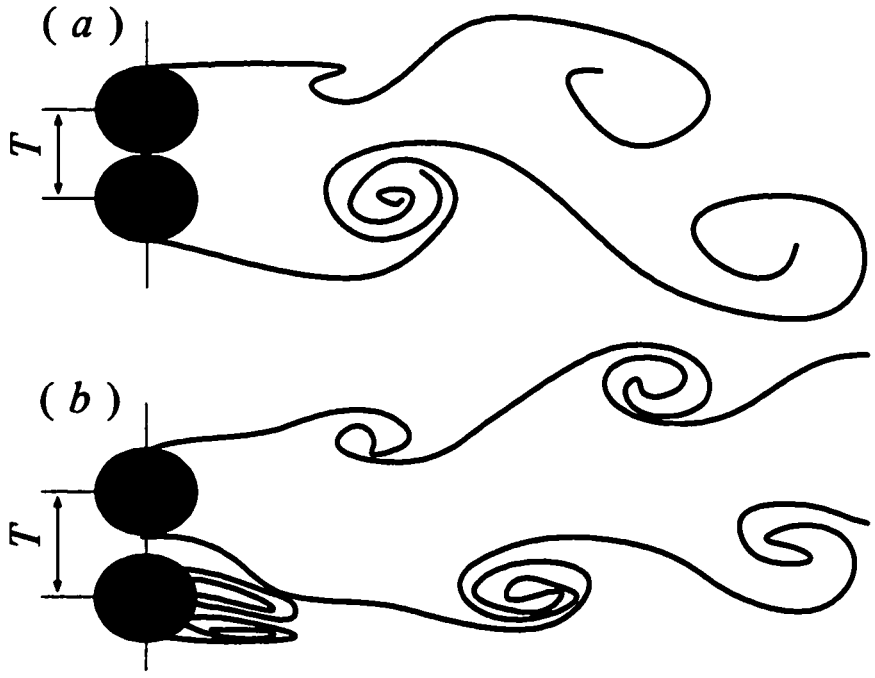

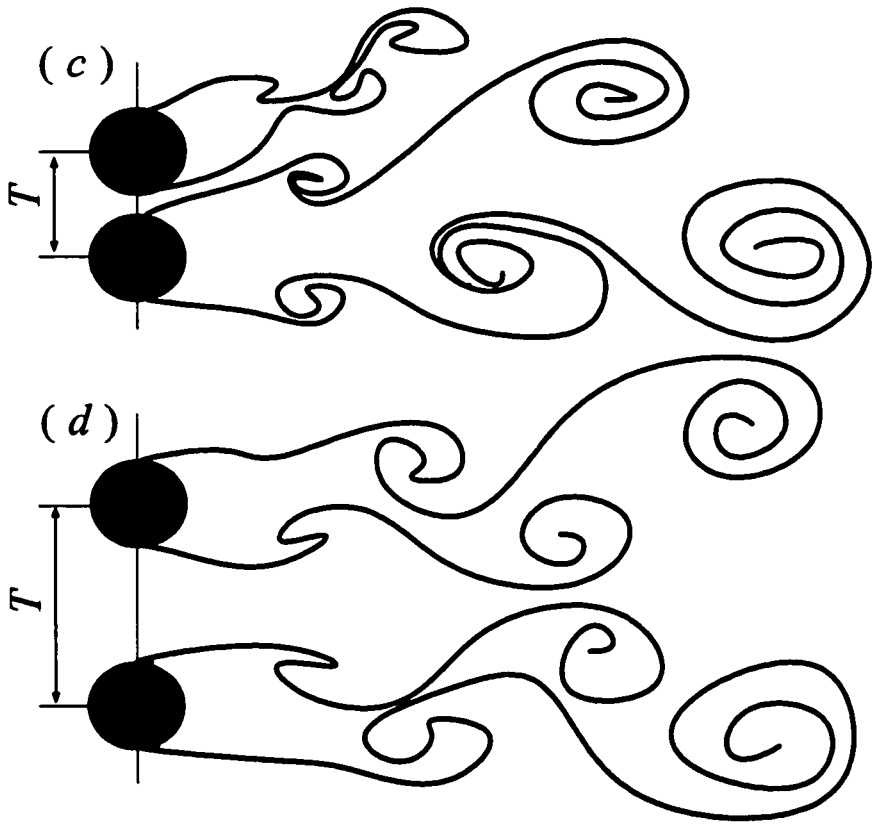

Figure 5-10 Summary sketches of typical flow structures behind two side-by-side cylinders. (a) $T/d < 1.25$; (b) $T/d = 1.25 \sim 1.6$: one-street flow structure at relatively low *Re*; (c) $1.6 < T/d < 2$ and $T/d = 1.25 \sim 1.6$: two-street flow structure at relatively high *Re*; (d) $T/d > 2.0$ (Zhou *et al.* 2001).

CHAPTER 6

A SIMPLIFIED AND APPROXIMATE SOLUTION ON AN ELASTIC BEAM IN A CROSS FLOW

6.1 Introduction

In a simple flow-induced vibration problem, where the structure is exposed to a uniform cross flow, the complexity depends to a very large extent on the properties of the structure. For example, if the structural stiffness is exceedingly large, the structure can be considered to be relatively rigid and fluid-structure interactions do not play a significant role. Of course, the structure could be subject to external excitations. When this happens, fluid-structure interactions will play an important role in the subsequent vibrations of the structure and the associated fluid damping and natural frequencies of the fluid-structure system. A lock-in phenomenon will occur when the frequency of the imposed force approaches the shedding frequency of the structure. On the other hand, if the structural stiffness is large but finite, the structure will vibrate under the vortex-induced excitation forces. Thus, the structure is said to be freely vibrating under the action of the flow-induced force. Resonance will occur when the frequency of the

vortex-induced force approaches the natural frequency of the fluid-structure system (Blevins, 1994). This simple free vibration problem is very complicated. There have been a number of investigations using different approaches as stated in Section 1.2.4. In all these approaches, the structural displacement is either assumed small compared to its hydraulic diameter or the mean displacement of the structure in the drag direction is assumed to have little effect on the structural dynamics in the lift direction. In other words, the coupling between the lift and drag direction is considered to be insignificant. If the mean displacement in the drag direction is large, the structure will develop a curvature; thus giving rise to an axial force that might not be negligible. It is known that axial force changes the rigidity of a beam (Weaver *et al.* 1989). For example, a tensile axial force will increase the beam rigidity whereas a compressive axial force may reduce it. The natural frequencies of the beam will increase or decrease accordingly. For the simple flow-induced vibration problem discussed here, a steady drag force is assumed to act on the structure. Therefore, a bending deformation in the streamwise direction will occur. This steady drag is small or large depending on the fluid density, the flow velocity and the hydraulic diameter of the structure. For a given structure and a fixed velocity, the drag is small for airflow but large for liquid because the liquid density is typically two orders larger than air. A large drag will give rise to a significant mean deformation. In turn, the relatively large axial curvature will give rise to a substantial tensile axial force when the structure is fixed-supported at both ends. This axial force effect influences the structural vibrations and their characteristics, such as the natural frequencies of the fluid-structure system and the vibration amplitude.

So far, it proves to be a challenge to analytically solve the equations of motion governing the fluid and structural response in the simple flow-induced vibration problem. The analytical solution for the structural response alone assuming a known force field has yet to be found, not to mention the combined solution of the fluid and structural dynamics. One of the difficulties in solving the structural equations of motion alone could be attributed to the nonlinear nature of the partial differential equations, which are coupled because of the coupling between the drag and lift.

In this chapter, a simplified and approximate analysis toward describing the self-excited vibration of an elastic beam will be carried out. This approach will be based on some engineering approximations that will provide an initial estimate of what the cylinder vibration is. The structural dynamic equations are derived based on Hamilton's principle and an assumed vortex-excited force given by a mean and a periodic component. Experimental measurements of the Strouhal number and force coefficients are used to determine the parameters introduced in the force model. Simplifying assumptions are made as long as they do not compromise the fundamental physics of the flow-induced vibration.

For practical flow-induced vibration problems, the mean structural displacement in the drag direction could be large. Therefore, it is also important to consider the spanwise curvature effect on the resultant structural response. In view of this, the present approach takes the spanwise curvature effect into account and the equations of motion are solved with this effect included.

6.2 Theoretical Formulation

In order to derive the equations of motion for a structure in a cross flow, the strain energy, the kinetic energy and the work done by the external forces have to be formulated. The external force in the present context includes the vortex-excited force and the axial force. The derivation is carried out assuming the cross section of the structure to have arbitrary geometry. The work done by the external forces is deduced first. It is then followed by the derivation of the strain energy and finally the kinetic energy. The equations of motion are derived using Hamilton's principle and the formulation is completed by specifying the vortex-excited force.

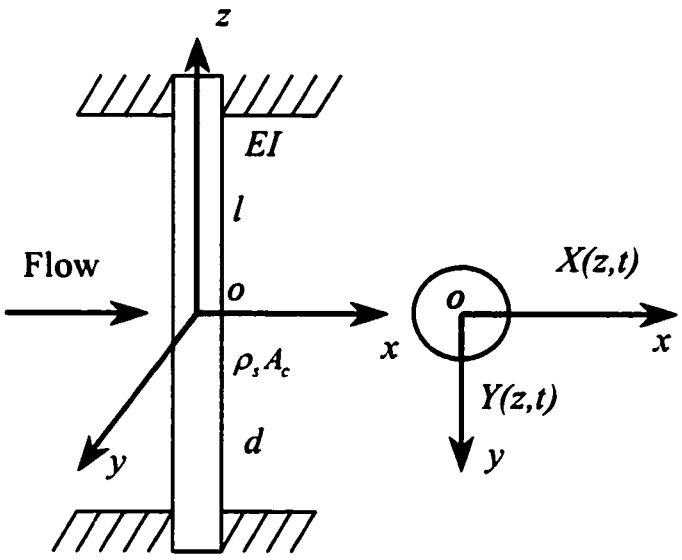

Figure 6-1 A schematic of a fixed-supported cylinder in a cross flow.

Consider a cylinder in a uniform cross flow fixed-supported at both ends. The cylinder is subject to the action of mean and fluctuating forces along the x (drag) and y (lift) direction (Figure 6-1). Consequently, a coupled bending-bending motion along x and y will result. If the cylinder surface is assumed to be smooth and the structural deformation to be small, then the structural displacements in the x, y and z directions can be written as

$$\begin{aligned} X &= X(z,t) \\ Y &= Y(z,t) \\ Z &= Z_1(x',z,t) + Z_2(y',z,t), \qquad x', y' \in [-d/2,\, d/2], \end{aligned} \tag{6-1}$$

where $Z_1 = -x'\partial X/\partial z$, $Z_2 = -y'\partial Y/\partial z$, x' and y' are coordinates in the x and y direction, respectively. Equation (6-1) needs justification. If a planar cross-section at location z remains plane even after bending, the rotation about the x- and y-axes are given by $\partial X/\partial z$ and $\partial Y/\partial z$, respectively (Figure 6-2). For a slender cylinder, whose aspect ratio is large, the rotational slope is generally small. Hence, the following assumptions are valid: $|\partial X/\partial z| << 1$, $|\partial Y/\partial z| << 1$ and $|Z| = O(X^2, Y^2)$. The two inequalities require the bending deformation to be sufficiently small, say less than 1 radian (Edward & Robert, 1968; Stronge & Yu, 1993; Chang *et al.* 1997), so that the cylinder length is approximately constant and the deformation occurs within the limit of elasticity, implying a linear relation between strain and displacement. The assumption $|Z| = O(X^2, Y^2)$ requires the longitudinal velocity to be small compared to the other two velocity components. Thus, its contribution to the kinetic energy is negligible. Once these

conditions are satisfied, the structural displacements in the x, y and z directions are given by (6-1).

For a cylinder element vibrating in the x-z plane, the tensile axial force N acting on a cross-section can be derived (Figure 6-3). The change in the elemental length is given by (Rao, 1992)

$$\Delta ds' = ds' - dz = \left[\sqrt{1-\left(\partial X(z,t)/\partial z\right)^2} - 1\right] dz \approx \frac{1}{2}\left(\frac{\partial X(z,t)}{\partial z}\right)^2 dz . \tag{6-2}$$

Similarly, the change in the elemental length in the (y, z)-plane is given by

$$\Delta ds'' = ds'' - dz = \left[\sqrt{1-\left(\partial Y(z,t)/\partial z\right)^2} - 1\right] dz \approx \frac{1}{2}\left(\frac{\partial Y(z,t)}{\partial z}\right)^2 dz . \tag{6-3}$$

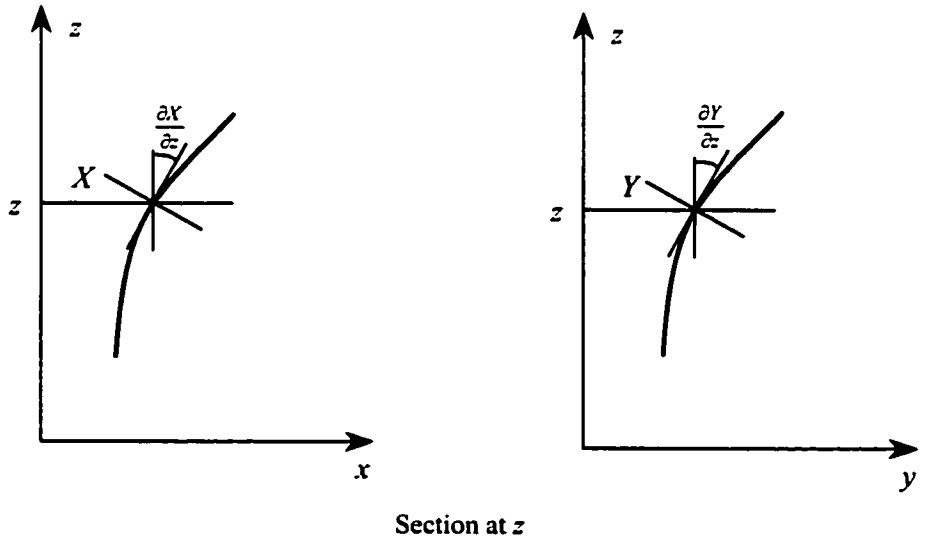

Figure 6-2 Rotation of the cylinder in the x-z and y-z plane.

The total change in the elemental length can be approximated by $\Delta ds = \Delta ds' + \Delta ds''$. Therefore, the work done by the applied loading along the x and y direction, q_x and q_y, respectively, and the axial force N may be calculated as

$$W = \int_{-l/2}^{l/2} q_x X(z,t)dz + \int_{-l/2}^{l/2} q_y Y(z,t)dz + \frac{1}{2}\int_{-l/2}^{l/2} N\left[\left(\frac{\partial X(z,t)}{\partial z}\right)^2 + \left(\frac{\partial Y(z,t)}{\partial z}\right)^2\right]dz, \quad (6\text{-}4)$$

The shear forces can be neglected when the cylinder aspect ratio is large. Therefore, there remain three components of strain in the x, y and z directions. Under the condition of small deformation, they can be written as

$$\begin{Bmatrix} \varepsilon_{xx} \\ \varepsilon_{yy} \\ \varepsilon_{zz} \end{Bmatrix} = \begin{Bmatrix} \partial X/\partial z \\ \partial Y/\partial z \\ \partial Z/\partial z \end{Bmatrix}. \quad (6\text{-}5)$$

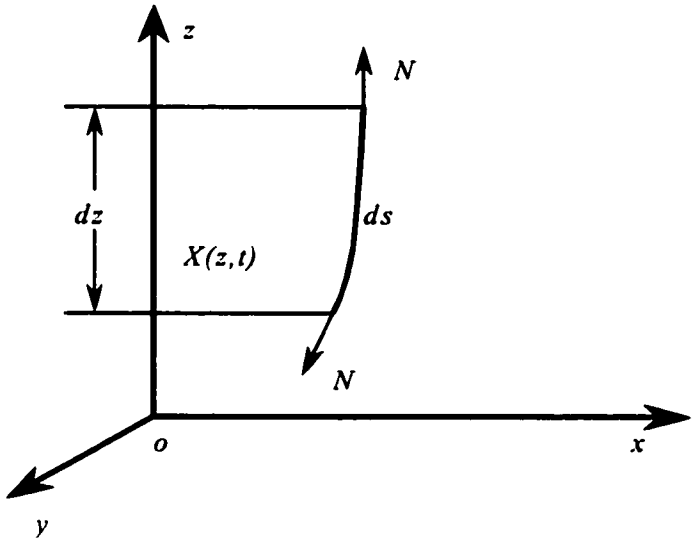

Figure 6-3 An illustration of the axial force resulting from cylinder curvature.

The stress components in the x, y and z directions can be calculated from (6-5) using Hooke's law. For an isotropic material, the stress can be expressed as

$$\begin{Bmatrix} \sigma_{xx} \\ \sigma_{yy} \\ \sigma_{zz} \end{Bmatrix} = E \begin{Bmatrix} \varepsilon_{xx} \\ \varepsilon_{yy} \\ \varepsilon_{zz} \end{Bmatrix}, \tag{6-6}$$

where E is Young's modulus. If Λ denotes the volume of the cylinder, the strain energy is given by

$$\begin{aligned} U &= \frac{1}{2}\iiint_{\Lambda} \begin{bmatrix} \sigma_{xx} & \sigma_{yy} & \sigma_{zz} \end{bmatrix} \begin{bmatrix} \varepsilon_{xx} & \varepsilon_{yy} & \varepsilon_{zz} \end{bmatrix}^T d\Lambda \\ &= \frac{1}{2}\int_{-l/2}^{l/2} \left[\iint_{A_c} \left(Ex'^2 \left(\frac{\partial^2 X(z,t)}{\partial z^2} \right)^2 + 2Ex'y' \frac{\partial^2 X(z,t)}{\partial z^2} \frac{\partial^2 Y(z,t)}{\partial z^2} + Ey'^2 \left(\frac{\partial^2 Y(z,t)}{\partial z^2} \right)^2 \right) dA_c \right] dz \quad . \end{aligned} \tag{6-7}$$

Finally, since there is no cylinder rotation and the velocity in the z direction is very small and can be neglected, the kinetic energy is derived by neglecting their contributions. The result is given by

$$T = \frac{1}{2}\int_{-l/2}^{l/2} \rho_s A_c \left[\left(\frac{\partial X(z,t)}{\partial t} \right)^2 + \left(\frac{\partial Y(z,t)}{\partial t} \right)^2 \right] dz \, . \tag{6-8}$$

Based on Hamilton's principle (Harrison & Nettleton, 1997), the following equality can be established,

$$\delta \int_{t_1}^{t_2} (U - T - W) dt = 0, \tag{6-9}$$

where time t_1 and t_2 are arbitrary. Expanding (6-9) and taking into account structural damping and the added mass of the cylinder, the dynamic equations of motion for the flow-excited structural vibrations are

$$EI_{yy}\frac{\partial^4 Y(z,t)}{\partial z^4} - N\frac{\partial^2 Y(z,t)}{\partial z^2} + c_s\frac{\partial Y(z,t)}{\partial t} + (c_m+1)\rho_s A_c\frac{\partial^2 Y(z,t)}{\partial t^2} + EI_{yx}\frac{\partial^4 X(z,t)}{\partial z^4} = q_y \tag{6-10a}$$

for the y-direction and

$$EI_{xx}\frac{\partial^4 X(z,t)}{\partial z^4} - N\frac{\partial^2 X(z,t)}{\partial z^2} + c_s\frac{\partial X(z,t)}{\partial t} + (c_m+1)\rho_s A_c\frac{\partial^2 X(z,t)}{\partial t^2} + EI_{xy}\frac{\partial^4 Y(z,t)}{\partial z^4} = q_x \tag{6-10b}$$

for the x-direction. The product of inertia is given by $I_{xy} = I_{yx} = \int_{A_c} x'y'dA_c$, the moments of inertia are $I_{yy} = \int_{A_c} x'^2 dA_c$ and $I_{xx} = \int_{A_c} y'^2 dA_c$. It should be noted that N in (6-10) is positive for a tensile axial force.

Equations (6-10) include the effects of axial force, which has not been considered in previous studies (e.g., Chen, 1987). Furthermore, the description of coupled bending vibration between the drag and lift directions is also included in (6-10). Therefore, in principle, (6-10) is valid for a cylinder with arbitrary cross-section and with an arbitrary angle of attack. However, the analytical solution of (6-10) is difficult to obtain. Therefore, for simplicity, a circular cylinder whose cross section is characterized by symmetry about the centroid is considered here. Under this simplification, the product of inertia is zero, i.e., $I_{xy} = I_{yx} = 0$, and the moment of inertia is simplified to $I_{xx} = I_{yy} = I$.

Correspondingly, the boundary conditions for a cylinder fixed-supported at both ends are given by

$$X(-\frac{l}{2}) = X(\frac{l}{2}) = 0 \quad \textit{and} \quad \left.\frac{\partial X}{\partial z}\right|_{z=-l/2} = \left.\frac{\partial X}{\partial z}\right|_{z=l/2} = 0, \tag{6-10c}$$

in the x or drag direction and

$$Y(-\frac{l}{2}) = Y(\frac{l}{2}) = 0 \quad \textit{and} \quad \left.\frac{\partial Y}{\partial z}\right|_{z=-l/2} = \left.\frac{\partial Y}{\partial z}\right|_{z=l/2} = 0, \tag{6-10d}$$

in the y or lift direction.

The flow excitation forces q_x and q_y are largely dependent on the flow around the cylinder, which is governed by the Navier-Stokes equations,

$$\nabla \cdot \vec{V} = 0 , \tag{6-11a}$$

$$\frac{D\vec{V}}{Dt} = -\frac{1}{\rho}\nabla p + \nu\nabla^2 \vec{V} . \tag{6-11b}$$

Here, D/Dt is the material derivative, t is time, $\vec{V}$ is the instantaneous velocity vector and p is the static pressure. Equations (6-10) - (6-11) are the governing equations for the fluid-cylinder system.

In order to solve (6-10), the flow excitation forces need to be specified. The excitation forces in (6-10) can be decomposed into three components, $q_k = \bar{q}_k + \tilde{q}_k + \dot{q}_k$, where the over bar, tilde and prime denote the time-mean, periodical and random components of the fluid force, respectively. The subscript k stands for either x or y.

Assuming the random component, q_k', to be negligible in view of the fact that vortex excitation is dominant, the other two components could be represented by

$$\bar{q}_x = \frac{1}{2}\rho U_\infty d[C_D(U_{rel} - \frac{U_{rel}}{U_\infty}\dot{X}) + C_L\frac{U_{rel}}{U_\infty}\dot{Y}], \tag{6-12a}$$

$$\tilde{q}_x = \frac{1}{2}\rho U_\infty^2 dC_D' \sin\Omega_D t, \tag{6-12b}$$

$$\bar{q}_y = \frac{1}{2}\rho U_\infty d[C_L(U_{rel} - \frac{U_{rel}}{U_\infty}\dot{X}) - C_D\frac{U_{rel}}{U_\infty}\dot{Y}], \tag{6-13a}$$

$$\tilde{q}_y = \frac{1}{2}\rho U_\infty^2 dC_L' \sin\Omega_L t. \tag{6-13b}$$

In (6-12) and (6-13), the dot over X and Y denotes $\partial/\partial t$. In general, $U_\infty >> \dot{X}(z,t)$ or $\dot{Y}(z,t)$. For example, the present experimental data (Section 6.5) shows that when the third-mode resonance occurs at $U_r \approx 26.9$ ($U_\infty \approx 16$ m/sec), the vibration amplitude reaches a maximum. Even then, $\dot{X}$ *or* $\dot{Y}$ is estimated to be in the order of 0.2 m/sec, about $0.012U_\infty$. Consequently, U_{rel} can be approximated by

$$U_{rel} = \sqrt{\dot{Y}^2 + (U_\infty - \dot{X})^2} \approx U_\infty - \dot{X} \text{ and } U_{rel}/U_\infty \approx 1.$$

For an isolated cylinder, the mean lift coefficient C_L = 0. With these simplifications, (6-10) is reduced to

$$EIX_{,zzzz} - NX_{,zz} + c_x\dot{X} + M\ddot{X} = \frac{1}{2}\rho dC_D U_\infty^2 + \tilde{q}_x, \tag{6-14a}$$

$$EIY_{,zzzz} - NY_{,zz} + c_y\dot{Y} + M\ddot{Y} = \tilde{q}_y, \tag{6-14b}$$

where the subscript ',z' denotes $\partial/\partial z$, $M=(c_m+1)\rho_s A_c$ is the sum of the added mass and the cylinder mass per unit length, and c_x and c_y denote the modal damping coefficients of the fluid-cylinder system. These coefficients are given by

$$c_x = c_s + \rho d C_D U_\infty, \tag{6-15a}$$

$$c_y = c_s + \rho d C_D U_\infty / 2, \tag{6-15b}$$

in the x and y direction, respectively. The second term on the right hand side of (6-15) comes from the mean fluid excitation force (6-12a) and (6-13a), respectively. It has the same effect as damping in the governing equation (6-10). Therefore, it is called the drag-induced fluid damping. Obviously, this drag-induced damping is insufficient to completely account for fluid damping, which is very complicated and could also depend on the motion of the cylinder. The effect of fluid damping on vibration will be further discussed in Section 6.5.

The steady fluid load on the right hand side of (6-14a), namely $\rho d C_D U_\infty^2/2$, causes a steady bending deformation when U_∞ is not changing. It does not contribute directly to the structural vibration response. Therefore, it could be neglected from the vibration response analysis. The axial force N in (6-14) may be decomposed into

$$N = N_{si} + N_{vi} + N_{ex}, \tag{6-16}$$

where N_{si} is caused by the mean drag force $\rho d C_D U_\infty^2/2$. It is the drag-induced axial force. If this force is assumed to distribute uniformly along the span of the cylinder, then the maximum deflection of the cylinder in the plane which includes $\rho d C_D U_\infty^2/2$ can be calculated based on mechanics of materials (Roy, 1996). Approximating the deflected

cylinder by a curve, the axial deformation can be estimated. The tensile stress due to this axial deformation can be calculated by means of Hooke's law. Finally, the drag-induced axial force can be written as $N_{si} = 2EA_c q^2 l^6 /(384EI)^2$. The second term, N_{vi}, on the right hand side of (6-16) is the vibration-induced axial force. It is caused by the axial deformation that is the result of cylinder vibration. This term changes with time and is zero when the vibration vanishes. It is given by

$$N_{vi} = (EA_c / 2l) \int_{-l/2}^{l/2} (\partial X / \partial z)^2 dz .$$

This vibration-induced axial force should have the same period as the vibration in the drag direction. When the vibration amplitude of the cylinder is large, the amplitude of this component should be significant. However, N_{vi} is not easy to calculate because the displacement response must be known first. Therefore, it is neglected in the example given in Section 6.5 for simplicity when only low order vibrations are concerned. The last term on the right hand side of Eq. (6-16), N_{ex}, is the external axial loading. Since the problem under consideration is a free vibration problem, there is no external loading on the cylinder. It is worth pointing out that the drag-induced axial loading is a tensile force because the cylinder is stretched under the effect of the steady drag.

Note that C_D, C_D', C_L' and C_m are time-dependent. It is still pretty difficult to solve the equation (6-14) analytically. To analytically calculate the displacement/strain response from Eq.(6-14) at resonance, these coefficients were replaced by their RMS (root mean square) values, respectively. With these simplifications, Equation (6-14) reduces to two independent and linear partial differential equations.

6.3 Cylinder Dynamics

The solution to Eq. (6-14) can be given in three different parts, i.e., the solution for the natural frequencies of the fluid-cylinder system, the solution for the displacements X and Y in the x and y directions, respectively, and the solution for the strains. These solutions are outlined below.

6.3.1 Natural frequencies of fluid-cylinder system

Taking the right hand side of Eq. (6-14a, b) to be zero, two homogeneous partial differential equations are obtained. They can then be solved to yield the frequency equations in the x and y directions, respectively. Assuming the solution to take the harmonic form,

$$X(z,t) = A_x(z)e^{j\omega_x t} \text{ and } Y(z,t) = A_y(z)e^{j\omega_y t}, \tag{17a, b}$$

where ω_x and ω_y are the circular frequencies and $j^2 = -1$, and substituting (6-17) into the two homogenous partial differential equations of (6-14), the frequency equation (6-18) is obtained after some tedious algebra,

$$\cosh\beta_{k2}\cos\beta_{k1} + \frac{1}{2}\left(\frac{\beta_{k1}}{\beta_{k2}} - \frac{\beta_{k2}}{\beta_{k1}}\right)\sinh\beta_{k2}\sin\beta_{k1} - 1 = 0. \tag{6-18}$$

In the above equation,

$$\beta_{ki} = \left(\left\{\sqrt{b^2 - 4ac} + (-1)^{i+1}b\right\}/2a\right)^{1/2}, \tag{6-19}$$

where $a = EI$, $b = N$, $c = jc_k\omega_k - M\omega_k^2$, $k = x$ or y, and $i = 1, 2$. Equation (6-18) is a transcendental and complex equation. It is therefore difficult to obtain an analytical

solution for the general case. In general, a solution for the system natural frequencies could be obtained by resorting to approximate analytical method (Weaver *et al.* 1989) or numerical methods. It is evident from (6-18) that N, besides M, EI and c, influences the determination of the natural frequencies of the fluid-structure system. As indicated in (6-15), damping (including fluid damping) in the drag direction is not the same as in the lift direction. Thus, the natural frequencies may differ, though slightly, between the drag and lift direction. For a circular cylinder in an air cross flow and anticipating the results of Section 6.5, the axial force has a very small effect on the lower order natural frequencies. Therefore, the frequency equation can be simplified and an approximate analytical solution to the equation can be deduced. This is illustrated below.

Assuming the effect of axial force is negligible, i.e., $N = 0$, we have from (6-19)

$$r_1 = \beta_{x1} = \beta_{x2} = \sqrt[4]{-(Ms^2 + c_x s)/EI}$$

$$\cos r_1 l \cosh r_1 l = 1, \tag{6-20}$$

Adopting a method to solve (6-20) similar to that used by Weaver *et al.* (1989), its roots can be approximated with satisfactory accuracy by

$$r_1 l \approx \frac{2n+1}{2}\pi \qquad n = 1, 2, \ldots\ldots \quad . \tag{6-21}$$

If weak damping is assumed, substituting (6-21) into (6-17a) yields

$$X(z,t) = A_x(z)e^{-c_x/2M} \cdot (C_1 \sin(\sqrt{4MEI((2n+1)\pi/2l)^4 - c_x^2}/2M)t + C_2 \cos(\sqrt{4MEI((2n+1)\pi/2l)^4 - c_x^2}/2M)t) \quad , \tag{6-22}$$

where C_1 and C_2 are constants to be determined from the initial condition. Evidently, the natural frequencies are given by

$$f_x^{(n)} = \frac{\omega_x^{(n)}}{2\pi} = \frac{\sqrt{4MEI((2n+1)\pi/2l)^4 - c_x^2}}{4\pi M}, \tag{6-23}$$

where n denotes the *nth* mode of vibration.

If $c_x = 0$, (6-23) is reduced to $f_0^{(n)} = [(2n+1)/3]^2 f_0^{(1)}$, where $f_0^{(1)} = (9\pi/8)\sqrt{EI/Ml^4}$ is the first-mode natural frequency of the cylinder. Subsequently, (6-23) can be rewritten as

$$f_x^{(n)} = f_0^{(n)}\sqrt{1-(\zeta_{x,e}^{(n)})^2}, \qquad n = 1, 2, \ldots \ , \tag{6-24}$$

where the modal damping ratio is given by

$$\zeta_{x,e}^{(n)} = \frac{c_x}{2M\omega_0^{(n)}} = \frac{c_x}{4\pi M f_0^{(n)}} \qquad n = 1, 2, \ldots \ . \tag{6-25}$$

Substituting (6-15a) into (6-25) gives $\zeta_{x,e}^{(n)} = \zeta_s^{(n)} + \zeta_{x,f}^{(n)}$, where

$$\zeta_s^{(n)} = c_s / 4\pi M f_0^{(n)} \tag{6-26a}$$

is the structural damping ratio and

$$\zeta_{x,f}^{(n)} = \frac{9C_D}{4\pi(2n+1)^2 M^*} U_r \ , \tag{6-26b}$$

is the drag-induced inline fluid damping ratio. The mass ratio M^* in (6-26) is defined as $M/\rho d^2$.

Similarly, the cross-flow natural frequencies of the system can be shown to be

$$f_y^{(n)} = f_0^{(n)}\sqrt{1-(\zeta_{y,e}^{(n)})^2} \ . \tag{6-27}$$

The cross-flow modal damping ratio $\zeta_{y,e}^{(n)}$ is given by $\zeta_{y,e}^{(n)} = \zeta_s^{(n)} + \zeta_{y,f}^{(n)}$ where,

$$\zeta_{y,f}^{(n)} = \frac{9C_D}{8\pi(2n+1)^2 M^*} U_r \,, \tag{6-28}$$

is the drag-induced cross-flow fluid damping ratio. The drag-induced fluid damping ratios (6-26) and (6-28) deduced here are consistent with those given in Chen (1987).

6.3.2 An approximate solution for the displacements

Since the right hand side of (6-14) is assumed known, the fluid excitation force can be considered as an external force to (6-14). Thus, the structural vibration can be regarded as forced vibration under a specified fluid load. With this understanding, there is no need to consider the initial conditions in solving (6-14), provided that only the steady-state vibration of the cylinder is of interest. The right hand side of (6-14a, b) can then be rewritten using Euler's triangle formula as

$$j\left(e^{-j\Omega_D t} - e^{j\Omega_D t}\right)\psi_x \quad \text{and} \quad j\left(e^{-j\Omega_L t} - e^{j\Omega_L t}\right)\psi_y \quad . \tag{6-29a, b}$$

Here, $\psi_x = \rho U_\infty^2 d C_D^{'}/4$ and $\psi_y = \rho U_\infty^2 d C_L^{'}/4$. With this simplification, (6-14) can be reduced to a set of linear partial differential equations and the superposition principle is applicable. In order to meet the initial conditions, the solution is assumed to be harmonic. Therefore, in the drag direction, the displacement solution takes the form

$$X(z,t) = X_1(z,t) + X_2(z,t)\,, \tag{6-30a}$$

where $X_1(z,t) = A_{x1}(z)e^{j\Omega_D t}$ and $X_2(z,t) = A_{x2}(z)e^{-j\Omega_D t}$. Similarly, the displacement solution in the lift direction takes the form

$$Y(z,t) = Y_1(z,t) + Y_2(z,t)\,, \tag{6-30b}$$

where $Y_1(z,t) = A_{y1}(z)e^{j\Omega_L t}$ and $Y_2(z,t) = A_{y2}(z)e^{-j\Omega_L t}$.

Substituting (6-30) into (6-14) yields a set of ordinary differential equations that can be solved together with the boundary conditions (6-11). Thus formulated, the displacement response can be solved to yield $A_{x2}(z) = -A_{x1}(z)$ and the following expression for A_{x1},

$$A_{x1}(z) = \frac{\left[\beta_{x2}\left(\cosh\frac{\beta_{x1}l}{2} - \cosh\beta_{x1}z\right)\sin\frac{\beta_{x2}l}{2} + \beta_{x1}\left(\cos\frac{\beta_{x2}l}{2} - \cos\beta_{x2}z\right)\sinh\frac{\beta_{x1}l}{2}\right]\psi_x j}{a\beta_{x1}^2\beta_{x2}^2\left(\beta_{x2}\cosh\frac{\beta_{x1}l}{2}\sin\frac{\beta_{x2}l}{2} + \beta_{x1}\cos\frac{\beta_{x2}l}{2}\sinh\frac{\beta_{x1}l}{2}\right)} \tag{6-31}$$

A similar manipulation gives $A_{y2}(z) = -A_{y1}(z)$ and the expression for A_{y1} is

$$A_{y1}(z) = \frac{\left[\beta_{y2}\left(\cosh\frac{\beta_{y1}l}{2} - \cosh\beta_{y1}z\right)\sin\frac{\beta_{y2}l}{2} + \beta_{y1}\left(\cos\frac{\beta_{y2}l}{2} - \cos\beta_{y2}z\right)\sinh\frac{\beta_{y1}l}{2}\right]\psi_y i}{a\beta_{y1}^2\beta_{y2}^2\left(\beta_{y2}\cosh\frac{\beta_{y1}l}{2}\sin\frac{\beta_{y2}l}{2} + \beta_{y1}\cos\frac{\beta_{y2}l}{2}\sinh\frac{\beta_{y1}l}{2}\right)}. \tag{6-32}$$

Using Euler's triangle formula, the displacement response can be simplified to give

$$X(z,t) = 2jA_{x1}(z)\sin\Omega_D t, \tag{6-33a}$$

$$Y(z,t) = 2jA_{y1}(z)\sin\Omega_L t. \tag{6-33b}$$

These are complex equations and the magnitude of X and Y is given by their modules value. The correlation of X and Y is zero since the form of the solution is assumed to be harmonic. In other words, the independence of X and Y follows from the linear assumption.

6.3.3 Solution for the dynamic strains

Strain response along the z-axis can be calculated based on the displacement response. The relationship between strain and axial displacement is approximately linear under the small deformation assumption. In other words, we have

$$\varepsilon_{zz}(x', y', z, t) = \frac{\partial Z}{\partial z} + O(Z^2) \quad .$$

For a point at the mid-span of the cylinder, the strain along the forward stagnation line due to the drag can be written as

$$\varepsilon_X = \frac{d}{2}\left(\frac{\partial^2 X}{\partial z^2}\right)_{z=0} \quad , \tag{6-34a}$$

and the strain at $\pi/2$ away from the forward stagnation line due to the lift is given by

$$\varepsilon_Y = \frac{d}{2}\left(\frac{\partial^2 Y}{\partial z^2}\right)_{z=0} \quad . \tag{6-34b}$$

Substituting (6-33) into (6-34), the exact form of the strain at these two points is

$$\varepsilon_X = jd\sin\Omega_D t\left(\frac{\partial^2 A_{x1}}{\partial z^2}\right)_{z=0} \quad , \tag{6-35a}$$

$$\varepsilon_Y = jd\sin\Omega_L t\left(\frac{\partial^2 A_{y1}}{\partial z^2}\right)_{z=0} \quad . \tag{6-35b}$$

Obviously, ε_X and ε_Y are also complex and independent of each other for a circular cylinder.

It should be pointed out that (6-35) is invalid for large deformation. When this happens, (6-5) is also not valid and the strain-displacement relation of Green (Nayfeh &

Mook, 1995) could be used to deduce

$$\varepsilon_{zz}(x', y', z, t) = \frac{\partial Z}{\partial z} - \left(\frac{\partial Z}{\partial z}\right)^2 + \frac{1}{2}\left(\frac{\partial X}{\partial z}\right)^2 + \frac{1}{2}\left(\frac{\partial Y}{\partial z}\right)^2 + O(Z^3) \quad . \tag{6-36}$$

As a result, (6-10) will take a more complex form and the difficulty of solving these equations will be much greater. The analytical approach to solve for strain will be very tedious and complex. Therefore, it is advisable to use Mathematica® 4 software to solve for the strains.

6.4 A Simple Experiment

Experimental data on the free vibration of a single cylinder in a cross flow is scarce, especially displacement measurements along the span of the cylinder. Recently, Zhou *et al.* (1999) measured the dynamic strains on a single cylinder using an optical fibre Bragg grating sensor (Jin *et al.* 2000) over a fairly wide range of reduced velocity, U_r. On the other hand, So *et al.* (2000) studied the dynamic behavior of the cylinder by measuring the root mean square (rms) transverse displacement, Y_{rms}, along the span of the cylinder using a laser vibrometer. Their measurements were carried out for several cylinders with different structural properties and over a range of Reynolds numbers, *Re*. In these two studies, the emphasis was on the dynamical behavior in the lift or transverse (y) direction. Little or no information could be found in the streamwise or drag (x) direction. Subsequently, Zhang *et al.* (2000) carried out an experiment similar to that conducted by Zhou *et al.* (1999) to measure the dynamic strain along the x and y directions simultaneously. Their aim was to study the behavior of fluid damping and its relation

with U_r. Again, the range of U_r covered was quite wide and complemented well the former measurements by Zhou *et al.* (1999) and So *et al.* (2000). Therefore, these measurements could be used to validate the theoretical analysis of the dynamical behavior of the free vibration of a single cylinder in a cross flow. However, one piece of data that is not available from these experiments is the variation of Y_{rms} with U_r. The validation would not have been complete if this crucial behavior could not be verified. In view of this, a simple experiment to measure the variation of Y_{rms} with U_r was carried out.

The experiment was carried out in the same wind tunnel used in the study of So *et al.* (2000). Details of the wind tunnel and the experimental setup are available from their study. Since the spanwise distribution of Y_{rms} measured by So *et al.* (2000) for two different U_r was performed using an acrylic cylinder, the present experiment was also conducted using an acrylic cylinder. These cylinders are stock items; therefore, their structural properties differ slightly. The cylinder used for this experiment has a length of 350mm, an outer diameter 6mm, an inner diameter 4mm, EI = 0.2476 Nm^2, and a mass per unit length of 0.018 kg/m. The cylinder was mounted in the mid-plane of the test section and 20 cm downstream of the exit plane of the contraction. A fixed support was provided at both ends so that the deflection at the support was essentially zero. Thus configured, the natural frequency of the stationary cylinder was found to be 106 Hz, slightly different from that used in the experiment of So *et al.* (2000). The freestream velocity, U_∞, can be varied over a rather wide range, enough to give an U_r of 0 to 40. Over this range of U_∞, the free-stream turbulence was measured at about 0.2%. A Polytec Series 3000 Dual Beam Laser Vibrometer was used to measure the Y time series

at the mid-span of the cylinder over a range of U_r. No measurements along the drag direction were attempted. This was due to the difficulty and relatively less accurate measurement as explained in Zhou *et al.* (1999). The result thus obtained is used to verify the prediction obtained from the present theoretical analysis.

All these experiments were carried out in a wind tunnel. Consequently, the range of mass ratio, M^*, covered in these experiments was very large, in the order of several hundred, and the maximum vibration amplitude normalized by the cylinder diameter d was only about 1%. Under these conditions, it is expected that the axial curvature of the cylinder will be small and its effect on cylinder vibration will be insignificant. Unfortunately, experimental data on vibration amplitude or dynamic strain where M^* is of the order of 1 to 10 is scarce. Therefore, the axial curvature effect on the cylinder dynamics cannot be verified by comparison with data. Instead, a parametric study of the effect of axial curvature on the cylinder dynamics over a range of M^* and U_r will be carried out.

6.5 Comparison with Measurements

The present calculations are compared with the data documented in So *et al.* (2000b) and Zhang *et al.* (2000), and the displacement measurements versus U_r obtained in the current experiment. In these studies, the cylinder used is essentially identical to the current cylinder. Therefore, the present calculation assumes a circular cylinder made of arcylic with properties identical to those specified in the different experiments. The calculations are compared with the measured Y_{rms}/d versus U_r in the current experiment,

the measured spanwise distribution of Y_{rms}/d for the resonance case given in So *et al.* (2000b), and the measured ε_{Xrms} and ε_{Yrms} versus U_r documented in Zhang *et al.* (2000). In order to perform calculations, several parameters associated with the assumed vortex-excited force model need to be specified. They are the mean drag coefficient, C_D, the rms force coefficients, $(C_D)_{rms}$ and $(C_L)_{rms}$, the frequencies Ω_D and Ω_L or the Strouhal number, St, and the fluid damping ratio. The C_D value for the cylinder in the Reynolds number (Re) range investigated is approximately 1.2. This value is consistent with the numerically calculated value reported in So et al. (2000a) in the range, $Re < 5000$. Therefore, the current calculations assume $C_D = 1.2$. The added mass is cited as $\rho\pi d^2/4$, consistent with Blevins (1994). As for St, a curve fit to the data documented in Chen (1987) is used. The $(C_D)_{rms}$ and $(C_L)_{rms}$ are determined by curve fitting the experimental data reported in Zdravkovich (1997). Finally, the modal damping ratio reported in Zhang *et al.* (2000) is used whenever it is required by the calculations.

6.5.1 Variation of Y_{rms}/d with U_r

The calculations are compared with the measured Y_{rms}/d versus U_r in the current experiment, The calculated and measured distributions of Y_{rms}/d at cylinder mid-span over a range of U_r are plotted in Figure 6-4. Two peaks are observed in this plot, one occurring at $U_r \approx 5$ and another at $U_r \approx 26.9$. Since the cylinder was fixed, varying U_r was achieved by changing U_∞. The freestream velocity corresponding to $U_r = 5$ was about $U_\infty = 3.0$ m/s. Therefore, the peak occurring at $U_r \approx 5$ corresponds to resonance with the natural frequency of the first mode of vibration of the cylinder. The peak at $U_r \approx$

26.9 can be interpreted as resonance with the third-mode natural frequency of the cylinder.

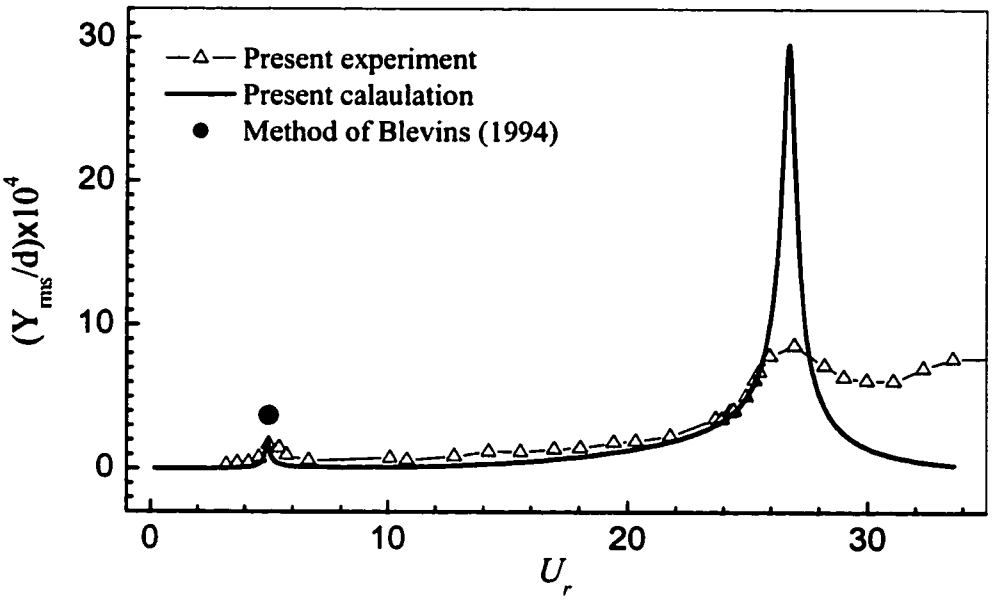

Figure 6-4 Distribution of Y_{rms}/d at cylinder mid-span with U_r for airflow.

The calculation gives the peak value at $U_r = 5$ with fair accuracy. Both present calculated and experimental values are approximately equal to 2.0. While the result estimated from Blevins model is about 3.7, almost doubling the measurement. By the contrast, the present calculated peak value at $U_r \approx 26.9$ is greatly over-predicted. Beyond $U_r \approx 26.9$, the calculations are greatly in error compared to the measured Y_{rms}/d. There are numerous reasons for the discrepancy noted at $U_r \approx 26.9$ and beyond. From the viewpoint of linear vibration theory, the calculated peak is higher than that of experiment

when the damping is underestimated. The effective fluid damping data in the present calculation is documented from Zhou *et al.*(2001) in which Zhou *et al.* adopted the linear ARAMX technique to identify the modal damping. Furthermore, the arising nonlinear effect may invalidate the linear formulation of the present analysis. In fact, it is quite surprising that the present analysis could give good agreement with measurements up to $U_r \approx 26.9$, where nonlinear effects are present.

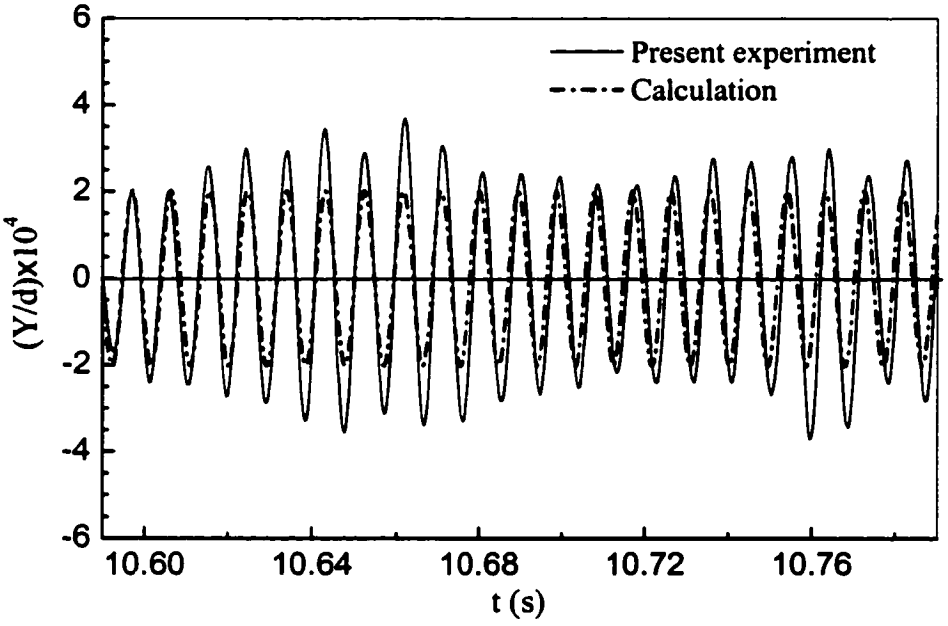

Figure 6-5 Comparison between the calculated and measured Y time series for $U_r = 5$.

The comparison shown in Figure 6-4 cannot fully reveal the difference between the linear analysis and the nonlinear behavior of the free vibration of a single cylinder in a cross flow. This difference, however, can be shown clearly by comparing the predicted Y

time series with that measured at the mid-span of the cylinder. A typical comparison for $U_r = 5$ is shown in Figure 6-5. The theoretical prediction gives a pure harmonic behavior for Y with a dominant frequency given by the first-mode natural frequency, which in this case is equal to the vortex shedding frequency. On the other hand, the measured Y time series reveals a host of harmonics besides the first-mode natural frequency. This indicates that the free vibration of a single cylinder in a cross flow is a true nonlinear problem. The nonlinearity arises from the interaction between the cylinder motion and the flow, through the moving boundary of the cylinder (Jadic *et al.* 1998).

6.5.2 Behavior of the predicted damping

The behavior of the natural frequencies and the modal damping ratios for a linear fluid-cylinder dynamic system is described by (6-24) to (6-28). The two parameters are related and they depend on the dimensionless parameters M^*, C_D and U_r. If M^* and C_D are fixed, the two parameters only depend on U_r. This is the case for the present experiment. It can be seen that, to the lowest order, the prediction is qualitatively consistent with experimental observation. As the structural mode n increases, the natural frequencies of the cylinder increase and the corresponding structural damping ratios (6-26a) decrease. On the other hand, the fluid damping ratios (6-26b) or (6-28) are virtually independent of the structural mode because the effects of n and U_r cancel out each other. For instance, at the first-mode resonance ($n = 1$), $(2n+1)^2 = 9$ and $U_r \approx 5$. At the third-mode resonance ($n = 3$), $(2n+1)^2 = 49$ and $U_r \approx 26.9$. The ratio $U_r/(2n+1)^2$ remains almost unchanged. The resultant modal damping ratios therefore decrease for a higher

vibration mode. Note that, as U_r increases, the drag-induced fluid damping ratios (6-26a and 28) are predicted to increase. However, the contribution from fluid damping to the modal damping ratios is small in the present context. This could explain why the measured modal damping ratios (Zhang *et al.*, 2000) were quite comparable in the inline and cross-flow directions; they increased slowly when $U_r > 15$.

6.5.3 Effect of axial force on the structural response

When the cylinder is subject to an axial loading, the natural frequency of cylinder would be changed. This can be illustrated by solving the frequency equation (6-18). After tedious algebra, one obtains $R_f = \omega_{kN}/\omega_k = [(4EI\beta_{k2}^2 + 2N) - c_k^2/(M\beta_{k2}^2)]^{1/2}$, where ω_{kN} and ω_k are the circular frequency with and without axial loading and damping, respectively. The subscript k (= x or y) denotes drag or lift. The term β_{k2} can be solved from Eqs.(6-18) and (6-19). In general, its value is a group of positive real roots of Eqs.(6-18) & (6-19). Evidently, for $N>0$ (or <0), the natural frequency would be increased (or decreased).

Figure 6-6 presents the effect of axial loading on first mode frequency. Here, the displacement is calculated assuming the cylinder is immersed in water. Other parameters are the same as giving earlier in this section. The tensile axial force causes a 15% increase in the first mode frequency, while the compressive axial force decreases the first mode frequency by 13%.

To further illustrate, a ratio $Y^* = Y_{rms}|_{N>0} / Y_{rms}|_{N=0}$ is calculated, where $Y_{rms}|_{N>0}$ and $Y_{rms}|_{N=0}$ denote Y_{rms} calculated with and without the effect of axial force N present,

respectively. This ratio is plotted in Figure 6-7 for a range of M^* and several U_r. It can be seen that Y^* deviates greatly from 1 for small values of M^*. For the example (cylinder in a water flowing medium) shown here, the maximum mean deflection at mid-span divided by the cylinder span is about 0.63% as the first-mode resonance occurs. Consequently, the maximum rotation of the cylinder in the x-z plane is equal to 0.012 radian. Therefore, all the governing equations and their results are still valid in this case.

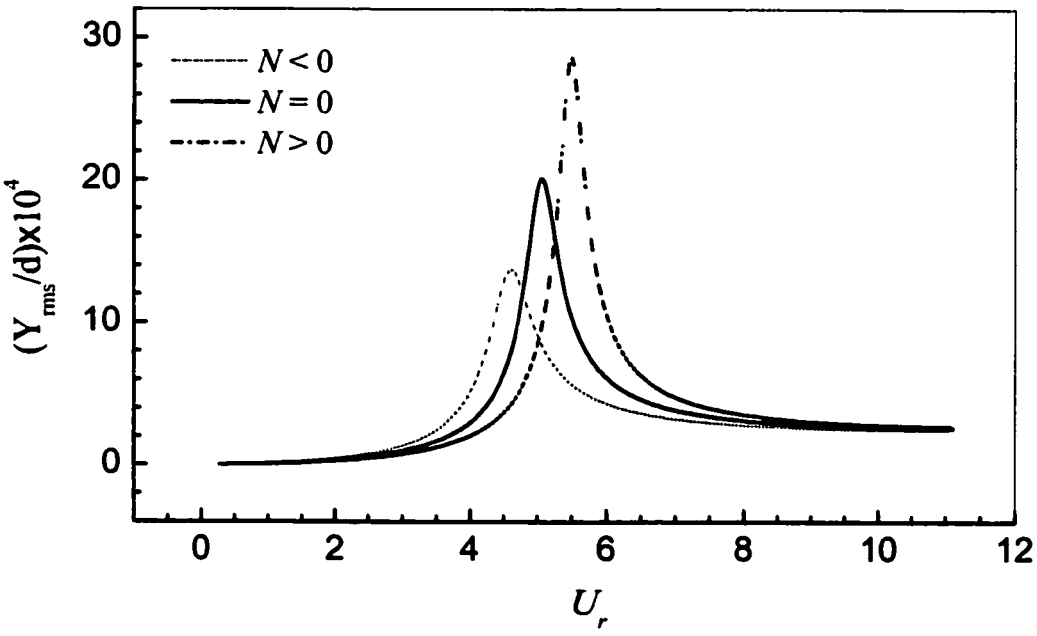

Figure 6-6 Effect of axial force N, associated with the steady drag, on the first-mode resonance assuming that the cylinder is subjected to a water cross flow.

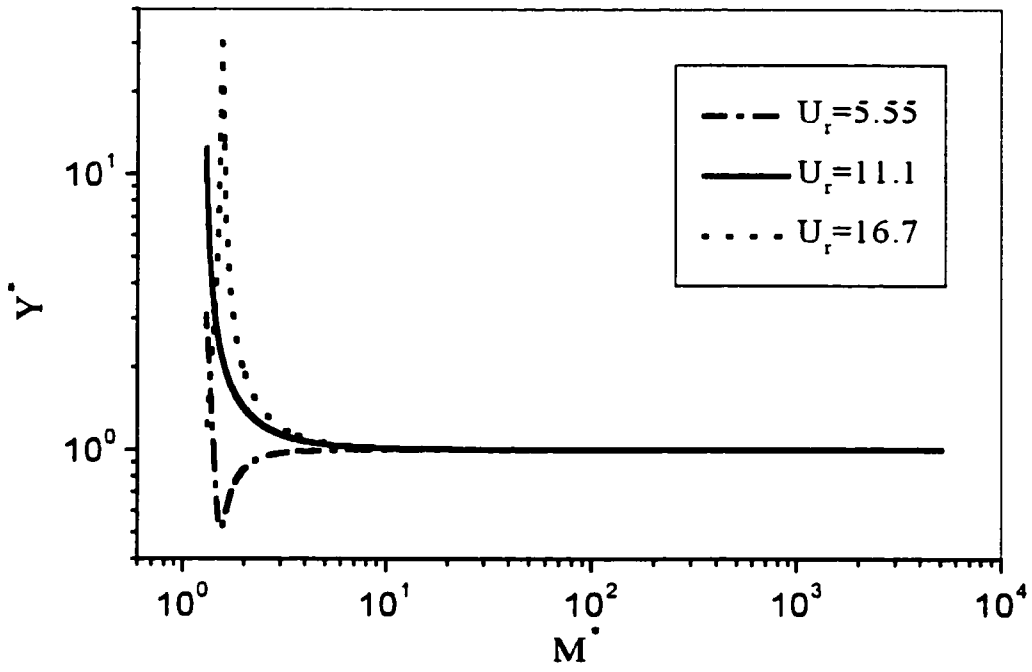

Figure 6-7 Variation of $Y^* = \frac{Y_{rms}|_{N\neq 0}}{Y_{rms}|_{N=0}}$ with M^* for several U_r, where $Y_{rms}|_{N\neq 0}$ and $Y_{rms}|_{N=0}$ denote Y_{rms} calculated with and without the effect of axial force N present, respectively.

6.5.4 Spanwise distribution of Y_{rms}/d

The spanwise distributions of Y_{rms}/d for two different U_r have been reported by So *et al.* (2000b). One case is when resonance occurs with the first-mode natural frequency, another case is off the first-mode resonance. In the resonance case, the spanwise distribution of Y_{rms}/d clearly displays a shape that is consistent with the first mode of vibration, while the off-resonance case displays a shape that is indicative of a

combination of first and third mode of vibrations. These two cases were calculated using (6-14) and (6-15).

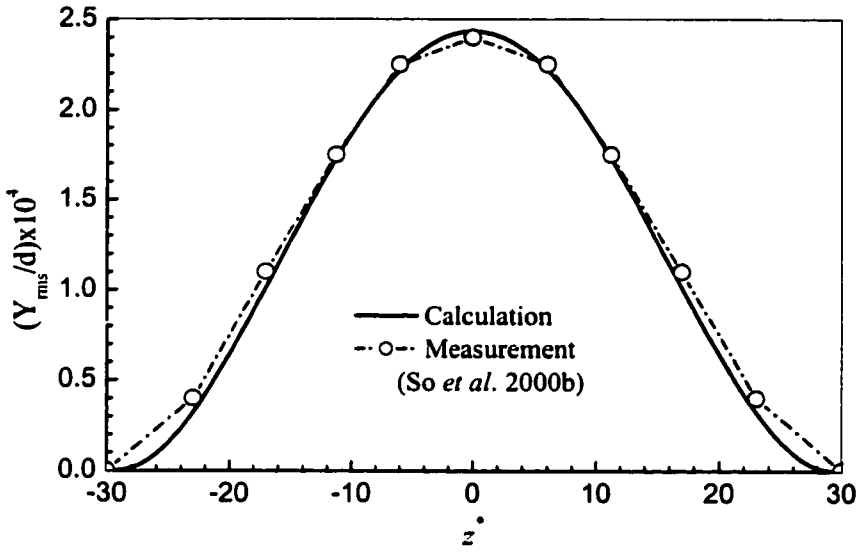

Figure 6-8 Spanwise distribution of Y_{rms}/d for the resonance case ($U_r = 4.2$).

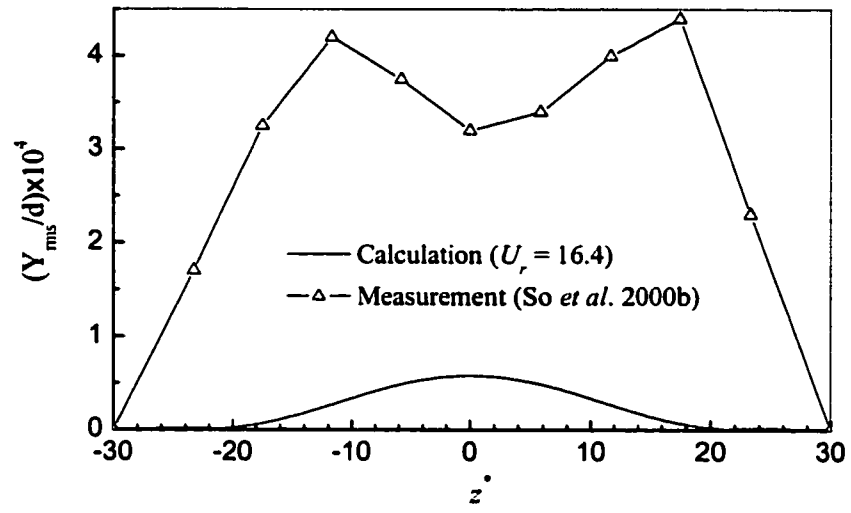

Figure 6-9 Spanwise distribution of Y_{rms}/d for the off-resonance case ($U_r = 16.4$).

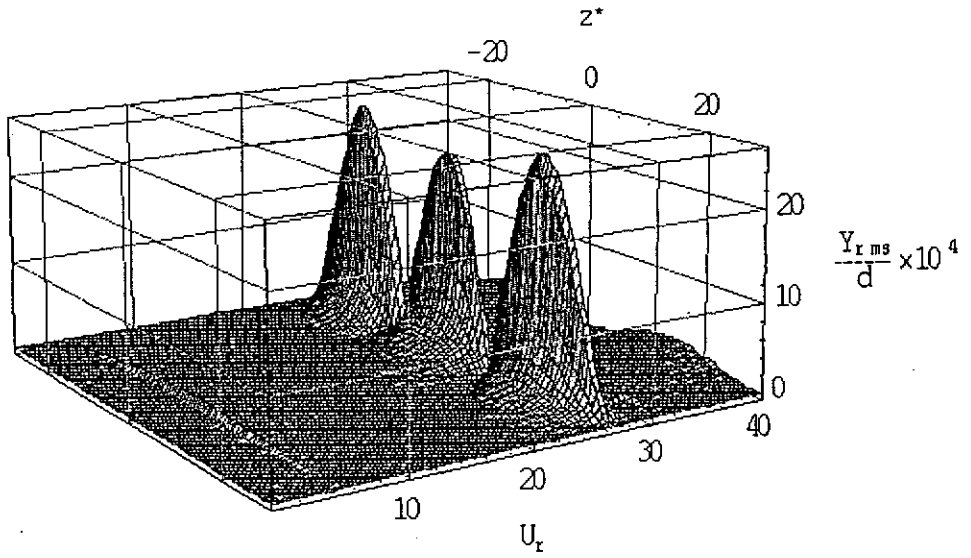

(a)

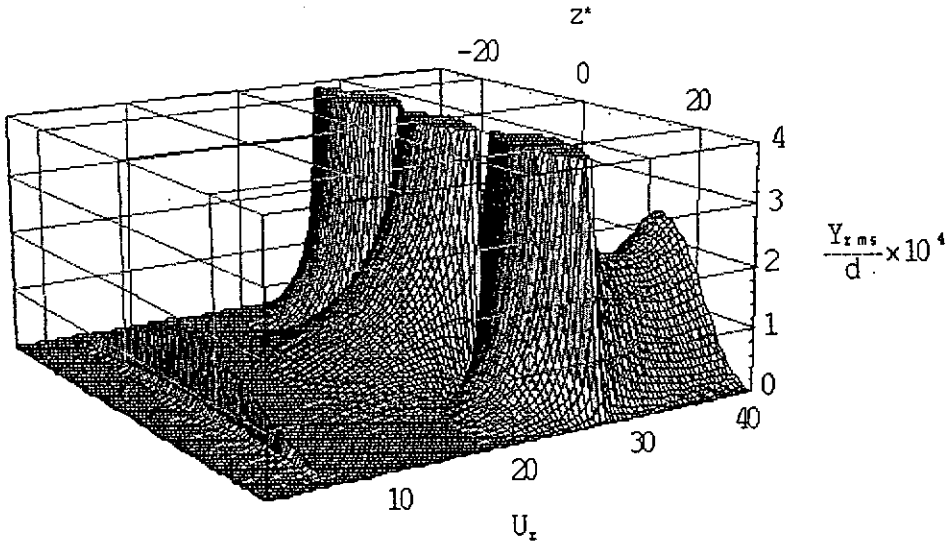

(b)

Figure 6-10 A plot of the spanwise distribution of Y_{rms}/d versus U_r.

The choice of Eq. (6-15) for the damping is because Figure 6-4 shows that the

theoretical analysis gives reasonable prediction of resonance with the first-mode natural frequency. Comparisons of the resonance and off-resonance cases are shown in Figures 6-8 and 6-9, respectively. The agreement between predictions and measurements is fairly good for a linear analysis. Finally, a spanwise distribution plot of Y_{rms}/d versus U_r is shown in Figure 6-10. This plot is made from the calculations shown in Figure 6-4. The evolution of the spanwise distribution of Y_{rms}/d for the range of U_r investigated is displayed; i.e., the change from first mode vibration to mixed mode vibration as U_r varies is clearly indicated.

6.5.5 Dynamic strain response

The predicted dynamic strain in the lift direction is compared with the measurements of Zhou *et al.* (2001). The comparison with ε_{Yrms} is shown in Figure 6-11.

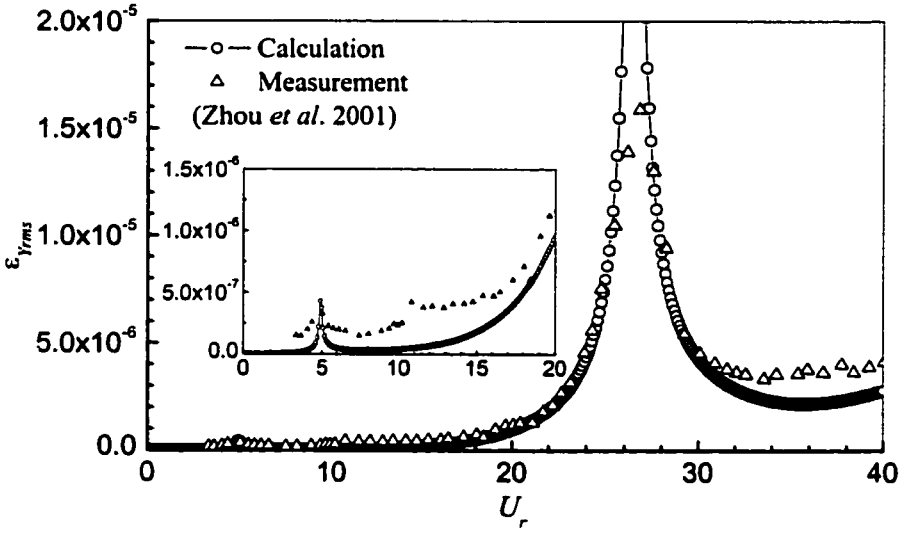

Figure 6-11. Comparison between the calculated and measured ε_{Yrms}.

Again, the analytical result is in agreement with experimental data up to $U_r = 26.9$ for the measurements in the y-direction, i.e., ε_{Yrms}. That also proves that the relationship between displacement and strain is not linear beyond the third mode resonance. There exists a slight peak around $U_r = 11$ in this set of experimental data. One possible reason could be that the measured point is not precisely at the stagnation line. Consequently, the measured strain might include the third-mode resonance vibration in the drag direction

6.5.6 Effect of damping on structural response

In this paper, the actions of fluid on structure are analyzed into three components. The one is fluid exciting force related to vortex shedding. The second one is modal damping. The last one is the random component neglected in above calculations. Here we discuss the effect of modal damping on structural vibration. In above calculation, the modal damping data from Zhou *et al.* (2001) were documented. As shown in Figure 6-4 and Figure 6-11, this modal damping should have taken a good effect on response up to the third mode resonance. However, the calculation deviates from experiment at the third mode resonance, because the corresponding modal damping is underestimated. On the other hand, the random component neglected in calculation may take some effect at this time.

6.6 Conclusions

The dynamical equations of motion are derived for a cylinder freely vibrating in a uniform cross flow. The axial loading, which is the consequence of a mean deformation

of the cylinder, is considered in the formulation for the first time. The vortex-excited forces acting on the cylinder are modeled by the sum of a steady, a periodic and a random component. The problem thus formulated can be solved analytically if the assumption of small deformation is invoked and the parameters introduced in the vortex-excited force model are determined from experimental measurements. This study leads to the following conclusions.

1. The analysis is valid for an elastic cylinder with any cross section. For the free vibration problem analyzed here, the analytical solution correctly predicts the occurrence of the first- and the third-mode natural frequency. It also predicts fairly correctly the displacement and strain response of the freely vibrating cylinder over a wide range of U_r ($0 < U_r \leq 26.9$). Beyond $U_r = 26.9$, there is a substantial difference between calculation and measurements. This discrepancy could be traced to the linear assumption used to simplify the analysis. Furthermore, the analytical solution also predicts correctly the shape of the Y_{rms} distribution for the case where resonance occurs with the first-mode natural frequency.
2. The influence of the modal damping of the fluid-cylinder system on the structural vibration has been examined. While this influence may be negligible on the natural frequency of the system, it is very significant on the vibration amplitude. At the third-mode resonance the vibration amplitude is seen decreasing by about 50% as a result of using the measured modal damping ratio, rather than that derived analytically. In spite of this improvement, the agreement with the

measured amplitude is still not good. The reason could be attributed to nonlinear effects at or near resonance because the deformation is large and the assumption of small deformation fails.

3. The axial force may have a negligible effect on the structural response in airflow but should not be overlooked in a water flow. This force could result in a significant increase in both the cylinder vibration amplitude and the natural frequencies of the fluid-cylinder system.

CHAPTER 7

SUMMARY AND CONCLUSIONS

In this work, the fluid-structure interactions of a streamwise oscillating circular cylinder in a cross flow in the presence of a neighbouring cylinder have been studied. The main conclusions are summarized below.

Firstly, the wake of a streamwise oscillating cylinder has been experimentally investigated using the LIF, PIV and hot-wire techniques at relatively large oscillation amplitudes A/d = 0.5 and 0.67 over a range of frequencies f_e/f_s = 0 ~ 3.1. The flow structure depends on both f_e/f_s and A/d. Five distinct modes of flow structures have been identified, i.e., S-I, A-I, A-III, A-IV, S-II. The flow structure of the S-II mode is experimentally observed for the first time. The analysis of forces of the oscillating cylinder on the fluid indicates that a nonlinear force and the linear damping force associated with the streamwise cylinder oscillation are probably responsible for the occurrence of the symmetrical vortex shedding. The mode of the flow structure depends on the wake feedback mechanism as well as the non-linear force and the linear damping force. Since the forces are small if f_e/f_s is low for a given A/d, the wake feedback effect is dominant, resulting in unstable S-I mode. As f_e/f_s increases, the forces may overwhelm

the wake feedback mechanism, thus inducing stable symmetrical boundary layer separation and forming a symmetric vortex street, an S-I mode or an S-II mode. Analysis has also been conducted to predict the occurrence of the S-II mode flow structure. The critical frequency ratio, $(f_e/f_s)_c$, for the S-II mode to occur is inversely proportional to A/d and dependent on Re. The Re effect is negligible for $Re > 250$. The prediction is in excellent agreement with experimental data.

Secondly, The effect of a streamwise oscillating cylinder at $f_e/f_s = 0 \sim 2$ and $A/d = 0.5 \sim 0.67$ on the downstream cylinder wake has been experimentally investigated for $L/d = 2.5 \sim 4.5$ and $Re = 150 \sim 1150$ using the LIF, PIV and hot-wire techniques. The mean pressure, drag and lift on the downstream cylinder were also measured. The flow structure behind the cylinders depends on the combination of A/d and f_e/f_s. Three distinct flow regimes have been identified for $0 < f_e/f_s < 2$ and $A/d = 0.5 \sim 0.67$, i.e., the symmetric-antisymmetric complex street (SA-mode), the antisymmetric-antisymmetric complex street (AA-mode) and single antisymmetrical street (A-mode). The SA-mode occurs for $f_e/f_s > (f_e/f_s)_c$ (about 1.45 for $A/d = 0.67$, 1.6 for $A/d = 0.5$). Analysis has been developed to predict the occurrence of the SA-mode flow structure, which is in excellent agreement with the experimental data. The AA-mode occurs for 0.8 (A/d = 0.67)~ 1.0 (A/d = 0.5) $\lesssim f_e/f_s \lesssim (f_e/f_s)_c$, when alternate vortex shedding occurs for both cylinders. The A-mode emerges behind the downstream cylinder at $0.45 \sim 0.5 \lesssim f_e/f_s \lesssim 0.8$ (A/d =0.45)~ 1.6 (A/d = 0.67). In general, f_e/f_s, at which a particular mode of the flow structure occurs, decreases as A/d increases. The drastic change in the flow structure with f_e/f_s at a fixed A/d results in different pressure distribution on the downstream cylinder and further

results in a variation on the mean drag. The mean drag is largest for the AA-mode and smallest for the SA-mode. In all cases, the mean drag is significantly larger than the case of two stationary cylinders of the same L/d. This is linked to the generation of vortices between the cylinders by the oscillation of the upstream cylinder. In contrast, there are no vortices generated between the two stationary cylinders. In the wake of two inline stationary cylinders, the flow structure depends on L/d. The critical L/d may vary with Re because of the Re dependence of the vortex formation length. When the upstream cylinder oscillates, however, the oscillation appears controlling fluid dynamics around the two cylinders and Re is probably of secondary importance, showing a negligible effect on the occurrence of the flow structure of different modes. The occurrence of the flow structure mode is further independent of L/d ($= 2.5 \sim 4.5$).

Thirdly, interference between a stationary cylinder wake and that of a downstream streamwise oscillating cylinder ($L/d = 2.5 \sim 4.5$; $A/d = 0.5$ and 0.67; $f_e/f_s = 0$ to 2) has also been studied. Two flow regimes have been identified, i.e., the 'single-cylinder shedding regime' at $L/d \leq 3.5$ and the 'two-cylinder shedding regime' at $L/d > 3.5$. At a small L/d, the streamwise oscillation of the downstream cylinder dominates. The shear layers separated from the upstream cylinder do not have sufficient space to develop into vortices, while those from the downstream cylinder are shed symmetrically to form a symmetrical vortex street. As L/d increases, the oscillation effect on the shear layer separation from upstream cylinder impairs so that the alternate vortex shedding resumes. The anti-symmetrically arranged vortices generated by the upstream cylinder may

subsequently impose an alternate excitation on the downstream oscillating cylinder, which suppresses the symmetrical vortex shedding, inducing alternate shedding.

Fourthly, experimental study of the near wake structure of two side-by-side cylinders has been conducted at Re = 150 –14300 and T/d = 1.2 - 1.6 using LIF, PIV and hotwire techniques. As $T/d < 1.25$, the near-wall effect is dominant; Re based on the gap flow velocity is so small that periodic vortex shedding cannot be induced from the inner side of the cylinders. As a result, vortices shed from the outer side only of the two cylinders, generating a single vortex street. For $1.25 \lesssim T/d \lesssim 1.6$, two flow structures have been observed. At a relatively low Re, a small closed wake occurs behind one cylinder; the flow is characterized by one single vortex street, dominated by a frequency measured at $f_0^* \approx 0.09$. The occurrence of the small wake is probably due to the near-wall effect at small T/d. The effect gives rise to a small gap flow velocity. The Reynolds number based on this velocity is then substantially smaller than Re, which is based on U_∞. As U_∞ or Re increases, the Reynolds number based on the gap flow velocity may exceed a critical value. The small closed wake then ceases to exist. Meanwhile, periodic vortex shedding starts, forming one narrow vortex street, coexisting with the wide street. The narrow and wide street are associated with a dominant frequency of about 0.3 and 0.09, respectively. Apparently, the smaller the gap between the cylinders, the stronger is the near-wall effect. Consequently, transition from the one-street to the two-street flow structure occurs at a larger Re. The present observation and interpretation sheds light upon the seemingly inconsistent reports of the dominant frequencies for $1.25 \leq T/d \leq 1.5$ in the literature. For $1.6 < T/d < 2.0$, the near-wall effect could be negligible, and

therefore the one-street flow structure is absent. The flow consists of one narrow and one wide street throughout the *Re* range investigated. At $T/d > 2.0$, two predominantly anti-phase streets occur.

Finally, vortex induced vibration of a single cylinder in a cross flow was analyzed theoretically by considering the cylinder as an elastic beam. Two-dimensional coupled and nonlinear dynamics equations were established based on the Hamilton's principle. The fluid forces were simplified and calculated using the related parameters such as the Strouhal number, root-mean-square lift and drag coefficients, and fluid damping ratio, which could be directly determined from previous experimental results. The axial loading, which is the consequence of a mean deformation of the cylinder, is considered in the formulation for the first time. Displacement and strain responses, and natural frequency of the cylinder have been solved analytically using Mathematica© software. The effect of the effective damping of the fluid-cylinder system on the structural vibration may be negligible on the natural frequency of the system but is very significant on the vibration amplitude. The axial force may have a negligible effect on the structural response in airflow but should not be overlooked in a water flow. This force could result in a significant increase in both the cylinder vibration amplitude and the natural frequencies of the fluid-cylinder system. The analysis should be valid for the elastic cylinder of any cross section.

References

ARIE, M., KIYA, M., MORIYA, M. & MORI, H. 1983 Pressure fluctuations on the surface of two circular cylinders in tandem arrangement. *Journal of Fluids Engineering*, **105**, 161-166.

BEARMAN, P. W., DOWNIE, M. J. & GRAHAM J. M. R. 1985 Forces on cylinders in viscous oscillatory flow at low Keulegan-Carpenter numbers. *Journal of Fluid Mechanics*, **154**, 337-356.

BEARMAN, P. W. 1984 Vortex shedding from oscillating bluff bodies. *Annual Review of Fluid Mechanics*, **16**, 195-222.

BEARMAN, P. W. & WADCOCK, A. J. 1973 Interference between a pair of circular cylinders normal to a stream. *Journal of Fluid Mechanics*, **61**, 499-511.

BERGER, E. 1988 On a mechanism of vortex excited oscillations of a cylinder. *Journal of Wind Engineering and Industrial Aerodynamics*, **28**, 301-310.

BISHOP, R. E. D. & HASSAN, A. Y. 1964 The lift and drag forces on a circular cylinder in a flowing fluid. *Proceeding of the Royal Society* (London) A**277**, 51-75.

BLEVINS, R. D. 1994 *Flow-induced Vibration* (2nd edition). Krieger Publishing Company, Florida, USA, p. 25.

BRIKA, D. & LANEVILLE, A. 1999 The flow interaction between a stationary cylinder and a downstream flexible cylinder. *Journal of Fluids and Structures*, **13**, 579-606.

CANTWELL, B. & COLES, D. 1983 An experimental study of entrainment and transport in the turbulent near wake of a circular cylinder. *Journal of Fluid Mechanics*, **136**, 321-374.

CARBERRY, J. & SHERIDAN, J. 2001 Forces and wake modes of an oscillating cylinder. *Journal of Fluids and Structures*, **15**, 523-532.

CETINER, O. & ROCKWELL, D. 2001 Streamwise oscillations of a cylinder in a steady current (Part I, Locked-on states of vortex formation and loading; Part II, Free-surface effects on vortex formation and loading). *Journal of Fluid Mechanics*, **427**, 1-59.

CHANG, W. K., PILIPCHUK, V. & IBRAHIM, R. A. 1997 Fluid flow-induced nonlinear vibration of suspended cables. *Nonlinear Dynamics*, **14**, 377-406.

CHEN, S. S. 1978 Crossflow-induced vibrations of heat exchanger tube banks. *Nuclear Engineering and Design*, **47**, 67-86.

CHEN, S. S. 1987 *Flow-induced Vibration of Circular Cylinder Structures*. Hemisphere Publishing Corporation, pp. 255 and 271-272.

EDWARD, F. B. & ROBERT, D. S. 1968 *Engineering Mechanics of Deformable Bodies*. International Textbook Company, Scranton, Pennsylvania, USA, pp. 214-216.

EVANGELINOS, C. & KARNIADAKIS, G. E. 1999 Dynamics and flow structures in the turbulent wake of rigid and flexible cylinders subject to vortex-induced vibrations. *Journal of Fluid Mechanics*, **400**, 91-124.

EVANGELINOS, C., LUCOR, D. & KARNIADAKIS, G. E. 2000 DNS-derived force distribution on flexible cylinders subject to vortex-induced vibration. *Journal of Fluids and Structures*, **14**, 429-440.

FENG, C. C. 1968 *The measurement of vortex-induced effects in flow past stationary and oscillating circular and D-section cylinders*. MASc thesis. University of British Columbia, Vancouver, B.C., Canada.

GERRARD, J. H. 1966 Formation region of vortices behind bluff bodies, *Journal of Fluid Mechanics*, **25**, 401-413.

GERRARD, J. H. 1978 Wakes of cylindrical bluff bodies at low Reynolds number. *Philosophical Transactions of the Royal Society* (London), Ser. A, **288**, 351-382.

GOVARDHAN, R. & WILLIAMSON, C. H. K. 2000 Modes of vortex formation and frequency response of a freely vibrating cylinder, *Journal of Fluid Mechanics*, **420**, 85-130.

GRIFFIN, O. M. 1980 OTEC cold water pipe design for problems caused by vortex-excited oscillation. *NRL Memorandum Report* **4157**, *Naval Research Laboratory, Washington, D. C.*

GRIFFIN, O. M. & HALL, M. S. 1991 Review – vortex shedding locked-on and flow control in bluff-body wakes. *Trans. ASME: Journal of Fluids Engineering*, **113**, 526-537.

GRIFFIN, O. M. & RAMBERG, S. E. 1976 Vortex shedding from a cylinder vibrating in line with an incident uniform. *Journal of Fluid Mechanics*, **75**, 257-271.

HARRISON, H. R. & NETTLETON, T. 1997 *Advanced Engineering Dynamics*. John Wiley & Sons, New York, USA, pp. 46-55.

HOVER, F. S., TECHET, A. H. & TRIANTAFYLLOU, M. S. 1998 Forces on oscillating uniform and tapered cylinders in crossflow. *Journal of Fluid Mechanics*, **363**, 97-114.

IGARASHI, T. 1981 Characteristics of the flow around two circular cylinders arrangement in tandem (1st report). *Bulletin of the JSME*, **24**, 323-331.

IGARASHI, T. 1984 Characteristics of the flow around two circular cylinders arrangement in tandem (2nd report). *Bulletin of the JSME*, **27**, 2380-2387.

ISHIGAI, S., NISHIKAWA, E., NISHMURA, K. & CHO, K. 1972 Experimental study on structure of gas flow in tube banks with tube axes normal to flow (Part 1, Kármán vortex flow around two tubes at various spacings. *Bulletin of the JSME*, **15**, 949-956.

IWAN, W. D. & BLEVINS, R. D. 1974 A model for vortex induced oscillation of structures. *Journal of Applied Mechanics*, **41**, 581-586.

JADIC, I., SO, R. M. C. & MIGNOLET, M. P. 1998 Analysis of fluid-structure interactions using a time marching technique. *Journal of Fluids and Structures*, **12**, 631-654.

JAMES, M. L., SMITH, G. M., WOLFORD, J. C. & WHALEY, P. W. 1994 *Vibration of Mechanical and Structural Systems with Microcomputer Applications*. Harper Collins College Publishers, pp. 57-61.

JIN, W., ZHOU, Y., CHAN, P. K. C. & XU, H. G.: 2000. "An optical fibre Bragg grating sensor for flow-induced structural vibration measurement," *Sensors and Actuators*, **79**, 36-45.

KAMEMOTO, K. 1976 Formation and interaction of two parallel vortex streets. *Bulletin of the JSME*, **19**, 283-190.

KARNIADAKIS, G E & TRIANTAFYLLOU, G 1989 Frequency selection and asymptotic states in laminar wakes. *Journal of Fluid Mechanics*, **199**, 441-469.

KHALAK, A. & WILLIAMSON, C. H. K. 1996 Dynamics of a hydroelastic cylinder with very low mass and damping. *Journal of Fluids and Structures*, **10**, 455-472.

KHALAK, A. & WILLIAMSON, C. H. K. 1997 Fluid forces and dynamics of a hydroelastic structure with very low mass and damping. *Journal of Fluids and Structures*, **11**, 973-982.

KHALAK, A. & WILLIAMSON, C. H. K. 1999 Motions, forces and mode transitions in vortex induced vibrations at low mass-damping. *Journal of Fluids and Structures*, **13**, 813-851.

KIM, H. J. & DURBIN, P. A. 1988 Investigation of the flow between a pair of circular cylinders in the flopping regime, *Journal of Fluid Mechanics*, **196**, 431-448.

KING, R. 1976 Wake interaction experiments with two flexible circular cylinder in flowing water. *Journal of Sound and Vibration*, **45**(2), 259-283.

KING, R., PROSSER, M. J. & JOHNS, D. J. 1973 On vortex excitation of model piles in water. *Journal of Sound and Vibration*, **29**(2), 169-188.

KING, R. 1977 A review of vortex shedding research and its application. *Ocean Engineering.* **4**, 141-171.

LANDL, R. 1975 A mathematical model for vortex-excited vibrations of bluff bodies. *Journal of Sound and Vibration*, **42**, 219-234.

LANDWEBER, L. 1942 Flow about a pair of adjacent, parallel cylinders normal to a stream. D. W. Taylor Model Basin, Department of the Navy, Report 485, Washington, D.C.

LANEVILLE, A. & BRIKA, D. 1999 The fluid and mechanical coupling between two circular cylinders in tandem arrangement. *Journal of Fluids and Structures*, **13**, 967-986.

LI, J., SUN, J. & ROUX, B. 1992 Numerical study of an oscillating cylinder in uniform flow and in the wake of an upstream cylinder, *Journal of Fluid Mechanics*, **237**, 457-478.

LIGHTHILL, M. J. 1979 Waves and hydrodynamic loading. *BOSS Confence, Imperial College, London*, pp. 1-38.

LJUNGKRONA, L, NORBERG, C. & SUNDÉN, B 1991 Free-stream turbulence and tube spacing effects on surface pressure fluctuations for two tubes in an in-line arrangement, *Journal of Fluids and Structures*, **5**, 701-727.

MENDES, P. A. & BRANCO, F. A. 1999 Analysis of fluid-structure interaction by an arbitrary lagrangian-eulerian finite element formulation. *International Journal for Numerical Methods in Fluids*, **30**, 897-919.

MITTAL, S. & KUMAR, V. 1999 Finite element study of vortex-induced cross-flow and in-line oscillations of a circular cylinder at low Reynolds numbers. *International Journal for Numerical Methods in Fluids*, **31**, 1087-1120.

NAUDASCHER, E. 1987 Flow-induced streamwise vibrations of structures. *Journal of Fluids and Structures*, **1**, 265-298.

NAYFEH, A. H. & MOOK, D. T. 1995 *Nonlinear Oscillations*. John Wiley & Sons, New York, USA, pp. 175-182 & 448.

NEWMAN, D. & KARNIADAKIS, G. E. 1996 Simulations of flow over a flexible cable: A comparison of forced and flow-induced vibration. *Journal of Fluids and Structures*, **10**, 439-453.

ONGOREN, A. & ROCKWELL, D. 1988a Flow structure from an oscillating cylinder. Part I. Mechanisms of phase shift and recovery in the near wake. *Journal of Fluid Mechanics*, **191**, 197-223.

ONGOREN, A. & ROCKWELL, D. 1988b Flow structure from an oscillating cylinder. Part II. Mode competition in the near wake. *Journal of Fluid Mechanics*, **191**, 225-245.

Peschard, I. & Le Gal, P. 1996 Coupled wakes of cylinders. *Physical Review Letters* **77**, 3122-3125.

QUADFLIEG, H. 1977 Vortex induced load on the cylinder pair at high *Re*, *Forsch. Ing. Wes*, **43**, 9-18.

RAO, J. S. 1992 *Advanced Theory of Vibration*. John Wiley & Sons, New York, USA, p. 294.

ROY, R. C. 1996 *Mechanics of Materials*. John Wiley & Sons, New York, USA, p. A-34.

SARPKAYA, T. 1979 Vortex-induced oscillations: a selective review. *Journal of Applied Mechanics*, **46**, 241-258.

SARPKAYA, T. 1980 Hydrodynamic interference of two cylinders in harmonic flow. *OTC Paper* 3775, *Houston, Texas*.

SARPKAYA, T. 1995 Hydrodynamic damping, flow-induced oscillations, and biharmonic response. *Journal of Offshore Mechanics and Arctic Engineering, Transaction of the ASME*, **117**, 232-238.

SCHLICHTING, H. & GERSTEN, K. 2000 *Boundary Layer Theory*. 8th revised and enlarge edition. Springer-Verlag Berlin Heidelberg, p. 22.

SKOP, R. A. & GRIFFIN, O. M. 1973 A model for the vortex-excited resonant response of bluff cylinders. *Journal of Sound and Vibration*, **27**, 225-233.

SO, R. M. C., JADIC, I. & MIGNOLET, M. P. 1999 Fluid-structure resonance produced by oncoming alternating vortices. *Journal of Fluids and Structures*, **13**, 519-548.

SO, R. M. C., LIU, Y., CHAN, S. T. & LAM, K. 2000a Numerical studies of a freely vibrating cylinder in a cross flow. *Journal of Fluids and Structures*, **15**, 845-866.

SO, R. M. C., ZHOU, Y. & LIU, M. H. 2000b Free vibrations of an elastic cylinder in a cross flow and their effects on the near wake. *Experiments in Fluids*, **29**, 130-144.

SPIVACK, H. M. 1946 Vortex frequency and flow pattern in the wake of two parallel cylinders at varied spacings normal to an air stream. *Journal of Aeronautical Sciences*, **13**, 289-297.

STAUBLI, T. & ROCKWELL, D. 1989 Pressure fluctuations on an oscillating trailing edge. *Journal of Fluid Mechanics*, **203**, 307-346.

STRONGE, W. J. & YU, T. X. 1993 *Dynamic Models for Structural Plasticity*. Springer-Verlag. London, UK, p. 51.

SUMNER, D., PRICE, S. J. & PAÏDOUSSIS, M. P. 2000 Flow-pattern identification for two staggered circular cylinders in cross-flow. *Journal of Fluid Mechanics*, **411**, 263-303.

SUMNER, D., WONG, S. S. T., PRICE, S. J. & PAÏDOUSSIS, M. P. 1999 Fluid behaviour of side-by-side circular cylinders in steady cross-flow. *Journal of Fluids Structures*, **13**, 309-338.

TANIDA, Y, OKAJIMA, A & WATANABE Y 1973 Stability of a circular cylinder oscillating in a uniform flow or in a wake. *Journal of Fluid Mechanics*, **61**, 769-784.

WANG, X. Q., SO, R. M. C. & LIU, Y. 2000 Flow-induced vibration of an Euler-Bernoulli beam. *Journal of Sound and Vibration*, **243** (2), 241-268.

WEAVER Jr, W., TIMOSHENKO, S. P. & DONOVAN, H. Y. 1989 *Vibration Problems in Engineering* (5^{th} edition). John Wiley and Sons, New York, USA, p. 426-432 & 454-456.

WILLERT, C. E. & GHARIB, M. 1991 Digital Particle Image Velocimetry. *Experiments in Fluids*, **10**, 181-193.

WILLIAMSON, C. H. K. 1985a Evolution of a single wake behind a pair of bluff bodies. *Journal of Fluid Mechanics*, **159**, 1-18.

WILLIAMSON, C. H. K. 1985b Sinusoidal flow relative to circular cylinders. *Journal of Fluid Mechanics*, **155**, 141-174.

WILLIAMSON, C. H. K. & ROSHKO, A. 1988 Vortex formation in the wake of an oscillating cylinder. *Journal of Fluids and Structures*, **2**, 355-381.

ZDRAVKOVICH, M. M. 1984 Classification of flow-induced oscillations of two parallel circular cylinders in various arrangements. *Symposium on Flow-induced Vibrations*, Vol. 2, p. 1-18.

ZDRAVKOVICH, M. M. 1985 Flow induced oscillations of two interfering circular cylinders. *Journal of Sound and Vibration*, **101**, 511-521.

ZDRAVKOVICH, M. M. 1986 Discussion: Effect of a vibrating upstream cylinder on a stationary downstream cylinder. *ASME Journal of Fluids Engineering*, **108**, 383-385.

ZDRAVKOVICH, M. M. 1987 The effects of interference between circular cylinders in cross flow. *Journal of Fluids and Structures*, **1**, 239-261.

ZDRAVKOVICH, M. M. 1997 *Flow Around Circular Cylinders Vol. 1: Fundamentals.* Oxford University Press, Oxford, England, p. 17.

ZDRAVKOVICH, M. M. & NAMORK, J. E. 1977 Formation and reversal of vortices around circular cylinders subject to water waves. *Journal of the Waterway Port Coastal and Ocean Division – ASCE*, **103**(3), 378-383.

ZHANG, H. J., ZHOU, Y., So, R. M. C., MIGNOLET, M. P. & WANG, Z. J. 2000 Measurement of Fluid and Structural Damping using an ARMA Technique,

Proceedings of International Conference on Advances in Structural Dynamics, Vol. **2**, p. 1109-1116. Hong Kong.

ZHANG, H. J. & ZHOU, Y. 2001 Effect of Unequal Cylinder Spacing on Vortex Streets behind Three Side-by-Side Cylinders. *Physics of Fluids*, **13**, 3675-3686.

ZHOU, Y. & ANTONIA, R. A.1993 A study of turbulent vortices in the wake of a cylinder. *Journal of Fluid Mechanics*, **253**, 643-661.

ZHOU Y., SO, R. M. C., JIN, W., XU, H. G. & CHAN, P. K. C. 1999 Dynamic strain measurements of a circular cylinder in a cross flow using a fibre Bragg grating sensor. *Experiments in Fluids*, **27**, 359-367.

ZHOU, Y., WANG, Z. J., SO, R. M. C., XU, S. J. & JIN, W. 2001 Free vibrations of two side-by-side cylinders in a cross flow, *Journal of Fluid Mechanics*, **443**, 197-229.

ZHOU, Y., ZHANG, H. J. & YIU, M. W. 2002 The turbulent wake of two side-by-side circular cylinders, *Journal of Fluid Mechanics*, **458**, 303-332.

APPENDIX

PUBLISHED, ACCEPTED OR SUBMITTED PUBLICATIONS

Referred Journals:

S. J. XU, Y. ZHOU and R. M. C. SO 2002 An analytical solution to the structural dynamics of an elastic cylinder in a cross flow. *Dynamics of Continuous, Discrete and Impulsive Systems Journal* (**In press**).

S. J. XU, Y. ZHOU and R. M. C. SO 2002 A symmetric binary vortex street behind a longitudinal oscillating cylinder. *Journal of Fluid Mechanics* (**Submitted**).

S. J. Xu, Y. Zhou and R. M. C. So 2002 Reynolds number effects on the flow structure behind two side-by-side cylinders. *Physics of Fluids* (**Tentatively accepted**).

Y. ZHOU and S. J. XU 2002 Effect of a streamwise oscillating cylinder on a downstream cylinder wake. *Journal of Fluid Mechanics* (**Submitted**).

Y. ZHOU, Z. J. WANG, R. M. C. SO, S. J. XU & W. JIN 2001 Free vibrations of two side-by-side cylinders in a cross flow. *Journal of Fluid Mechanics*, **443**, 197-229.

S. J. XU, and Y. ZHOU 2002 Flow visualization behind a streamwise oscillating cylinder and a stationary cylinder in tandem arrangement. *Journal of Visualization* **(invited, submitted)**.

Referred Conference Proceedings:

S. J. XU, Y. ZHOU and R. M. C. SO 2002 Flow structure behind a streamwise oscillating cylinder, *Conference on Bluff Body Wakes and Vortex-induced Vibrations: BBVIV3, 17, December, 2002, Australia.* (accepted).

S. J. XU, Y. ZHOU and R. M. C. SO 2002 Reynolds number dependence of the flow structure behind two side-by-side cylinders. *Proceedings of 5th FSI, AE & FIV+N' 2002 ASME International Mechanical Engineering Congress & Exposition November 17-22, 2002, New Orleans, Louisiana, USA.* Paper No. IMECE2002-32176.

S. J. XU and Y. ZHOU 2002 Interference between a streamwise oscillating cylinder and a stationary cylinder in tandem arrangement. *The 10th International Symposium on Flow Visualization, August 26-29, 2002, Kyoto, Japan.* Paper No. F0256

S. J. XU and Y. ZHOU 2002 Effect of a streamwise oscillating cylinder on a downstream cylinder wake, Proceedings of 11th international Symposium on Applications of Laser Techniques to Fluid Mechanics (CD Rom), Lisbon, 8-11 July, 2002. Paper 34.4.

S. J. XU, Y. ZHOU and R. M. C. SO 2001 A linear analysis of the free vibration of a fix-supported elastic cylinder in a cross flow. *Proceedings of PVP'01, ASME Pressure Vessels and Piping Conferences*, Atlanta, Georgia, USA, July 22-26 (CD-ROM).